

Proceedings of the IEEE

Workshop on Agri-Food Robotics

Dealing with natural variability

October 2, 2015

Hamburg

Gert Kootstra
Yael Edan
Eldert van Henten
Marcel Bergerman

<http://dx.doi.org/10.18174/392250>

Table of content

Objectives.....	3
Organisers	4
Peer-reviewed papers	5
Victor Bloch, Avital Bechar and Amir Degani Fitness of Diverse Orchard Architectures on Optimal Robot Manipulator	6
Susana Brandão, Ana Viera, João P. Costeira, and Manuela Veloso, The Heat Based Rump Descriptor for Identification of Very Thin Goats in Dairy Farms.	11
Jonathon A. Gibbs, Michael Pound, Darren M. Wells, Erik Murchie, Andrew French, Tony Pridmore, Three-Dimensional Reconstruction of Plant Shoots from Multiple Images using an Active Vision System. ..	17
Z. Gobor, C. Cariou, B. Seiferth, S. Thurner, W. Feucker, C. Tessier, B. Tekin, and M. Berducat, Advanced pasture management through innovative robotic pasture maintenance.	23
Lars Grimstad, Huynh T. Phan, Cong D. Pham, Pål J. From, Initial field-testing of Thorvald, a versatile robotic platform for agricultural applications.....	30
Georg Halmetschlager, Johann Prankl, and Markus Vincze, Increasing the Precision of Generic Crop Row Detection and Tracking and Row End Detection.	36
Raghav Khanna, Joern Rehder, Martin Möller, Enric Galceran and Roland Siegart, Studying Phenotypic Variability in Crops using a Hand-held Sensor Platform.	40
Alexander Jairo Rojas Malaver, Luis Felipe Gonzalez, Nunzio Motta, Tommaso Villa, and Victor Etse, Design and Flight Testing of an Integrated Solar Powered UAV and WSN for Greenhouse Gas Monitoring Emissions in Agricultural Farms.	45
Cagatay Odabasi and H. Isil Bozma, Attentively Finding and Moving Among Apples.....	51
Timo Oksanen, Robotic mowing of agricultural grass fields with spatial variability using adaptive cruise control system.....	56
Bastiaan A. Vroegindeweyj, Steven van Hell, Joris IJsselmuiden and Eldert J. van Henten, Object segmentation in poultry housings using spectral reflectivity.	60
Stephen Wilshusen and Stephen Nuske, Recognizing Apples by Piecing Together the Segmentation Puzzle.....	66
Program Committee	72

Objectives

The world population is expected to reach 9 billion inhabitants by 2050. Producing food to feed such a large population will significantly increase the strain already in place on production environments and inputs, especially land and water. It furthermore proves to be difficult already now to find skilled and motivated workers and to keep the production costs low. To meet this important societal challenge, research and development in the agri-food sector is of utmost importance. One important direction is towards increasing automation and robotisation of the industry to improve the efficiency of its processes, reduce waste and costs, and improve food quality and safety.

The challenge of natural variation

Where some other industries, such as the automotive industry, are already highly robotized, the agri-food industry is still very labor intensive. This discrepancy is mainly due by the fact that agricultural robots need to deal with natural products in natural environments. The main challenges for robotics in this area lie with the variation in (a) products (between and within species), (b) environmental parameters (light, soil, humidity, seasonal factors etc.), and (c) tasks (pre-harvest maintenance, harvesting, and post-harvest processing). Although automation and robotic system exist for performing specific tasks on specific crops in specific environments, these are often not economically viable due to their limited application. We therefore believe that the main research challenge in agri-food robotics is to improve flexibility and robustness to deal with these variations.

With recent advances in horticulture and food production, agri-food is more and more being produced in semi-controlled environments. Examples include high-density orchards, where fruit literally grows in "fruit walls," modern greenhouses, etc. Parts of the environments are controlled, such as the type of product, and cultivation parameters, but on the other hand, there is always the previously-discussed variability of the product and the environment due to the inherent biological nature which is unstructured and uncontrolled. Semi-controlled environments allow the use of top-down model-based design methods, whereas uncontrolled environments need methods that are robust to the variability. The agri-food domain requires robotic research in both areas combined.

Application domains can range from more controlled, e.g., food inspection and packaging, to more uncontrolled, e.g., crop maintenance and harvesting in the open field, where the more controlled domains have potential to develop applications on short term, whereas more long-term fundamental research is required to handle less controlled situations.

Workshop's aims

In this workshop, we aim to bring together IROS attendees dedicated to or interested in solving some of the more pressing agri-food sector problems, specifically towards improved robustness and flexibility in dealing with variability in products, environments, and tasks. Our goal is furthermore to increase awareness of the important research topics and challenges in agri-food robotics and to promote interaction between researchers from different backgrounds in order to propel research in this area.

Topics of interest

Topics of interest addressed by this workshop include, but are not limited to robotic research in the following application domains:

- Crop maintenance
- Crop inspection
- Weed detection and removal
- Indoor navigation (greenhouses)
- Outdoor navigation (open field)
- Crop thinning and pruning
- Crop yield estimation
- Disease detection
- Harvesting
- Food-quality inspection
- Food grasping and manipulation
- Packaging

Support by IEEE RAS AgRA TC

This workshop is supported by the IEEE RAS Technical Committee on Agricultural Robotics and Automation (AgRA TC)

Organisers

The workshop was organised by:

Gert Kootstra (corresponding organiser)
Computer Vision and Robotics, Post-Harvest Technology,
Wageningen University and Research Centre
The Netherlands
gert.kootstra@wur.nl

Yael Edan
ABC Robotics Initiative
Ben-Gurion University of the Negev
Israel

Eldert van Henten
IEEE TC on Agricultural Robotics and Automation, and
Full professor at the Farm Technology Group
Wageningen University
The Netherlands

Marcel Bergerman
IEEE TC on Agricultural Robotics and Automation, and
Senior Systems Scientist at the Robotics Institute,
Carnegie Mellon University,
United States

Peer-reviewed papers

Submitted papers were subject to thorough peer-reviewing process, with peers selected from the members of the Program Committee. The PC selected twelve papers for oral and poster presentations. The remainder of this document provides the full texts of these contributions.

For citing the papers in your own work, please use the following standard:

[*authors*] (2015) [*title*]. In G. Kootstra, Y Edan, E van Henten, and M Bergerman (Eds.), *Proceedings of the IROS Workshop on Agri-Food Robotics*. Hamburg, October 2, 2015.

Fitness of Diverse Orchard Architectures on Optimal Robot Manipulator

Victor Bloch, Avital Bechar and Amir Degani

Abstract— Achieving a low cost robotic arm is crucial in agricultural applications. Task based optimization of the robot kinematics influence the robot simplicity and cost. Nevertheless, the environment of the robot also has a major influence on its simplicity. We have simulated a variety of orchard architectures and searched for an optimal robot design for each architecture. From the training systems which we considered, the Tall Spindle system provides the minimal average time for fruit picking and thus is preferable for robotic harvesting.

I. INTRODUCTION

Despite decades of research on robotic applications in agriculture, commercial agricultural harvesters are sparse or even nonexistent [1], [2]. Among others, the two main reasons are high cost of existing (industrial) robots and serviceability, making them unprofitable for farmers; and agricultural environment complexity, causing the sensing and motion planning of the robot to be complicated, time consuming and therefore impractical.

For agricultural applications, robotic arms are often tailor designed. They strive to be “light, simple and cheap” such as the arm for kiwi harvester [3]. Moreover, the robots are in some cases optimized for a specific task, such as an optimal robot for cucumber harvesting [4], or an optimal robot for eggplant harvesting [5]. However, up until now, the optimization was focused mainly on the robot component of the robot-environment system.

In the manufacturing domain, the robot environment is defined as the robot cell. Design of the robotic cells intended for throughput optimization is well studied and helps to solve numerous industrial challenges [6]. The main methods of the cell design are effective scheduling, multiple gripper usage, and parallel working robot usage.

Simplification and structuration of the agricultural environment is noted [2]. Nevertheless, design or optimization of the environment has not been performed. Such optimization is difficult because of the large number of optimization parameters, the difficulty in reaching the desired design, the extensive work required to design a tree and the required knowledge of the plant behavior (e.g., parameters of the L-systems [7]). Evaluation of the effectiveness of the existing environment types is performed in this paper as a preliminary step to the environment optimization.

Victor Bloch and Amir Degani are with Faculty of Civil and Environment Engineering, Technion, 32000 Haifa, Israel (Tel: 972-48292632; e-mail: {victorc, adegani}@technion.ac.il).

Victor Bloch and Avital Bechar are with Agricultural Research Organization (ARO), Volcani Center, Agricultural Engineering, 50250 Bet-Dagan, (e-mail: avital@volcani.agri.gov.il).

Different training systems (orchard architectures) of the fruit trees represent clearly different robotic environments. Modern high plant density training systems, such as the Tall Spindle (Figure 1 b), and Y-trellis (Figure 1 c), were developed mainly for increasing the yields and quality of fruit [8], [9]. In addition, they save labor time during harvesting, providing a convenient environment for the human harvesters. This advantage can also be used to provide an environment suitable to robotic harvesters, turning them into a profitable harvesting solution. The goal of this research is to evaluate the fitness of these training systems to robotic harvesting.

II. PROBLEM DESCRIPTION AND FORMULATION

A. Environment Modelling

Three apple trees trained by Central Leader (CL), Tall Spindle (TS) and Y-trellis (YT) training systems were modeled as the robot environment (Figure 1). The tree model consists of cylinders modeling the segments of the branches and the trellis parts, ellipsoids modeling the fruits and a plane modeling the ground. The leaves were not modeled in this preliminary examination. The environment coordinate system has its origin in the point of intersection of the ground plane with the tree trunk. The Z-axis is directed upward perpendicular to the ground plane, the Y-axis is parallel to the tree row, and the X-axis complements the right handed system.

The CL tree was modeled with the help of a mechanical digitizer developed for this purpose [10], the TS tree was reconstructed from pictures, and the YT tree was approximated by tuning the parameters of the L-systems and Markov chain. Future comprehensive studies will be based on tree models achieved by the digitizer.

B. Robot Performance Cost Function

Robot performance cost function is used to evaluate the effectiveness of the robot. The effectiveness depends on the customer’s demands, thus, the cost function cannot be strictly defined for the general case. One of the most common requirements in robotic applications is minimization of the robot performance time, which we use in this research. We study the mechanical aspect of the robot performance, hence, we consider only the time of the robot motion, which is defined here as the robot performance cost function F . This function depends on the robot geometry and the power of the robot actuators.

Exact calculation of the performance time is also nearly impossible in the general case. The time depends on parameters such as actuator power and weight, construction material, etc., which are defined by the designer. In order to find the optimal robot for our case study, the performance

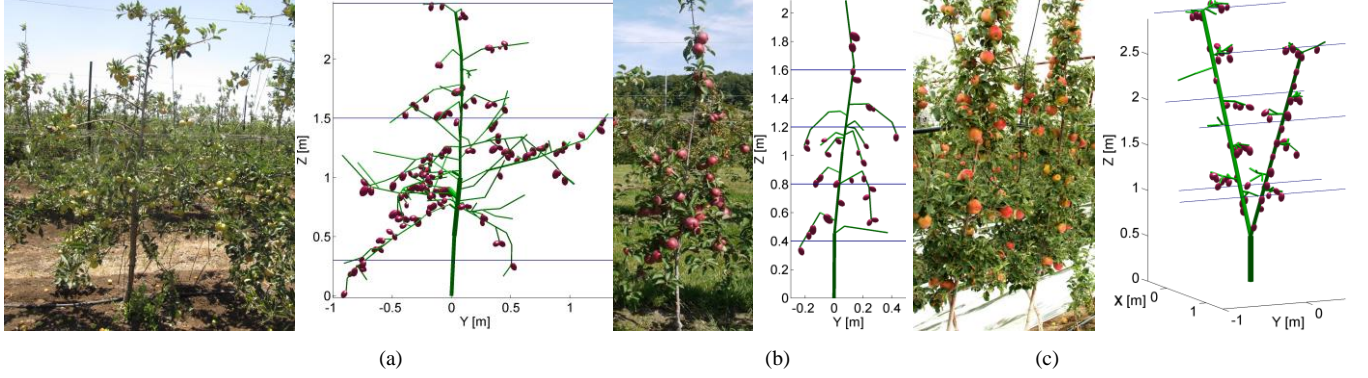


Figure 1. Three actual task environments and their models: apple trees trained by Central Leader (a), Tall Spindle (b) and Y-trellis (c) training systems.

time is evaluated by making several assumptions on the robot actuators and structure.

- Robot arm kinematics is predefined as a 3-degrees of freedom (DOF) with revolute or prismatic joints and general Denavit–Hartenberg (DH) parameters table. The number of DOF is denoted as N_{DOF} .
- Actuators are considered massless, assuming that the actuators are mounted on the robot base and are transmitting forces through beams or cords similar to the actuating system presented in [3].
- The length density of the robot links is taken as 1.5kg/m (similar to the density of a 3mm thick aluminum tube with a diameter of 60mm).
- The mass of the load is taken as 0.1kg (assumed as the mass of an average apple).
- The power of the robot actuators is taken with specific values: 100W is the power of the actuator in the first robot joint actuating the weight of the entire robot. The power of the rest of the actuators decreases proportionally to the weight of the link moved by the actuator.
- Time spent moving the mobile platform is not included in the cost function (because of the large variety of platform types). Nevertheless, a designer working with a specific mobile robot can take the moving time into account while evaluating the total robot cost function.
- The robot places the picked fruit in a gathering bin adjusted to the robot platform. Thus, the robot task must consist of the following stages: moving the end-effector from the robot home configuration to a fruit, approaching the lower hemisphere of the fruit, and retracting back to the home configuration.

The precise computation of the time and energy of motion is cumbersome for mechanical systems with three or more DOF. Therefore, the time is approximated with the help of basic physical expressions. Assuming the robot geometry, link masses and inertia and actuator power, the time spent for picking a specific fruit is

$$t_{fr,i} = \max(E_i/W_i), \quad (1)$$

where E_i is the energy consumed by the i 's actuator, and W_i is the power of the i 's actuator.

The energy $E_{fr} = \sum_{vi} E_i$ needed for the picking of a single fruit is the energy of the robot's movement from its initial home configuration q_i to a final configuration q_f set for picking the fruit. Therefore, the energy is calculated as

$$E_{fr} = E_d + E_s + E_{damp}, \quad (2)$$

where E_d is the dynamic work against the inertia of the robot and the load, E_s is the static work against the load and the robot's weight, and E_{damp} is the damping work against the friction in the robot joints. Friction in the robot joints depends on the gearbox parameters chosen by the designer, hence, it is disregarded therein. The static work is evaluated as

$$E_s = \int_{q_i}^{q_f} \tau(q) dq. \quad (3)$$

The torques produced by the actuators τ are calculated with the help of the transposed Jacobian

$$\tau = J^T P, \quad (4)$$

where P is the force acting on the robot, consisting of the weight of the load and of the robot links, which are all directed in the negative Z -axis direction. The mass of each link is calculated by the link length and length density, with the weight applied at the middle of each link.

The dynamic work, E_d , is calculated by

$$E_d = \int_{q_i}^{q_f} I(q) \ddot{q} dq, \quad (5)$$

where I is the inertia of the robot links and load, depending on the robot configuration. It is assumed that the acceleration has a maximal value (bang-bang control), hence, it is taken as a constant. Finally, the dynamic work can be approximated as

$$E_d = \ddot{q}_{max} \int_{q_i}^{q_f} I(q) dq. \quad (6)$$

The cost function F is the average fruit picking time for all picked fruits N_{picked}

$$F = \left(\sum_{i=1}^{N_{picked}} t_{fr,i} \right) / N_{picked}. \quad (7)$$

The cost function F is measured in units of time (seconds). The time calculation is approximated and simplified, and does not include important, but non-mechanical and difficult to define factors such as fruit recognition time, trajectory planning time, time for fruit

detachment and placement in the gathering bin, etc. Therefore, the achieved time values are different from the values reported in previous researches, such as [4].

C. Optimization Parameters

The parameters of the optimization are the known DH convention parameters α , θ , a and d [12]. The total number of parameters defining the robot kinematics is $4 \times N_{DOF}$. The parameters representing the robot's degrees of freedom (θ and d) are found by solving the inverse kinematics at a specific configuration of the robot. Thus, the total number of free unconstrained optimization parameters is $3 \times N_{DOF}$.

Type and order of the robot joints can strongly affect the applicability of the robot structure to different environments. For a 3-DOF robot we checked the following orders: RRR, RRP and PPP.

The location of the robot base constitutes additional optimization parameters. Each location is defined by two parameters: X and Y coordinate on the ground plane. Searching the optimal base location is decoupled from the optimization of the robot kinematics, and is found for a given number of robot locations N_{loc} by the grid search method with the branch and bound algorithm [11].

We also define the limits of the optimization parameters fitted to the task as follows:

- α parameter is in the interval $[-\pi, \pi]$,
- θ parameter is in the interval $[-\pi, \pi]$,
- a and d parameters are taken in the interval $[0,3]$, considering that the height and width of orchard trees do not exceed 3m,
- similarly, the X and Y coordinates of the robot base location are taken from the interval $[-3, 3]$.
- The limits of the robot DOF depend on the mechanical design of the robot. Hence, in this paper the robot revolute parameters θ are inside the interval $[-\pi, \pi]$, and the robot prismatic parameter d is taken from the interval $[0,3]$.

D. Optimization Constraint

The environment constraint is a set of geometric models of all obstacles and targets in the robot task environment. Interaction with these objects influences the robot motion: the robot must approach a target without collision with the obstacles.

To make the environment constraint more realistic, the allowed unpicked fruit percentage is defined. This percentage depends on the economic aspects of the fruit picking. In this paper, the percentage is taken 5%, meaning that in order to fulfill the task, the robot must be able to approach at least 95% of the targets.

E. Optimization and Navigation Algorithm

The optimization problem has a relatively large number of parameters, $3N_{DOF}=3 \times 3=9$, and a long function evaluation time: 2 to 20 minutes, depending on the tree. On average, the inverse kinematics solution takes 10% of this period of time, and the robot navigation solution with collision check takes

90%. To solve this problem, a Genetic Algorithm is used with a population size of 200 and a mutation rate of 20%.

The rapidly exploring random tree (RRT) algorithm [13] is used as the planner of trajectories between the robot home position and the robot targets (fruit). The RRT uses 100 vertices and an incremental distance of 0.03m. The original version of RRT was implemented.

F. Environment Fitness Evaluation

The agronomical and economical aspects of the tree shaping, such as fruit quality and yields, are out of scope of this research. Hence, these aspects are not considered in the evaluation of the environment fitness to the robot performance (especially, considering the fact that originally the tree training was being performed for purposes not connected with robotic harvesting).

In order to find the environment fitness evaluation, we calculate a single fruit picking average time. The lower the average time is, the more fitted the environment is to the robotic harvester.

III. RESULTS AND DISCUSSION

A. Optimal Robots for Different Environments

Three optimal robots for different environments are shown in Figure 2. For illustrations of the robot kinematics for each robot location, several fruits and robot homing configurations are presented in the upper part of Figure 2. The unpicked fruit are colored in black.

The trajectories of the end-effector from the homing configuration to the fruit picking configuration are shown in the lower part. We can observe that the shorter the trajectories are, the shorter the motion time is and, therefore, the robot is more optimized.

Table 1 shows the relation between the environment types, the robot cost function F , the order and type of the joints, and the number of robot locations around the tree N_{loc} .

In all the environments and robot types we can observe that the cost function value decreases as the number of locations around the tree N_{loc} increases. The reason for this dependence is that the robot working volume is divided into smaller parts as the number of the robot locations increases. As a consequence, the smaller the working volume, the shorter the lengths of the robot links and the smaller their

TABLE I. AVERAGE COST OF THE FRUIT PICKING BY THE OPTIMAL ROBOT FOR DIFFERENT ENVIRONMENTS

Joint type	N_{loc}	Central Leader	Tall Spindle	Y-Trellis
		F [second]		
RRR	2	0.81	0.35	0.44
	4	0.64	0.3	0.42
	6	0.58	0.24	0.38
	8	0.55	0.23	0.37
RRP	2	0.33	0.17	0.27
	4	0.27	0.15	0.25
	6	0.26	0.12	0.21
	8	0.26	0.1	0.2
PPP	2	No solution	0.085	0.22
	4	0.4	0.079	0.17
	6	0.32	0.06	0.16
	8	0.32	0.06	0.16

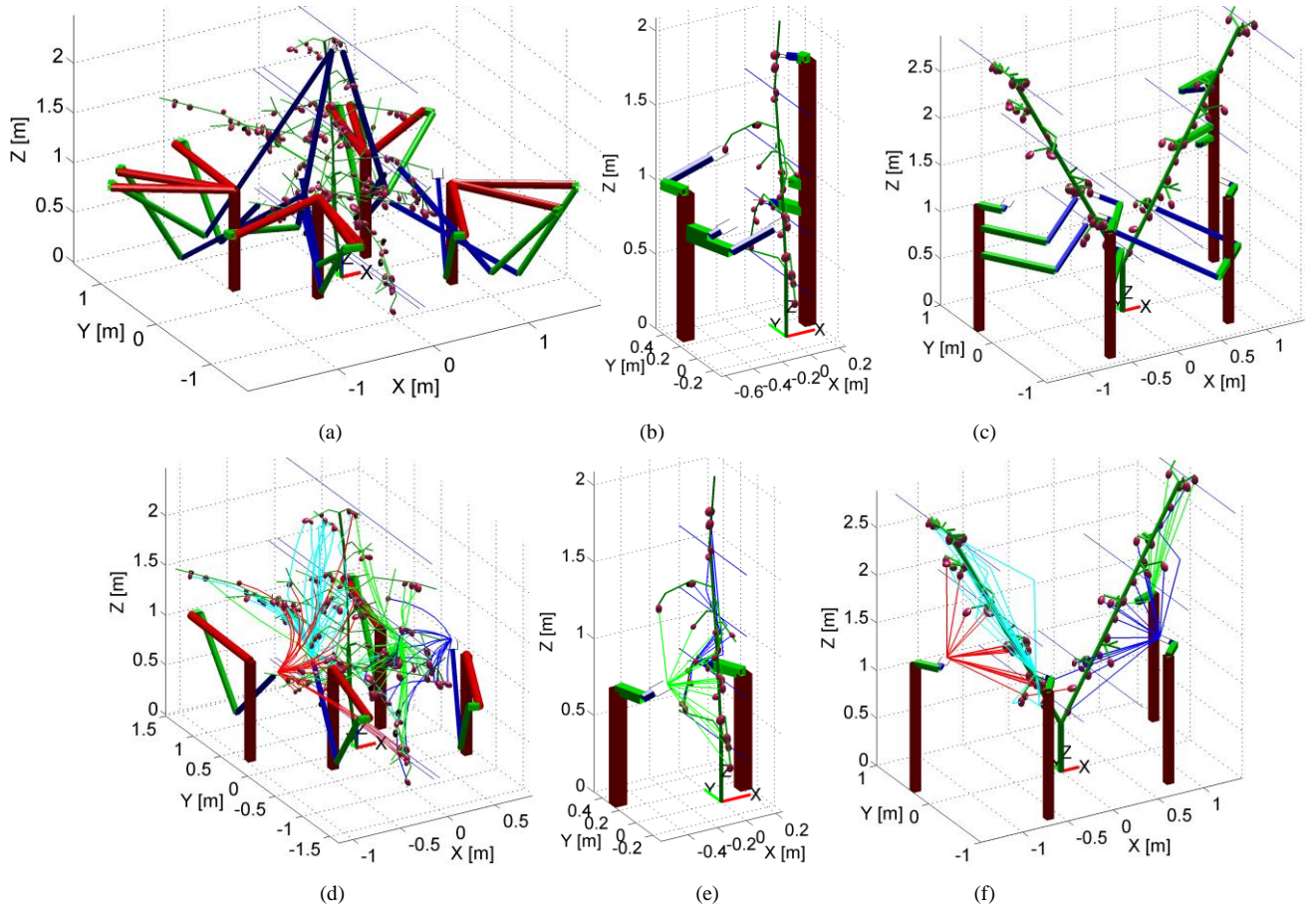


Figure 2. Optimal robots and their end-effector trajectories for Central Leader (a, d), Tall Spindle (b, e), and Y-trellis (c, f) apple trees. The robots are presented in the several configurations for fruit picking (upper row) and homing configurations (lower row).

masses are, resulting in a decrease in the energy and the time needed for their motion.

However, while the cost function decreases as the number of robot locations increases till six, for eight locations the cost function almost does not change. This can be observed in all robot types, and points at the fact that the larger number of robot locations has smaller efficiency.

Comparison of the robot types for each environment type shows that each environment has its most effective robot type, where the cost functions have minimal values: TS and YT environments have PPP, and CL environment has RRP. This is due to the geometrical features of the environments. Trees shaped by the TS and YT methods have relatively structured environments. As a result, most of the fruit is surrounded by open space without obstacles, which enables the robot to approach the fruit by a straight line in the workspace from any robot base location. This type of motion is typical for the PPP type robot. Trees shaped by the CL method have more fruit hidden by branches which constitute obstacles to the robot motion on a straight line. To approach them, revolute joints must be involved in the robot structure. The RRP type robot is suitable for this type of motion.

The fact that each environment type has a specific robot type best suited to operate in it enables an evaluation of the fitness of the environment to robotic harvesting. The simpler

the optimal robot is, the better fitted its designated environment will be to robotic harvesting.

Thus, according to the defined cost function, a prismatic joint is more effective than a revolute joint, since during the motion it changes only the position of its link and end-effector, while the revolute joint changes orientation as well as position for the same motion. Hence, the more prismatic joints a robot has, the more efficient it is. Consequently, TS and YT training systems are more effective than CL training systems, and, according to the cost function values, the TS method is more effective than the YT method.

B. Total Robot Motion Time Evaluation

The movements between the robot base locations must also be considered in the evaluation of the cost function for a row or entire orchard. The time of the movement depends on the platform carrying the robotic arm and is not evaluated here for the general case. To understand its influence, we propose to define the average movement time as 3 seconds (denoted as T_{mov}) and evaluate the time needed for picking 7920 fruit in orchards shaped by the considered methods.

We assume that the orchard consists of the modeled trees duplicated and located along the rows. The number of fruit on each tree, N_{fruit} , is given in Table 2. Hence, to model 7920 fruit, the row must include the following number of trees $N_{tree}=7920/N_{fruit}$ (given in Table 2). The total time for the

TABLE II. AVERAGE COST OF THE FRUIT PICKING BY THE OPTIMAL ROBOT FOR DIFFERENT ENVIRONMENTS

	<i>Environment and Tree Type</i>		
	<i>CL, RRP</i>	<i>TS, PPP</i>	<i>YT, PPP</i>
N_{fruit}	144	30	66
N_{tree}	55	264	120
$T_{tot} N_{loc}=2$	2944 sec	2257 sec	2462 sec
$T_{tot} N_{loc}=4$	2798 sec	3794 sec	2786 sec
$T_{tot} N_{loc}=6$	3049 sec	5227 sec	3427 sec
$T_{tot} N_{loc}=8$	3379 sec	6811 sec	4147 sec

fruit picking is calculated according to

$$T_{tot} = T_{fruit}N_{fruit} + T_{mov}N_{tree}N_{loc}, \quad (8)$$

where T_{fruit} is the average time for the fruit picking equal to the cost function value F . The total time for different N_{loc} and specific robot types is presented in Table 2.

The results presented in Table 2 show that the TS training system is the most effective. The total fruit picking time depends on the number of trees and the number of locations around a single tree, and has an optimal value (shown in bold), which is the tradeoff between the average fruit picking time and the number of movements.

IV. CONCLUSION

We propose to evaluate the fitness of the orchard tree architecture to robotic harvesting. The comparison of the robot performance cost function for different tree training systems shows that high density training systems have a structure that demands a simpler optimal robot to perform the fruit picking in less time. Therefore, these systems are better fitted to robotic harvesting than the conventional systems. In addition to the agronomical advantages of high density training systems [8], they provide automation advantages.

Tree training according to high density training systems is performed by growing high trees in high density and eliminating small branches. This provides three main advantages. Concentration of the fruit in a compact volume (near the row plane at TS and along the trellis at YT) shortens the robot's link lengths and enables the robot to shorten the time of movement between the locations around the tree. In addition, a plane-shaped tree (so called "fruit wall") enables the positioning of the robot close to its targets and orients its joints along the plane, making the end-effector motion close to two-dimensional and allowing the use of prismatic joints. Finally, the decreased number of branches provides a working volume with minimum obstacles. An additional non-mechanical advantage of tree training according to high density training systems is the decreased number of branches and leafs occluding the fruit, which can simplify fruit recognition.

The stochastic nature of the agricultural environment, which includes a large number of unordered objects, makes the designing process extremely time consuming. To complete a design in an acceptable amount of time, more effective methods, such as environment characterization [10], should be applied.

Future work must consider the following generalizations. Agricultural environment has a large deviation in its geometrical features even for trees taken from the same row in an orchard [10]. Hence, a single plant cannot represent the entire orchard. To achieve an optimal and robust robot and a reliable evaluation of the training system fitness, we must collect enough sampled data (tree models) characterizing the tree training system. Nevertheless, we have to take into account that a large dataset leads to a growth in the computation time. To address this problem and to shorten the optimization time, our method described in [10] can be used. The method is based on building an average, characteristic tree model with the help of the minimal amount of data sufficient for the optimization.

Trellis cables and supports represent obstacles for the robot. We will try to offer engineering recommendations defining the positioning of these supports in a way which minimizes their interference with the operation of the robot.

Methods of describing the environment, such as L-systems and Markov chains, can be used as parameters for an optimization of the environment best suitable to robotic harvesting.

REFERENCES

- [1] A. Bechar, "Automation and robotic in horticultural field production," in *Stewart Postharvest Review*, 6(3), 1-11, 2010.
- [2] C. W. Bac, E. J. Van Henten, J. Hemming, Y. Edan, "Harvesting Robots for High-value Crops: State-of-the-art Review and Challenges Ahead," in *Journal of Field Robotics*, 31(6), 888-911, 2014.
- [3] A. J. Scarfe, R. C. Flemmer, H. H. Bakker, C. L. Flemmer, "Development of an autonomous kiwifruit picking robot," in *Autonomous Robots and Agents, 4th International Conference*, 380-384, 2009.
- [4] E. J. Van Henten, D. A. Van Slot, C. W. J. Hol, and L.G. Van Willigenburg, "Optimal manipulator design for a cucumber harvesting robot," in *Computers and Electronics in Agriculture*, 65(2), 247-257, 2009.
- [5] S. Han, S. Xueyan, Z. Tiezhong, Z. Bin, and X. Liming, "Design optimisation and simulation of structure parameters of an eggplant picking robot," in *New Zealand Journal of Agricultural Research*, 50(5), 959-964, 2007.
- [6] M. W. Dawande, H. N. Geismar, S. P. Sethi, C. Sriskandarajah, "Throughput Optimization in Robotic Cells," in *International Series in Operations Research & Management Science*, vol. 101, 2007, 420 p.
- [7] J. Hua, M. Kang, "Optimize Tree Shape: Targeting for Best Light Interception," in *Proceedings of the 7th International Conference on FSPM*, 27-29, 2013.
- [8] T. L. Robinson, A. N. Lakso, Z. Ren, "Modifying Apple Tree Canopies for Improved Production Efficiency," in *HortScience*, vol. 26, no. 8., 1991, pp. 1005-1012.
- [9] M. Bergerman, S. Sanjiv and B. Hamner, "Results with autonomous vehicles operating in specialty crops," in *Robotics and Automation International Conference on. IEEE*, 2012.
- [10] V. Bloch, A. Bechar, A. Degani, "Development of an Environment Characterization Methodology for Optimal Design of an Agricultural Robot," in preparation.
- [11] P. T. Kolesar. "A Branch and Bound Algorithm for the Knapsack Problem", in *Management Science*, vol. 13, No. 9, May 1967.
- [12] J. J. Craig. "Introduction to Robotics: Mechanics and Control," Pearson/Prentice Hall, 400 pages, 2005.
- [13] S. M. LaValle. "Planning algorithms," Cambridge University Press, 842 pages, 2006.

The Heat Based Rump Descriptor for Identification of Very Thin Goats in Dairy Farms

Susana Brandão¹, Ana Vieira², João P. Costeira³, Manuela Veloso⁴

Abstract—In this paper we address the problem of identifying goats in dairy farms with sub-optimal values of Body Condition Score (BCS). The BCS conveys information on whether an animal is fat or thin and its identification has a strong economic impact as very thin animals have poorer milk production and associated health problems. Albeit its important implications, not only there is no automated way of assessing the BCS in dairy farms, but current available techniques require specially trained personnel. However, the recently introduced Pictorial Scale for BCS assessment in dairy goats shows that the rump region has several visual cues strongly correlated with animal’s BCS values. In this paper we move towards the automatic assessment of BCS by developing a descriptor for rump’s 3D surfaces, collected by an RGB-D camera. The use of 3D surfaces as the basis for identification is fundamental, as it allows data collection without requiring animal handling to ensure careful alignment between camera and animal. However, the identification of the rump region in the 3D surfaces is very difficult, which leads to a large variability in the type of surfaces associated with the same BCS value. The descriptor we here introduce, the Heat Based Rump Descriptor (HBRD), uses diffusion geometry concepts to seamlessly handle the difficulty in defining a rump region and the resulting large variability of shapes. We test our descriptor in a dataset of 32 dairy goats and show that our descriptor is able to effectively cluster all the very thin animals.

I. INTRODUCTION

The Body Condition Score (BCS) is correlated with an animal fat deposits and is an important animal-based indicator of animal welfare. Furthermore, very low BCS, as those represented in Fig. 1(a), are also correlated with low milk production [1] and are not in adherence with consumers expectations on animal’s welfare [2].

European Union, having recognized the farm animals’ right of freedom from hunger and thirst, is currently moving towards the introduction of BCS as a key indicator on welfare assessment protocols on goat farms. However, standard techniques for estimating the BCS in goats, e.g., as those presented in [8], cannot be used in large scale assessments, as they require restraining and handling of each animal individually by specially trained assessors.

The recently introduced Visual Body Condition Scoring System, [15], addresses the scalability problem by creating illustrations to allow non-experts to assess the BCS by visual



Fig. 1. Examples of very thin, normal and very fat animals at different distances and orientations from a RGB-D camera. Each animal was manually evaluated to assess its BCS score.

inspection. For the construction of the Pictorial Scale, authors identified several visual features in the rump region that are strongly correlated with the animal BCS. Those features correspond to distances between bones and muscle folds, which are easy to visually identify. The features were used to define a *standard* individual of each class, from which a professional illustrator generated drawings for the Pictorial scale. The Pictorial scale can now be used in farms, but still requires trained evaluators.

The features identified in [15] worked well for the purpose of creating visually accurate illustrations. However, to retrieve such features, authors acquired photographs taking careful control on conditions such as: i) animals’ stillness; and ii) rumps’ alignment with the camera, which are difficult to ensure without animal handling. In this paper we move towards a scenario where no handling is required by using RGB-D cameras, as 3D information handles better changes in the orientation between camera and animal. Such cameras can be fixed on top of the animals’ normal path, and can accurately collect data at roughly 2m from the animal.

RGB-D cameras, such as the Kinect camera, provide both an RGB image and a depth image, from which we can recover 3D surfaces corresponding to the animal surface. From the whole animal, we extract the rump as showed in Fig. 2 using a manual labeling approach similar to the one presented in [15].

As noted in [15], the main difference between different

¹Susana Brandão is with ECE at CMU, USA and IST-UL, Portugal. sbrandao@ece.cmu.edu

²Ana Vieira is with Veterinary School at FMV-UL, Portugal. ana.lopesvieira@gmail.com

³João P. Costeira is with Faculty with ECE at IST, Portugal. jpc@isr.ist.utl.pt

⁴Manuela Veloso is with Faculty with CS, CMU USA. mmv@cs.cmu.edu

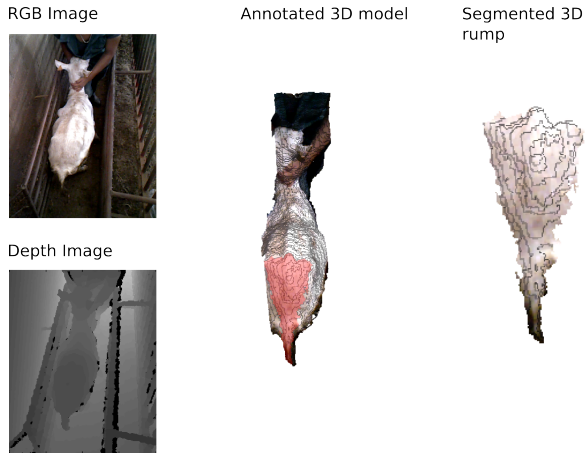


Fig. 2. Acquiring rumps' 3D surfaces.

BCS categories are the fat reserves in the rump, which yield a bulkier appearance in fatter animals. To correctly assess the animal class, we focus on descriptors that represent changes in the volume between rumps of different animals. Furthermore, the most noticeable changes in the rump volume concern its upper part, near the hip.

However, the direct comparison of volume between rumps 3D surfaces is very challenging, as: (i) rump shapes vary considerably between animals, regardless of BCS, as showed in Fig.1; and (ii) it is difficult to consistently define the rump region in a meaningful and consistent way.

Without a clear definition of the region of interest, we cannot compare two surfaces. In fact, from the several descriptors available for the recognition of 3D shapes,[16], [10], [3], none that we are aware of handles the problem of representing a shape that itself is ill defined. We thus propose to assess the changes in volume from one surface to another based on how much they differ from a plane. Animals with rumps that are more similar to a plane, have smaller fat deposits, i.e., are thinner. By introducing an intermediary shape, we avoid mapping and registration between rumps.

To capture changes in this vague region of the upper part of the rump, without having to specifically segment it, we use multi-scale descriptors, i.e., descriptors that provide information on how a given point in the surface is related to the whole surface by considering increasingly large neighborhoods for that point. An example of such descriptors are Heat Kernel Signatures [13].

Heat Kernel Signatures and other heat based descriptors describe how connected a point is to its neighborhood by simulating heat propagating over a surface. In Fig. 3 we show several snapshots of the process of heat propagating from an initial heat source to the whole surface. At each fixed time instant, the temperature of a point in the surface is related to its distance to the initial source. Furthermore, as time passes, the temperature in points further from the source increases, while the temperature at the source decreases. The change in the temperature is more significant in the first instants, when there are sharp contrasts over the surface, than in the

end, when the temperature over the whole surface becomes constant, regardless of the surface shape.

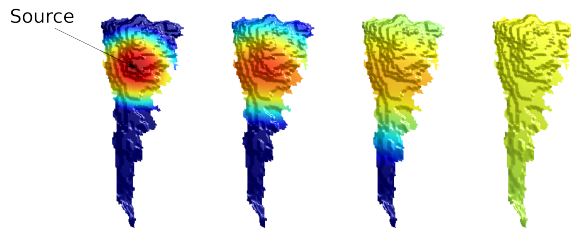


Fig. 3. Heat diffusion over a goat's 3D rump. Red corresponds to higher temperatures and blue to colder ones.

Thus, heat diffusion has two characteristics that make it the ideal choice of representation: (i) naturally introduces a notion of scale, and (ii) temperatures can be used as a surrogate to distances[3], specially when surfaces are noisy and have a poor resolution such as those from common RGB-D cameras.

In this paper we move towards the automatic identification of the body condition score of farm goats by introducing a Heat Based Rump Descriptor (HBRD) that:

- represents regions at different scales, allowing to focus on the upper part of the rump, without having to explicitly segment the region;
- describes the rump by comparing it against a default shape, in this case a plane.

Such descriptor allows to handle the variability in the animals' shape and the difficulty in defining the region of interest.

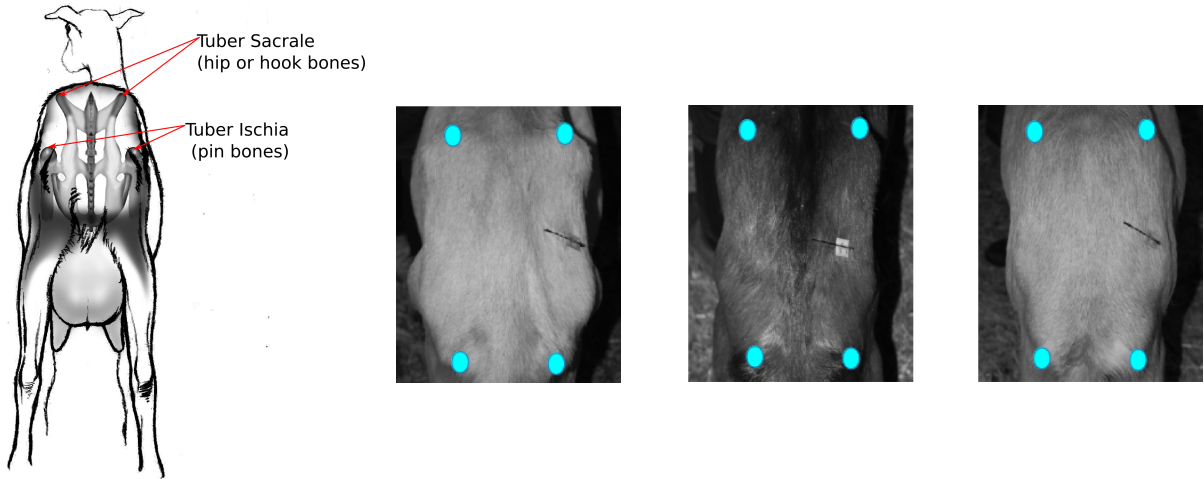
In the following we show how we obtain an initial segmentation of the rump region given the output of an RGB-D sensor, and we provide full detail on how to estimate HBRD descriptors in any given rump.

II. DATA ACQUISITION

While leaving the milking room, animals pass one by one through a narrow corridor. We placed a calibrated RGB-D sensor on a fixed point above the animals' path. An expert manually evaluated the animals' BCS to provide ground truth using the simplified 3 points scale defined in [15].

While we cannot identify accurately the rump region in the different animals, we follow [15] and define the region based on the rump bone structure, namely the tuber sacrale (hip or hook bones) and the tuber ischia (pin bones), represented in Fig. 4(a). The tips of these bones correspond to easily identifiable features in the RGB images of animals of all categories, as we show in Fig. 4(b)-(d).

From the depth image, D , we can recreate the goat 3D surface, as illustrated in Fig. 2. The surface corresponds to a set of triangles, represented by a list of vertex coordinates $X = [\bar{x}_1^T, \bar{x}_2^T, \dots, \bar{x}_N^T]$ and a set of edges $E = \{e_1 = (1,2), \dots, e_{N_e} = (k,N)\}$. Each vertex corresponds to a pixel in the depth image, and the coordinates are obtained by calibrating the sensor. We construct the set of edges based



(a) Detail on the rump bone structure. (b) Examples of photographs with annotated hip and pin bones.

Fig. 4. Rump identification: Detail on the bone structure of a goat rump, showing that hip and pin bones are part of the same structure and lay on the same plane, and photographs showing that the bones are easy to identify.

on adjacency relations between pixels in the depth image, creating a mesh of triangles that cover the surface, without overlap. From the camera calibration, we can also map the annotations in the RGB image, I , to the depth image, D , to obtain the 3D coordinates of the left and right hip bones, $\bar{h}_{l,r}$, and pin bones $\bar{p}_{l,r}$.

When the goat is standing, the four bone tips approximately define a plane, as the hip and pin bones are rigidly connected. By finding the orientation of the plane defined by the four bone tips with respect to the floor, we rotate the whole surface, so the bone tips lay in the $x-y$ plane. We define the rump as all the points with a positive z . This segmentation is reproducible and consistent, albeit it may lead to the inclusion of other parts of the animal in the rump, e.g., the tail.

To account for changes in the animal size, we normalize both x and y coordinates of all vertices, so that the bone tips of all the animals are in the same position $\bar{h}'_{l,r}$, $\bar{p}'_{l,r}$ in the $x-y$ plane. To account for possible hip or tip bones miss-alignment, we normalize using a projective transformation. The resulting normalized coordinates, $X_{norm} = [\bar{x}_1^{norm} = [x_1^{norm}, y_1^{norm}, z_1], \dots, \bar{x}_N^{norm}]$, maintain the same z -coordinate. The edges in the normalize surface connect the same vertices as the edges in the original one.

After segmentation and normalization, we obtain a set of rumps similar to those represented in Fig. 5.

III. RUMP DESCRIPTION

A. Representing variable surfaces

Rumps in Fig. 5 highlight that the most distinct feature among all rumps is that thin goats are almost flat. The rumps also illustrate the intra-class variation resulting from the natural variability of goats shapes and sizes. In particular, it shows that goats have different features that are not related with the BCS, e.g., rump boundaries change considerably

across animals, and in some animals the tail is included in our estimation of the rump region. We must also account for errors in the segmentation process, such as (i) there is a large uncertainty in the identification of hip and pin bones on the animals rump, (ii) it is difficult to ensure that the bone tips are in a plane, and (iii) errors in camera calibration result in errors in the map between RGB and depth images.

Common approaches for 3D shape representation, such as bag of features or 3D holistic representations are not effective in describing these variations, as they all assume that any input shape is fully explained by the category they want to represent and eventually classify. As far as we are aware, there is no previous work on the representation of 3D shapes where the shape itself was not explicitly defined.

We compare the differences in volume by extracting shape information, e.g., distances between points and areas, and compare it with the same information extracted from a planar projection, as showed in Fig. 6. The planar projection corresponds to the same mesh, but with z -coordinate set to zero, $X_{plane} = [\bar{x}_1^{plane} = [x_i^{plane}, y_i^{plane}, 0], \dots, \bar{x}_N^{plane}]$.

The comparison between the two surfaces is possible because there is a natural bijection relating the two surfaces, i.e., there is an one to one relation between points in the rump and in the planar projection. We thus compare the two surfaces by computing a geometry dependent function at each point and compare the values of both surfaces at related points.

As stated, in this work we use the temperature resulting from a heat diffusion process, as it provides a natural segmentation of the interest region and depends on the geometry of each surface, as it occurs faster in planar surfaces. Other functions, e.g., the distance to a point, also depend on the geometry of each surface, however require a rigorous definition of the interest region. We thus assess if the geometry of the two surfaces is similar by comparing the

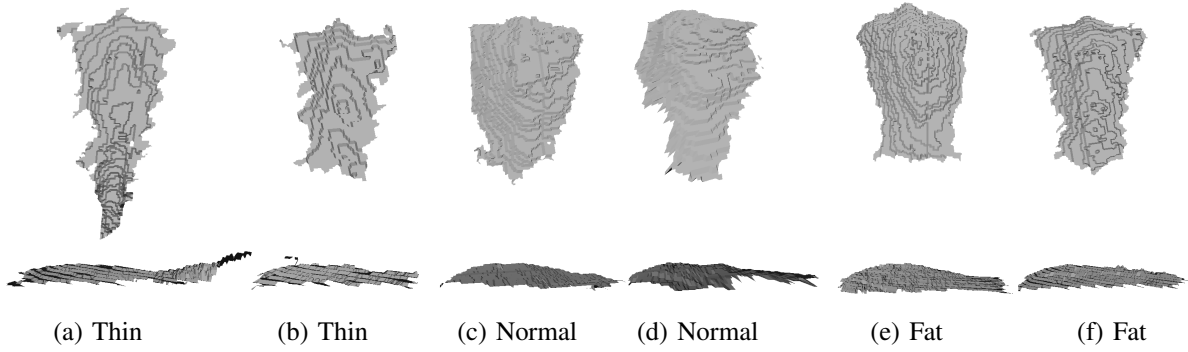


Fig. 5. Example of rumps from different animals. The top image represent a view from the z-axis, while the bottom view from the x-axis.



Fig. 6. Example of a planar rump, on the left, built from the regular rump on the right.

temperature at equivalent points in both surfaces.

B. Heat Diffusion on Discrete Surfaces

Heat based descriptors have shown good results at representing surfaces retrieved from depth sensor [3], [4], [5] and other 3D shapes [13], [6]. We here briefly review the necessary steps to compute a temperature $\bar{T}(t) \in \mathbb{R}^N$ on all the vertices in the surface, at each time instant t . The familiar reader may skip to section III-C.

Heat diffusion in discrete surfaces, such as the one obtained from depth images, is described by eq.1, [9]

$$\partial_t \bar{T}(t) = -L\bar{T}(t) \quad (1)$$

where L is the discrete Laplacian matrix, which is related with the Laplace-Beltrami operator defined in continuous surfaces [13]. Such operator returns the temperature second derivative as defined over the surface, i.e., taking into account that the surface is not necessarily a plane.

The discrete version we use in this work is associated with a graph interpretation of the organized set of points in the depth image. As showed in Fig. 7, each pixel i in the depth image leads to a vertex in the graph with coordinates \bar{x}_i . The vertices are connected by the triangle edges E and to each

edge $e = (i, j)$ connecting a vertex i to a vertex j there is an associated weight $w_{i,j} = \|1/\|\bar{x}_i - \bar{x}_j\|^2$.

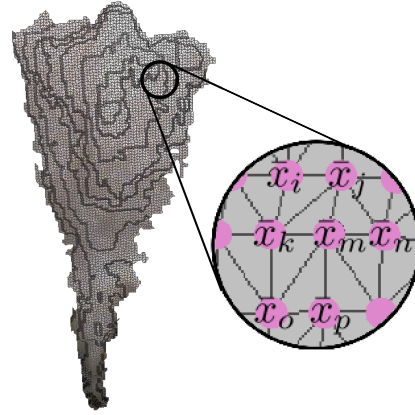


Fig. 7. Graph structure of surfaces retrieved with an RGB-D camera.

For a graph/surface with N vertices, the Laplacian is the $N \times N$ symmetrical matrix $L = D - W$, with $[W]_{i,j} = w_{i,j}$ if there is an edge connecting the vertex i and j , i.e., if $e = (i, j) \in E$, and 0 otherwise. D is a diagonal matrix, with $[D]_{i,i} = \sum_{j=1}^N [W]_{i,j}$. The resulting L matrix, using the above definition for the weights, corresponds to the finite differences approximation to the second derivative.

With Newman boundary conditions and an initial temperature over the surface equal to $\bar{T}(0)$, the temperature at any other time instant $\bar{T}(t)$ can be written in close form with respect to the eigenvalues λ_i and eigenvectors $\bar{\phi}_i$ of L :

$$\bar{T}(t) = \sum_{i=1}^{N_V} \bar{\phi}_i \exp\{-\lambda_i t\} \bar{\phi}_i^T \bar{T}(0). \quad (2)$$

C. Heat Based Rump Descriptors

We evaluate how much a rump differs from a plane by considering a heat diffusion process starting at its center and the equivalent vertex on its planar projection. Thus, the initial condition for both the temperature in the normalized surface $\bar{T}(0)$ and in the plane, $\bar{T}'(0)$ will be equal to each other and be zero everywhere except for some vertex c in the center of the rump, i.e., $[\bar{T}]_c = 1$ and $[\bar{T}]_i = 0 \forall i \neq c$.

The vertices at the center of both rumps, with coordinates \bar{x}_c , and $\bar{x}_{plane,c}$, are those closest to the center of the quadrilateral defined by $\bar{h}'_{l,r}, \bar{p}'_{l,r}$ in both X_{norm} and X_{plane} respectively.

For each animal, given the set of edges E and the two sets of vertex coordinates X_{norm} and X_{plane} , we compute the Laplacian for each surface, L_{norm} and L_{plane} . From each Laplacian we compute the first 300 eigenvectors and eigenvalues and, given the initial condition, $\bar{T}(0)$, we propagate the temperature at both surfaces using eq. 2. As to each point in the original surface corresponds a single point in the planar surface, we can compute the difference between the temperature at both surfaces, $\Delta\bar{T}(t) = \bar{T}_{norm}(t) - \bar{T}_{plane}(t)$ at each time instant.

We evaluate the time difference at exponentially large time intervals, as changes in temperature occur faster in the beginning. In particular, we use time instants $t_k = 0.1e^{-k\delta t}$, spanning from 1/700 to 1/10. We focus on the rump upper part by assessing $\Delta\bar{T}(t)$ at a subset of vertices \mathcal{S} that form the shortest path in the planar mesh between \bar{x}_c and \bar{h}'_l , which we compute using the Dijkstra algorithm [7].

Finally we construct the descriptor, \bar{z} by considering, for each time instant t_k , the maximum of $\Delta\bar{T}(t_k)$ over the subset of vertices \mathcal{S} , i.e.,

$$\bar{z}: [\bar{z}]_k = \max_{x \in \mathcal{S}} [\Delta\bar{T}(t_k)]_x \quad (3)$$

The main steps for computing HBRD are highlighted in Algorithm 1. The algorithm requires as input an RGB image, I , a Depth image, D , which we here assume that is already mapped into the RGB image. As fixed input parameters, the algorithm further requires the time instants at which we compute the temperature, \bar{t} , and the coordinates of the left and right hip and pin bones in the normalized rump, $\bar{h}'_{l,r}, \bar{p}'_{l,r}$. In this study, the position of the bone tips in the RGB image $\bar{h}_{l,r}, \bar{p}_{l,r}$ is provided by the user, however we expect that this step can be automated using feature matching and taking advantage of the 3D information provided by the depth image, as in [12].

IV. RESULTS

We used Algorithm 1 to describe different animals.

Fig. 8 shows that temperature in thinner animals converges faster to that the planar rump. The figure represents four rumps, two very thin and two normal. The colors represent the absolute difference between the temperature in the rump to the planar rump. The black line in the upper left part of each rump corresponds to the shortest path \mathcal{S} .

Fig. 9 shows the descriptors for the animals in Fig. 8. There is a clear difference over the maximum of the difference between normal and thin animals. Furthermore, we note that by looking only into what happens on the top part of the rump, the animal's tail has little impact on the temperature on the top part of the rump.

Finally, we show that HBRD differentiates thin animals among a dataset of 32 animals, 9 thin, 17 normal and 6 fat. Fig. 10 shows the 3D-Isomap projection[14] of the set of descriptors. The Isomap projection, similarly to PCA projections[11] allows to visualize data of high dimension.

Algorithm 1: Heat Based Rump Descriptor (HBRD).

Input: RGB image: I ; Depth image: D ; Time instants: \bar{t} ; bone tips in the normalized rump: $\bar{h}'_{l,r}, \bar{p}'_{l,r}$

Output: Rump descriptor, \bar{z}_r .

Manually Annotate Hip and Pin Bones in the RGB Image:

$[\bar{h}_{l,r}, \bar{p}_{l,r}] \leftarrow \text{annotate}(I)$

Segment and Normalize depth image:

$[X_{norm}, E] \leftarrow \text{segmentNormalize}(D, \bar{h}_{l,r}, \bar{p}_{l,r}, \bar{h}'_{l,r}, \bar{p}'_{l,r})$

$X_{plane} \leftarrow \text{project}(X_{norm})$

Find Path Between Center and Left hip bone:

$\bar{x}_c \leftarrow \text{centroid}(\bar{h}'_l, \bar{h}'_r, \bar{p}'_l, \bar{p}'_r)$

$\mathcal{S} \leftarrow \text{dijkstraShortestPath}(\text{mesh}, X_{plane}, \bar{h}'_l, \bar{x}_c)$

for $i = 1; i < \text{size}(\bar{t}); i++$ **do**

 Estimate both temperatures distributions, from eq 2:

$\bar{T}_{norm}^{\mathcal{S}} \leftarrow \text{propagateHeat}(X_{norm}, E, \mathcal{S}, [\bar{t}]_i)$

$\bar{T}_{plane}^{\mathcal{S}} \leftarrow \text{propagateHeat}(X_{plane}, E, \mathcal{S}, [\bar{t}]_i)$

$\Delta T([\bar{t}]_i) = \bar{T}_{norm} - \bar{T}_{plane}$

 Get descriptor, from eq 3:

$[\bar{z}_r]_i \leftarrow \max(\Delta T([\bar{t}]_i))$

end

However, Isomap provides a representation which minimizes distortion of the distances over nonlinear subspaces, in contrast to PCA that assumes linear subspaces and euclidian norms.

Results show that very thin animals are well clustered, i.e., that the Heat Based Rump Descriptor captures a very elusive characteristic. Some supervised machine learning algorithm can then be trained using these descriptors and used for automatic classification. Support vector machines would be good candidates for classification. We further note that, by introducing a comparison surface that shares with the original rump most of the characteristics that are not intrinsic to the class, e.g., the tail, we obtained a descriptor that correctly represents the class dependent characteristics.

V. CONCLUSIONS AND FUTURE WORK

In this paper we introduced the Heat Based Rump Descriptor (HBRD) for the identification of very thin goats in dairy farms. The identification of such animals is of utmost relevance not only by the economic implications of the decrease in the milk production associated with a low BCS, as it is in direct violation of the animal's rights.

The HBRD assesses the BCS by the rump volume. To handle the large variability of animal shapes and the difficulty of exactly setting the limits of the relevant part of the rump, HBRD uses heat diffusion to represent distances between points in two equivalent surfaces. The volume is assessed by having the surfaces differ only on the characteristic that we want to measure, i.e., the volume. The use of heat diffusion allows to soft segment the region of interest, as the difference in temperature in both surfaces will be more significant in

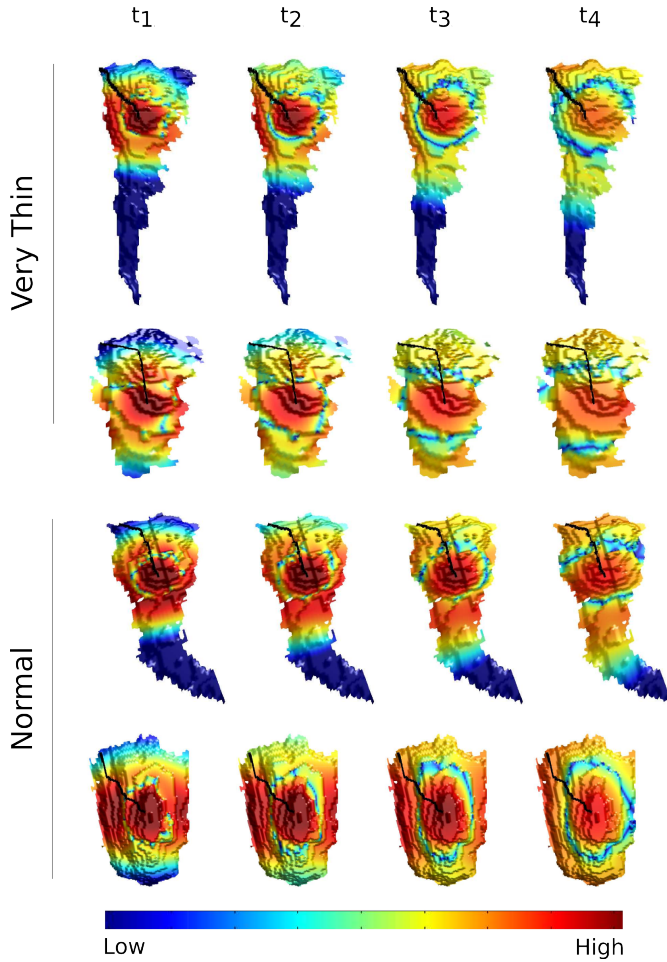


Fig. 8. Difference over time between the temperature over the rump and over the planar rump.

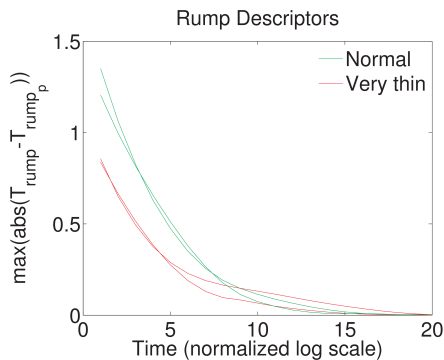


Fig. 9. Maximum difference over time and over the path marked in Fig. 8.

initial time instants, where only the regions close to the source have a significant impact on the temperature.

Using a dataset of 32 animals, we showed that HBRD provides a good representation for the problem, as all the very thin animals in the dataset were clustered together.

By the introduction of relevant descriptors, the work here presented is an important step towards the automation of BCS assessment in dairy goats. Future work should then focus on the automatic identification of the hip and pin bones

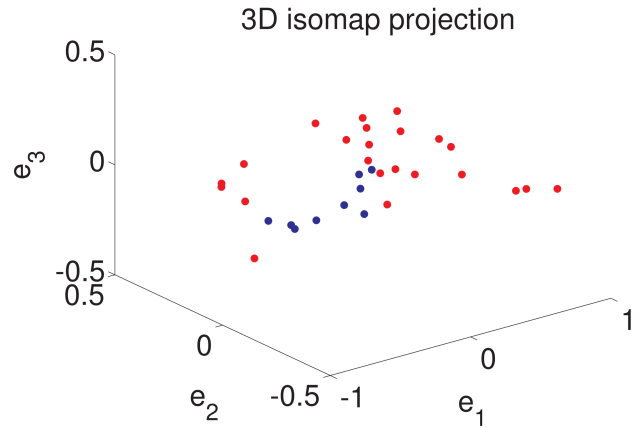


Fig. 10. 3D Isomap projection of the rump descriptors on a dataset of 32 animals. The blue points correspond to thin animals, while red correspond to normal and very fat.

in the RGB images.

ACKNOWLEDGMENT

The authors would like to thank Telmo Nunes, Inês Ajuda and George Stilwell, from the School of Veterinary Medicine, University of Lisbon for valuable comments and for making possible the data collection for this paper.

REFERENCES

- [1] Invited review: Body condition score and its association with dairy cow productivity, health, and welfare. *J. Dairy Sci.*, 2009.
- [2] H. Blokhuis, M. Miele, I. Veissier, and B. Jones. *Improving farm animal welfare - Science and society working together: the Welfare Quality approach*. 2013.
- [3] S. Brandão, J. Costeira, and M. Veloso. Partial view heat kernel descriptor. In *ICRA*, 2014.
- [4] S. Brandão, M. Veloso, and J. P. Costeira. Multiple hypothesis for object class disambiguation from multiple observations. In *3DV*, 2014.
- [5] S. Brandão, M. Veloso, and J. P. Costeira. Global localization by soft object recognition from 3d partial views. In *Iros*, 2015.
- [6] M. M. Bronstein and I. Kokkinos. Scale-invariant heat kernel signatures for non-rigid shape recognition. In *CVPR*, 2010.
- [7] E. W. Dijkstra. A note on two problems in connexion with graphs. *Numerische Mathematik*, 1959.
- [8] J. Hervieu and P. Morand-Fehr. Comment noter l'état corporel des chèvres. 1999.
- [9] D. A. Levin, Y. Peres, and E. L. Wilmer. *Markov Chains and Mixing Times*. American Mathematical Society, 2006.
- [10] R. B. Rusu, G. Bradski, R. Thibaux, and J. Hsu. Fast 3D Recognition and Pose Using the Viewpoint Feature Histogram. In *IROS*, October 18-22 2010.
- [11] J. Shlens. A tutorial on principal component analysis. In *Systems Neurobiology Laboratory, Salk Institute for Biological Studies*, 2005.
- [12] X. Song, J. Schutte, P. van der Tol, F. van Halsema, and P. Groot Kerkamp. Body measurements of dairy calf using a 3-d camera in an automatic feeding system. In *International Conference of Agricultural Engineering*, 2014.
- [13] J. Sun, M. Ovsjanikov, and L. Guibas. A concise and provably informative multi-scale signature based on heat diffusion. In *SGP*, 2009.
- [14] J. Tenenbaum, V. de Silva, and J. Langford. A global geometric framework for nonlinear dimensionality reduction. *Science*, 2000.
- [15] A. Vieira, S. B. ao, A. Monteiro, I. Ajuda, and G. Stilwell. Development and validation of a visual body condition scoring system for dairy goats with picture-based training. *J. of Dairy Sci.*, 2015.
- [16] W. Wohlkinger and M. Vincze. Ensemble of shape functions for 3d object classification. In *ROBIO*, 2011.

Three-Dimensional Reconstruction of Plant Shoots from Multiple Images using an Active Vision System

Jonathon A. Gibbs, Michael Pound, Darren M. Wells, Erik Murchie, Andrew French, Tony Pridmore

Abstract – The reconstruction of 3D models of plant shoots is a challenging problem central to the emerging discipline of plant phenomics – the quantitative measurement of plant structure and function. Current approaches are, however, often limited by the use of static cameras. We propose an automated active phenotyping cell to reconstruct plant shoots from multiple images using a turntable capable of rotating 360 degrees and camera mounted robot arm. To overcome the problem of static camera positions we develop an algorithm capable of analysing the environment and determining viewpoints from which to capture initial images suitable for use by a structure from motion technique.

I. BACKGROUND AND MOTIVATION

The global population is expected to reach 9 billion by 2050 and the spread of prosperity throughout the world is increasing the food intake per capita, driving the demand for a richer, more varied diet. At the same time, changes in climate are causing more frequent and severe flooding, destroying crop yields and shortage of arable land constitutes an additional challenge. It has been widely predicted that without crop climate adaption the production of food will deteriorate [1], [2]. The long-term goal of this work is to provide the innovative approach to sustainable agriculture necessary to adapt to the fluctuating environment and increased demand for food.

The identification of more productive and/or resilient crop species requires connections to be made between the genetic and physical structures of the plant. While significant progress has been made in the study of the genome in recent years, the creation and quantitative analysis of plant phenotypes (structures) has become a major bottleneck. Though some plant traits (e.g. leaf area) can be estimated using a single carefully placed camera and 2D image analysis methods, the ability to produce accurate 3D models of plants would support a wide variety of phenotyping tasks.

Image-based reconstruction methods are attractive in this context. Plants are easily disturbed; non-invasive sensing techniques capable of capturing information across the whole object are required. Plant shoots are, however, a challenging target for image-based reconstruction. Individual variation within species is often large, making it difficult to predict structures a priori. Individual leaves can be very similar in appearance, and densely-packed, occluding each other from many viewpoints: plants can be very crowded scenes. The leaves of many species are quite highly reflective, and often lack the strong texture needed by some techniques.

The starting point for the work described here is the hypothesis that active vision can aid in the generation of high-quality plant models by providing improved, and responsive, image acquisition strategies. Active vision

systems automatically control and manipulate camera viewpoints to provide images which best support the task at hand. Active methods have played a role in other plant-related tasks. For example, [3] attach a camera to a robot arm in order to identify peppers to be collected. The effect of camera placement on fruit picking has been investigated [4], and active vision used to address the problem of occlusion. The large-scale phenotyping systems now finding application in plant and crop science, however, typically rely on fixed viewpoints that are not adapted to the specific plant being modelled. Some systems rotate the plant during imaging, but still use static camera positions. This means that, in many cases, the images captured are far from optimal, adversely affecting the results obtained. The ability to adjust sensors in response to emerging plant properties (e.g. size) is vital if accurate representations are to be obtained of a wide variety of plant species, ages and conditions.

We aim to produce a fully automated, active system that is capable of manipulating a camera's viewpoint to produce high quality 3D models of a wide range of plants by adapting to the visual information available, without user interaction, with the longer-term goal of improved plant phenotyping. The approach proposed here offers more flexibility than existing large scale phenotyping systems by adapting to the natural variation of individual plants in order to obtain optimal data.

The remainder of the paper is organized as follows; we first introduce the reader to 3D plant reconstruction, discussing current approaches and the challenges they face. We then provide a concise overview of active vision and the various components that are necessary, before discussing the approach used in this work. Results obtained from real and artificial plants are presented. Finally, we conclude with a summary of progress and plans for future work.

II. 3D PLANT RECONSTRUCTION

Until the late 1960s botanical drawings were the primary means of capturing plant architecture. Today a variety of approaches are available. Rule-based methods use a set of rules to define the structure of a particular species or class of plant. Varying the parameters of these systems produces models of single plants, but rule-based approaches cannot easily be used to produce the descriptions of specific, existing plants needed to support phenotyping.

Image based approaches seek plant geometry directly, analysing a set of images to reconstruct representations of actual plants. Image based models can be used to support simulations and enable the extraction of trait measurements.

Some approaches, such as Light Detection and Ranging (LiDAR) [5], custom illuminate the target object by emitting

radiation into the scene. LIDAR is commonly used in the airborne reconstruction of field based plants, trees in particular. For example, [6] describe the forest canopy as a series of cones fitted to a raw LiDAR point cloud, then apply simple geometric operations to adjust and correct its height. Similar methods can be applied to smaller plants; [7] model rice plants using a three-dimensional sonic digitiser to capture a 3D point cloud. The digitisation process is reported to take up to an hour to complete, and [8] note that the digitisation process for their approach to reconstruct White Clover canopies required between 3 to 7 hours. They used electromagnetic digitising apparatus with corner flags to aid calibration, applying a destructive approach and pruning the canopy from the top downwards.

The recovery of 3D descriptions from images captured under natural illumination is a longstanding research topic in the computer vision community. A range of approaches such as structure from motion, shape-from-silhouette and space carving, have been developed and can be used for plant reconstruction. For example [9] combine a volumetric opacity estimate with view-dependent texturing and successfully model trees from a series of images whilst [10] use a space carving approach with particle flows to estimate tree volume. [13] use a stereovision approach to reconstruct plant models using automated segmentation. User input is, however, often required. [11] adopt the less common approach of sketching to create plant models. Other interactive approaches construct models directly from images. [12] obtain a point cloud from 35 images of a plant, though user input is required in the form of segmentation to separate leaves, and the image acquisition process is manual.

Fully automatic reconstruction of plants from natural images is challenging due to the intricate phyllotaxis (leaf structure) and continuous reorganization of plant foliage. Many problems arise during the image acquisition and reconstruction processes. Determining the number of images required, and their viewpoints, such that all the required plant features are visible remains difficult. Too few or poorly chosen images results in the loss of data, whilst too many results in increased computational requirements.

Occlusions are a common side effect of complex structures such as plants and can be overcome by capturing an increased number of images, though in some cases approximation techniques must be used. Some approaches rely on intrusive/destructive approaches to obtain more information, however this means the plant cannot return to its original configuration, preventing the comparison of descriptions obtained at different times. Invasive methods can also increase reconstruction time and encourage irreversible errors. Multiple side image methods also exist but often don't support 3D modelling as there is no overlap between images.

An active vision approach can alleviate the problems associated with plant modelling. By manipulating the camera(s) to optimise image number and viewpoint it can help overcome occlusion. By analysing a developing point cloud and moving to view a region that has been identified as unexpectedly sparse, it can help to obtain missing data. Selecting camera positions on the basis of emerging data can

also prevent multiple, unnecessary views of the same regions being collected, both reducing the computational requirements and explicitly reacting to natural variation.

III. AN ACTIVE PHENOTYPING CELL

A. Hardware and Calibration

We present a nonintrusive and nondestructive active vision approach to 3D plant modelling using a camera mounted robot arm and a turntable. The approach is based on a structure from motion method that derives 3D descriptions of the plant surface from sets of colour images. Our active phenotyping cell comprises a Universal Robot 5 (UR5), with a standard handheld camera, Canon 650D, and a high precision turntable, the LT360 EX. The UR5 offers 6 degrees of freedom whilst the turntable enables a full 360 degrees of rotation ensuring it is possible to see the entire plant, both of which are necessary as it is not always possible for the robot arm to move around the entire plant, for example a large rice plant. Our setup is illustrated in Figure 1.



FIGURE 1. HARDWARE SETUP OF ROBOT, TURNTABLE AND CAMERA

We calibrate the camera using a checkerboard approach [14], in which 15 arbitrary images of the checkerboard are captured. We calculate the forward kinematics using Denavit Hartenberg (DH) parameters [15] with joint angles obtained directly from the robot. The remaining transformations are calculated using a simultaneous closed-form quaternion approach [16].

In order to use the turntable with our fully calibrated system we need to take into consideration the rotations performed by the turntable. To achieve this we project to the centre of the turntable, which is known from our calibration process. From this we can calculate Y_j where Y_r , the rotation of Y , is calculated using Eq. 1, j is the number of degrees that the turntable has rotated and function RotZ is a rotation around the Z axis.

$$YR_j = \left(Y' \text{RotZ}(j) \right) \quad (\text{Eq. 1})$$

The translation, Yt , requires that the difference between the rotation matrix before and after a rotation is known; Eq.

2, where \vec{c} is the homogeneous position of the centre of the turntable. Finally, we multiply x' and y' by Yr with its original translation from Y_0 to obtain Y_j

$$\begin{aligned}\vec{p} &= \vec{c} - (\text{RotZ}(j)\vec{c}) \\ x' &= -\vec{c}_x + (-\vec{p}_x) \\ y' &= -\vec{c}_y + (\vec{p}_y) \\ \vec{Yt}_j &= [x' y' 0 1]'\end{aligned}\quad (\text{Eq. 2})$$

Y_j can then be calculated as

$$Y_j = [YR_j \vec{Yt}_0] * \vec{Yt}_j \quad (\text{Eq. 3})$$

Once we have a fully calibrated system we are able to remove the checkerboard from the scene and calculate our camera position from the remaining variables.

B. Image acquisition strategies

To obtain accurate 3D models via structure from motion the camera needs to be in a position to collect an optimal number of images of the highest quality. This is a challenging problem due to the vast number of possible viewpoints and the lack of prior knowledge of the shape and size of the object. We have developed a proof-of-concept image acquisition strategy that uses a simple threshold-based method to identify the plant in order to calculate initial camera positions. There are two primary constraints; 1. The camera must be facing the plant in the robot's starting position, approximately placing the plant in the centre of the view. 2. A white background must be used with no other colour visible, which allows us to calculate the position of any given plant. These constraints are commonly satisfied and/or are easily achievable in controlled phenotyping environments. More powerful segmentation methods could be used in less constrained environments.

The role of image analysis in the proposed system is to identify four points on the boundary of the plant region; those nearest the four edges of the image. The coordinates of these points provide measures, TX, BX, LX, RX, of the shortest distances from the plant region to top, bottom left and right edges respectively. A user-defined threshold is applied to separate plant from (white) background, and plant pixels with the highest and lowest x and y coordinates are identified. To reduce the likelihood of selecting a noise-generated false-positive plant pixel we examine 400 pixels around each candidate (approximately 0.01% of the total pixels). Only if 75% or more are of those pixels are above threshold is the pixel accepted as lying on and near the boundary of the plant (Figure 2). This heuristic is simple, but effective and computationally efficient.

To initialise and parameterise the system the camera is first moved to a start position facing the turntable. It is then moved in a plane normal to the image plane to define four

points. These points define the corners of a quadrilateral normal to the image and passing through the start position. The points are chosen to be the furthest from the start point in each direction from which the turntable remains visible. Throughout image acquisition all translational movements of the camera take place within the plane defined by this quadrilateral. Camera rotations may take it outside the plane, but it remains close to it at all times.

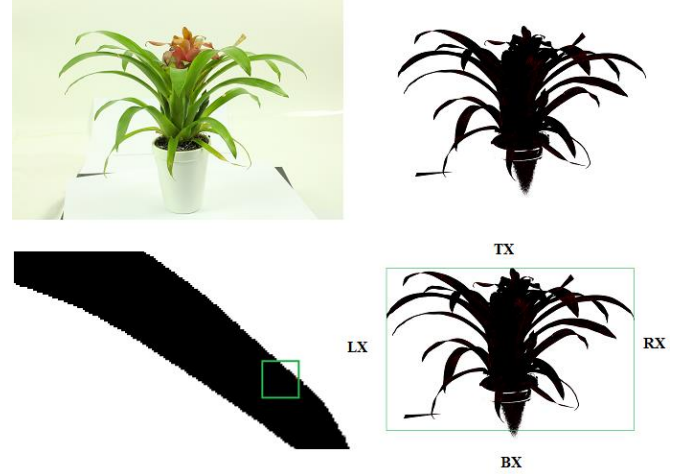


FIGURE 2. TOP LEFT: ORIGINAL IMAGE, TOP RIGHT: IMAGE SEPARATED FROM BACKGROUND WITH DISCARDED OUTLIERS, BOTTOM LEFT: EVALUATION OF A PIXEL, BOTTOM RIGHT: THE RESULTING BORDER DEFINING VALUES RX, LX, TX, BX

The centre of the quadrilateral is used to define a set of n initial points from which the search for suitable viewpoints begins. These are evenly spaced along a vertical line through the quadrilateral centre; the image acquisition process is run from these points in fixed (lowest to highest) order, providing n images for each turntable position. The dimensions of the quadrilateral determine the size of the camera translations made during image acquisition. Large translations towards (forward) or away from the plant (backwards) are 30% of the width of the quadrilateral, small movements 10%. Camera rotations (up, down, left, right) are of a small, fixed size (typically 2 deg.) set by the user.

Active image acquisition begins with the camera in one of the initial positions described above. Images are repeatedly captured, thresholded, plant boundary points identified, and the camera moved under the control of a set of heuristic rules until the plant is either fully enclosed by the image boundary but without excess space or the arm is at its maximum reach.

The rules employed are intuitive, but effective:

- If there are 50 or more pixels of white space surrounding the plant (TX, LX, BX, RX all > 50) a forward movement is made.
- If the plant region is close to the boundary at either the top and bottom or left and right a backward movement is made.
- Forward and backwards movements are large unless a movement in the opposite direction has just been made, in which case they are small. This introduces a degree of fine-tuning and prevents oscillation.

- If LX is large and RX is small, rotate left.
- If RX is large and LX is large, rotate right.
- If TX is large and BX is small, rotate upwards.
- If TB is large and TX is small, rotate downwards.

These rules are applied to each of the vertical stack of initial points. Once an improved camera position has been identified for each such point, images are captured and the turntable is rotated. The size of the rotation is set to ensure that at least 60 images are captured in total. In a typical experiment 6 vertical positions are used, and the turntable rotated 36 degrees, between capture sessions. During image capture camera files are created containing the camera matrix that transforms a 3D point to a 2D point on the image plane.

Plant structure varies significantly between species; when modelling those expected to be rotationally symmetric the search for camera locations need only be performed once and the same positions used at each turntable rotation. Given species that may not be rotationally symmetric a new search may be performed for each turntable setting.

C. Reconstruction methods

A point cloud is first generated from the images and corresponding transformation matrices using Patch-based Multi-view Stereo [17]. The point cloud is the starting point for further reconstruction and is a common input for many software packages and surface reconstruction algorithms.

We also apply Pound et al's Canopy Reconstruction method [18] which accepts a point cloud as input and generates a surface using alpha-shapes and level set methods, aiding the process by revisiting the images to ensure consistency. Note that this final stage is not possible when using a direct 3D sensor such as a laser scanner.

Surface reconstruction is fully automated and only requires user interaction if the hardware is moved, in which case the calibration stage needs to be performed. Patch-Based Multi-View Stereo (PMVS) and Canopy Reconstruction have been integrated into our cell to create a smooth workflow that can run unattended, taking a step towards reducing the phenotyping bottleneck. PMVS takes a set of images and camera parameters and reconstructs the 3D structure and Canopy Reconstruction takes the output to generate a surface-based description.

IV. RESULTS AND DISCUSSION

We conducted experiments on four artificial plants of varying sizes and densities (Figure 3). Models of each plant were built using a set of fixed camera positions, defined such that the largest of our plants is fully visible in each image, and results compared to those obtained from our active vision system, which reacts to the size of the plant. A set of 60 images were used for each reconstruction.

This initial study focuses first on the point cloud data provided by PMVS. Comparison of the number of high quality points generated from static and actively captured images by this state of the art method gives some insight into the potential benefits of the active approach. Figure 4 shows the point clouds obtained from each image set, for clarity we

have manually removed, using Meshlab, the excess data obtained from under the plant, mainly from the plant pot.



FIGURE 3. ORIGINAL PLANTS, TOP ROW PLANTS A AND B, SECOND ROW PLANTS C AND D

We compare the number of points obtained by static and active vision for each plant; Plant A active 120,422 whereas static produces significantly less at 35,872. Plant C active has 99,570 points compared to 26,668 static and Plant D active 51,267 points and 17,388 static. The static camera positions were in fact obtained by running the active method over plant B, ensuring that the largest plant is fully visible in the images and therefore has the same number of points for both static and active; 168,344. Active vision provides significantly more valuable points for each plant, which is particularly useful for the small dense plants in this study.

Though point clouds capture the broad structure of the target object, surface reconstruction is essential for plant phenotyping, as many desirable traits must be measured over leaves. The canopy reconstruction method of [18] was applied to the actively acquired image sets generated here; results are shown in Figure 5. Our artificial test plants are particularly challenging, with only very small 3D and colour differences between their very close packed, uniform leaves. [18] employs an image-based surface patch extension method which produced an acceptable surface reconstruction, but tended to over-extend leaves. We applied the same techniques to a dense domestic plant (Figure 6). The noise present in the point cloud (middle) has successfully been removed by [18] which uses a colour threshold to remove noisy points. The point clouds and images obtained from our initial active phenotyping cell can support fully automatic 3D modelling of real plants.

More complex reconstruction algorithms such as [18] may also benefit from the integration of active image acquisition strategies, but have different requirements than point cloud recovery methods. Though [18] builds on data supplied by PMVS, choosing images to simply increase the number of points may not be the best strategy. [18] operates within planar patches fitted to point clusters – increasing the number of points available need not improve the plane descriptions, and could add noise. The points provided by PMVS arise from textured leaf areas; [18] may benefit more from strategies that provide clearer views and higher resolution

images of smoother (less textured) areas, allowing a greater degree of patch extension while making leaf boundaries more easily identifiable. This could be achieved by exploiting initial surface reconstruction data to guide acquisition of new images, rather than selecting them from a pre-acquired set as is currently the approach in [18].



FIGURE 4. LEFT HAND SIDE ACTIVE VISION POINT CLOUDS, RIGHT SIDE STATIC. THE PLANTS FROM TOP TO BOTTOM ARE A, B, C, D

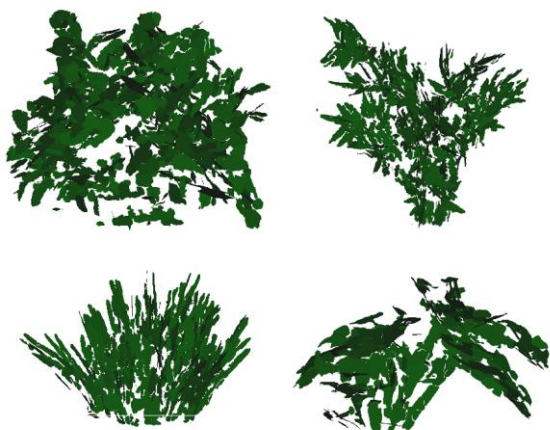


FIGURE 5. SURFACE RECONSTRUCTION FOR THE FOUR ARTIFICIAL PLANTS CORRESPONDING TO THOSE SHOWN IN FIGURE 3

Point cloud data may also be used to guide image acquisition. Though point clouds provide a relatively crude representation of complex plant architectures, they can capture plants' broad structure. Models of the expected distribution of points in different species might highlight regions of the target volume that are not sufficiently explored

by an initial image set, allowing the camera to viewpoints that will produce more complete plant descriptions.



FIGURE 6. SURFACE RECONSTRUCTION OF A REAL PLANT FROM ACTIVELY ACQUIRED IMAGES. TOP; ACTUAL PLANT, MIDDLE; THE POINT CLOUD ACQUIRED, BOTTOM; SURFACE RECONSTRUCTION

V. CONCLUSION

We present initial work towards an active plant phenotyping cell capable of recovering 3D descriptions of plant shoots from multiple colour images. An automatic image acquisition technique is described which provides improved point cloud data and supports the 3D reconstruction of leaf surfaces. After the initial calibration of the system, which need only be done if hardware is replaced or moved, no user input is necessary and the process can continuously run through a custom designed interface. Experimental results show that by using an active vision approach, rather than a traditional static set of camera positions we are able to gather significantly more data on the plant and its structure from the same number of images.

The active vision approach provides significant opportunities to enhance and extend the scope of surface reconstruction methods such as [18]. Careful selection of views focusing on areas of ambiguity will, we believe, produce both more accurate point clouds and higher quality image data from which surfaces can be produced. Active

vision may also reduce the number of unnecessary images captured, those adding little to the reconstruction, improving throughput.

Cameras and multi-view stereo are employed here, rather than e.g. laser scanners, as the image sets involved carry information on plant appearance missing from a point cloud. In addition to providing 3D structure, multiple colour images could be used e.g. to assess plant health. We would suggest, however, that an active sensing approach could aid the integration of the 2½D data produced by such devices.

Future work will more closely integrate active image acquisition into the reconstruction process, allowing a wide range of camera movements and focusing on areas of ambiguity, occlusion and those likely to be missing data. Evaluation of the models produced is difficult as ground truth data is required. Future work will also investigate the possibility of using X-ray CT data to produce reference data. In the longer term we aim to provide improved, active phenotyping of a wide range of complex plant species.

REFERENCES

- [1] A. Challinor, J. Watson, D. Lobell, S. Howden, D. Smith, and N. Chhetri, “A meta-analysis of crop yield under climate change and adaptation,” *Nature Climate Change*. Nature Publishing Group, 16-Mar-2014.
- [2] A. Adeloje, “Global Warming Impact: Flood Events, Wet-Dry Conditions and Changing Scene in World Food Security,” *J. Ag. Res. Dev.*, 9, 1, 2010.
- [3] J. Hemming, C. W. Bac, B. A. J. van Tuijl, R. Barth, J. Bontsema, E. J. Pekkeriet, and E. van Henten, “A robot for harvesting sweet-pepper in greenhouses,” in *Proceedings of the International Conference of Agricultural Engineering*, 2014.
- [4] J. Hemming, J. Ruizendaal, J. W. Hofstee, and E. J. van Henten, “Fruit detectability analysis for different camera positions in sweet-pepper,” *Sensors (Basel)*, vol. 14, no. 4, pp. 6032–44, Jan. 2014.
- [5] C. A. Northend, “Lidar, a laser radar for meteorological studies,” *Naturwissenschaften*, vol. 54, no. 4, pp. 77–80, 1967.
- [6] M. Van Leeuwen, N. C. Coops, and M. A. Wulder, “Canopy surface reconstruction from a LiDAR point cloud using Hough transform,” *Remote Sens. Lett.*, vol. 1, no. 3, pp. 125–132, Sep. 2010.
- [7] T. Watanabe, J. S. Hanan, P. M. Room, T. Hasegawa, H. Nakagawa, and W. Takahashi, “Rice morphogenesis and plant architecture: measurement, specification and the reconstruction of structural development by 3D architectural modelling,” *Ann. Bot.*, vol. 95, no. 7, pp. 1131–43, Jun. 2005.
- [8] M. Rakocevic, “Assessing the Geometric Structure of a White Clover (*Trifolium repens* L.) Canopy using 3-D Digitising,” *Ann. Bot.*, vol. 86, no. 3, pp. 519–526, Sep. 2000.
- [9] A. Reche-Martinez, I. Martin, and G. Drettakis, “Volumetric Reconstruction and Interactive Rendering of Trees from Photographs,” in *ACM Transactions on Graphics (ToG)*, 2004, vol. 23, no. 3, pp. 720 – 727.
- [10] B. Neubert, T. Franken, and O. Deussen, “Approximate image-based tree-modeling using particle flows,” in *ACM SIGGRAPH 2007 papers on - SIGGRAPH '07*, 2007, vol. 26, no. 3, p. 88.
- [11] M. Masry and H. Lipson, “A sketch-based interface for iterative design and analysis of 3D objects,” in *ACM SIGGRAPH 2007 courses on - SIGGRAPH '07*, 2007, p. 31.
- [12] P. Tan, L. Yuan, and J. Wang, “Image-based Plant Modeling Overview of Plant Modeling System,” pp. 599–604, 2003.
- [13] B. Biskup, H. Scharr, U. Schurr, and U. Rascher, “A stereo imaging system for measuring structural parameters of plant canopies,” *Plant. Cell Environ.*, vol. 30, no. 10, pp. 1299–308, Oct. 2007.
- [14] Z. Zhang, “A Flexible New Technique for Camera Calibration,” *IEEE Pattern Anal. Mach. Intell.*, vol. 22, no. 11, pp. 1330 – 1334, 2000.
- [15] J. Denavit, “A kinematic notation for lower-pair mechanisms based on matrices,” *J. Appl. Mech.*, vol. 20, pp. 215–222, 1955.
- [16] F. Dornaika and R. Horaud, “Simultaneous robot-world and hand-eye calibration,” *IEEE Trans. Robot. Autom.*, vol. 14, no. 4, pp. 617–622, 1998.
- [17] Y. Furukawa and J. Ponce, “Accurate, dense, and robust multiview stereopsis,” *IEEE Trans. PAMI.*, vol. 32, no. 8, pp. 1362–76, Aug. 2010.
- [18] M. P. Pound, A. P. French, E. H. Murchie, and T. P. Pridmore, “Automated recovery of three-dimensional models of plant shoots from multiple color images,” *Plant Physiol.*, vol. 166, no. 4, pp. 1688–98, Dec. 2014.

Advanced pasture management through innovative robotic pasture maintenance*

Z. Gobor, C. Cariou, B. Seiferth, S. Thurner, W. Feucker, C. Tessier, B. Tekin, and M. Berducat

Abstract— The results of the i-LEED project should demonstrate an advanced pasture management combining a pasture care and management robot with the i-LEED software in order to provide significantly improved pasture regrowth, biomass quality and consequently better feeding of the grazing cattle. The information from the barn and the pasture complementing one another will lead to a more balanced and demand driven feed supply to the cattle, particularly affecting the improved amount of valuable milk components of the dairy cattle. Besides the positive effects for the pasture and cattle, the required working time for pasture care and management should decrease. Furthermore, less greenhouse gas emissions are expected due to avoiding of open and compacted soil, as well as better nutrient distribution and a higher productivity.

I. INTRODUCTION

Contemporary agricultural production faces new challenges. The world population increases steadily with a trend to surpass the 9 billion mark by 2050. This will affect the demand for meat and dairy products globally and cause higher retail prices in Europe. The higher living standard, rising incomes and urbanisation are often associated with the addition of protein to the diet and increased consumption of higher value meats, such as bovine and dairy products. Not only the quantity but ever more the quality is demanded. In the past 50 years the meat production has increased by 300% whereas the number of bovine, porcine, poultry and ovine animals has grown, at 57%, 137%, 400% and 49%, respectively. By 2050 compared with production levels in 2005/07 the required increase of the meat production is estimated to 200Mt a year [1], which is a reason why the meat is anticipated to be one of the fastest growing commodities in the coming years. The consumption of dairy

*The project: “Advanced cattle feeding on pasture through innovative pasture management (i-LEED) is funded within the 2nd ICT-AGRI ERA-NET and financially supported by a grant from NCPs: the German Federal Ministry of Food, Agriculture and Consumer Protection (BMELV) through the Federal Office for Agriculture and Food (BLE) grant number 2812ERA058 and 2812ERA059, the French National Research Agency (ANR) grant number 12-ICTA-0002-01 and 12-ICTA-0002-02 and the Scientific and Technological Research Council of Turkey (TUBITAK) grant number 112 O 464.

Z. Gobor, B. Seiferth, S. Thurner are with the Bavarian State Research Center for Agriculture (LfL), Institute for Agricultural Engineering and Animal Husbandry, Vöttinger Str. 36, 85354 Freising, Germany (phone: +49 816171 3897; fax: +49 816171 4363; e-mail: Zoltan.Gobor@LfL.bayern.de).

C. Cariou and M. Berducat are with the National Research Institute of Science and Technology for Environment and Agriculture (IRSTEA), 9 avenue des Landais, CS 20085, 63172 Aubière Cedex, France (e-mail: Christophe.Cariou@irstea.fr).

W. Feucker is with the German computer retailer Data Service Paretz GmbH (DSP), Parkring 3, 14669 Ketzin, Germany (e-mail: Werner.Feucker@dsp-agrosoft.de).

C. Tessier is with the French software company Effidence, Chemin de Saint-Verny, 63450 Saint-Saturin, France (e-mail: Cedric.Tessier@effidence.com).

B. Tekin is with the Ege University, Faculty of Agriculture, 35100 Bornova-Ýzmir, Turkey (e-mail: Behic.Tekin@ege.edu.tr).

products in the coming years until 2020 is expected to increase modestly in developed countries. Milk and dairy products are anticipated to be one of the fastest growing sectors in the coming years, increasing demands on agricultural resources. In the context of the reformed Common Agricultural Policy (CAP) the animal products from EU should become more competitive on the world market and ensure a fair standard of living for farmers [2].

The required additional production needs to be provided by increased productivity and the real and essential challenge lies in meeting the rising demands in a more sustainable manner. The productivity gains will depend on protecting the available resources, R&D, and on the ability of the industrial sector to adopt the latest technologies.

A possible solution to stay sustainably competitive is based on continuous grazing farms, which can be considered as low-input farming systems (LIFS). Mostly in disadvantaged areas of some EU countries, a stronger tendency of LIFS was noticeable in the previous period aiming at aspects of sustainability [3]. In such systems high pasture graze portions (35-60%) of the total annual feeding ration are preferred. Hence the management of the pasture has a high relevance, because under optimal conditions with constant grazing the grass growth remains very young and shows high energy values (9,8-11,3MJ ME). In some cases a complete dispense on concentrate during the grazing period can cause a decrease in fat- and protein percentage as well as an increase of urea content in milk. For this reason a continuous monitoring of the pasture and milk parameters needs to be striven for, in order to provide better quality of the products as well as animal health and welfare. One of LIFS disadvantages is a significant amount of work required in order to stay manageable.

On the contrary to conventional high-input farming system HIFS, LIFS provokes less negative impacts on the environment and the quality of life of rural and neighbouring communities. Fewer changes on the landscape can be observed, decreasing its homogenisation and destruction of traditional landscape elements and, consequently, loss of habitats. Furthermore, the general public likes to see the dairy cows on the pasture, and therefore the dairy industry tries to keep grazing to remain the standard [4].

In the civil society ever more people are worrying about animal welfare conditions and the negative effects of livestock production units on the appreciation of the landscape [4]. Accurate data about feeding, animal health and welfare can be achieved only by using ICT and thus, it is possible to optimise the production and make it more sustainable. In spite of the growing population the demographic trends indicate that the number of the well versed agricultural workers will either remind static or even decrease especially in the developed countries and cause additional expenditures in agricultural production. Considering these facts the implementation of ICT and

robotics also for livestock husbandry on pasture should be striven for in order to make this method more competitive.

Introduction of field robots in the agricultural or off-road sector with relatively high working speed (range up to 3m/s), which have been considered as optimal for carrying out selected operation with the pasture robot, are rarely addressed in the literature. Associated accurate path following and integrity considerations of a robot moving at high speed under harsh conditions (slope, sliding, varying soil conditions, obstacles, rollover risk) poses in fact many challenging problems. The main existing approaches [5, 6] assume currently a known and non-varying environment, such as road conditions or very low speeds, and the robot stability is generally only addressed from a passive point of view, using rollover protective structure, or thanks to mechanical design properties [7]. In off-road conditions (varying soil properties, slope, sliding), large lateral errors are usually observed if a classical control approach is used [8], usually based on the pure rolling without sliding assumption, and the robot stability need to be addressed with respect to the rollover risk. Moreover, the robot must be able to detect and avoid potential obstacles during its motions in the pasture (e.g. machines, animals, humans). Many methods have been proposed in the literature for this function [9] but their performances are often limited to robots moving at very low speeds, neglecting the sliding and skipping effects in the obstacle avoidance reaction in off-road conditions. Making mobile robots safe and reliable is an absolute necessity for them to find their market.

II. OBJECTIVES

The aim of the project is to optimise the feeding of cattle on pasture as well as the management of the pasture through introduction and fusion of innovative tools. The new i-LEED software, which will be developed within the frame of the project, will interact with a global Herd Management Software (HMS) and provide control of the pasture robot as well as providing calculations of the optimal feeding strategy for cattle and maintenance of the pasture providing support for the farm manager by decision making.

Within the project a concept of pasture robot including several variants will be developed based on existing wheeled robotic platforms. The pasture robots will be redesigned in order to allow stable movement under difficult terrain conditions. During the optimisation phase aspects of energy consumption, energy availability and mobility management will be particularly considered. The pasture robot should be able to move under specific circumstances at relatively high speed (up to 3m/s) in the pasture with a high-precision, in order to obtain an economically viable solution. In the same time the accuracy of defined path following should stay stable with a lateral error not higher than 20cm.

Furthermore, different actuators (mulcher and seeder) and adequate sensors for pasture care will be implemented on the robot platform. The sensors should provide information about the biomass to ensure optimised feeding of cattle and allow detection of cowpats and leftovers, heading gramineous plants, undesired plants (nettles, crowfoot etc.) or areas

without vegetation, in order to carry out selective improvement of the pasture condition after grazing. This task have to be done by mulching only the areas with cowpats, leftovers and heading gramineous plants as well as by seeding on areas without vegetation.

III. MATERIALS AND METHODS

The literature survey and analysis considering the basic concept for pasture robot, which will be adapted within the frame of the i-LEED project, indicated that a solution with a caterpillar track can cause considerable damages on the pasture, in particular during the sharp turns and manoeuvres [10]. The wheeled robots in general have lower amortisation and maintenance cost, steering with high-precision is more reliable especially during turns at high speed in presence of sliding, their energy consumption is considerably lower (to speed up the outside track during turns requires considerably more power), and finally, to repair a wheeled system is under certain conditions much easier. The better distribution of total weight, one of the main advantages of a vehicle with tracks, plays a subordinate role because a light weight low-energy consuming solution is pursued in the i-LEED project. Based on these facts, similar decisions made by other authors [11, 12, 13] and ideas to consider further agricultural field tasks (not only on pasture) using the same robot platform, a wheeled platform was chosen.

The stability problem will be approached based on adaptive and predictive control techniques, designed to compensate for the perturbations encountered in a natural environment and perform accurate path following. Certain approaches [14, 15] can lead to an oscillating behaviour of the robot, even at limited speed, but the improved algorithms presented in [16] can handle this problem.

A. Pasture robot

To avoid problems considering conflicts between the pasture robot and cows, all the missions will be carried out on the paddocks not occupied by animals. The robot will access the paddocks from the opposite site than the cows, because cows need to return to the automatic milking systems (AMS) two to three times per day along the passageway and in case the robot would use the same passageway unnecessary robot-cow encounters, with unknown implications, could not be avoided. In the advanced phase of the project the cohabitation of cows and robot in the same paddock could be also an interesting constellation which needs to be considered to experience feedback for future work, before the product introduction on the market.

One version of the pasture robot will be developed using the platform RobuFast [16](IRSTEA) another version will be developed based on a commercial available mobile, remotely controlled mulcher [17] (Lfl) and a third version of the pasture robot will be developed based on the RoboTurk platform [18] (EGE) see Figure 1. The conditions on pasture which can affect the kinematical and dynamical behaviour of the pasture robot were analysed and the requirements defined in order to choose or rather develop the pasture robot.



Figure 1. : Robotic platforms: RobuFast - IRSTEA (top), i-LEED LfL (middle), RoboTurk (bottom left) and rendering of the novel concept of EGE (bottom right)

Considering the functionality which the pasture robot has to fulfill, two main tasks are defined: scouting – data collection about the condition of the pasture, and pasture maintenance – sowing and mulching. Figure 2 illustrates the process of the functionality of the robot for one paddock.

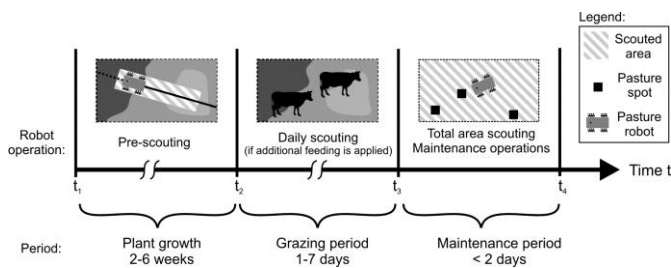


Figure 2. Process of the robot for one paddock

1) Scouting

Scouting operations take place during the period of growth before grazing, optionally during the grazing period (if additional feeding after a grazing day is applied) and immediately after grazing. The aim of scouting is to collect information about forage quality and biomass quantity, as

well as to locate suboptimal zones on a pasture in order to provide the necessary information for controlling the agricultural implements mounted to the pasture robot and thus gain optimal maintenance of the pasture.

Commercially available sensors for these tasks will be evaluated, tested and integrated in the pasture robot, if applicable. E.g. an approach for determining the biomass quantity using a 2D laser scanner (wavelength 660 nm) was carried out. For this purpose the sensor was attached to a framework for scanning a defined area of grass, whereas the scanning plane was perpendicular to the direction of motion and the sensor traversed over the area with constant speed. After scanning the grass was cut, collected, the samples were weighted and later dried (method of the Association of German Agricultural Analytic and Research Institutes - VDLUFA) to determine the dry mass as reference. Moreover a NIR sensor (wavelength range of 950-1650 nm) is tested in regard to the identification of dry matter content and feed substances (e.g. nitrogen) of the grass on pasture.

In order to localise the spots on the pasture on which maintenance operations are desired test with the 2D-laser scanner were carried out, too. With the regard to the detection of faults in the sward, so-called seeding spots, output dimensionless echo amplitude values depending on the surface properties of the target object are used. In principle amplitude data can deliver an estimate of the relative reflectivity of an object [19]. With the first test series under model conditions the difference between the reflectance of the areas covered with grass and soil was proven. The laser scanner was installed stationary above a cut dry lawn area ($z = 740$ mm), so that the scanning plane was perpendicular to the ground level. The scanning zone was split into two areas: the first was covered with 30 mm high cut lawn (see Figure 3 on the right) and in the second trays filled with local dry topsoil were placed onto the grass (see Figure 3 on the right). The trays simulated faults in the sward, e.g. caused by trampling of the cattle or other animals. In this test series the both zones have approximately the same height. The trays were total covered to assure a laser beam reflection on the soil. A width of 1200 mm was scanned, which corresponds to the working and scanning width of the pasture robot.

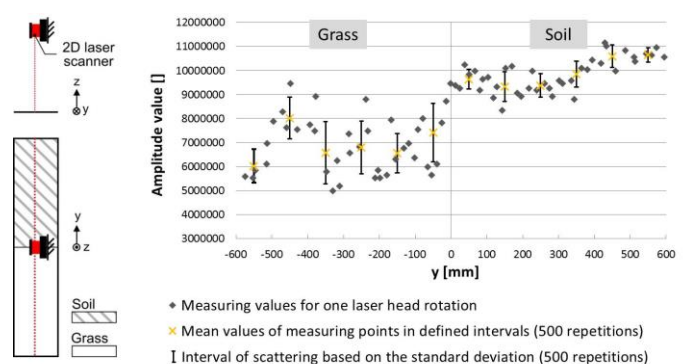


Figure 3. Experimental arrangement (left); amplitude values collected with Pepperl&Fuchs R2000 laser scanner for one laser head rotation in relation to the y-coordinate and mean values in defined intervals for 500 repetitions

2) *Mulching and seeding*

The maintenance operations: mulching and seeding take place after grazing. Because of the plant growth and the impending weed infestation, the maintenance operations, especially mulching, have to be finished within two days after animals have left the pasture. The maintenance operations include mulching of leftovers and heading gramineous plants, seeding of faults areas without vegetation and spreading cowpats.

B. *i-LEED Software*

The i-LEED pasture management software (PMS) should allow planning and managing the entire grazing activities in combination with one or more pasture robots. For this purpose it combines data from the mission planning software, the attached sensors, the herd management system and the feed ration software. The aim of the software is to support the farmer by decision making in order to increase the efficiency of the pasture utilisation while reducing the risk for the animals' health and negative environmental impacts due to grazing activities. The PMS is supposed to be a comprehensive repository of all relevant information about grazing activities. Moreover it allows scheduling of the grazing rotation and supports the operation of the pasture robots.

1) *Mission planning*

In addition to scheduling the operations to be performed by the pasture robot in the different paddocks, one of the main issues of the mission planner is to generate the trajectories to be followed by the robot with respect to the needs of the mission (e.g. full or partial coverage of a paddock, reach successive areas, speed reference), while taking into account and adapting to both the constraints of the environment (e.g. shape of the paddocks, static obstacles, fences) and kinematic and dynamic constraints of the considered robot (e.g. wheelbase, maximum wheels steering angle and rate).

Based on a prior knowledge of the environment, fences location and identification of several kinematic and dynamic parameters of the robot, the proposed planning approach is based on the junction of elementary primitives (arc of circles, line segments) with arc of clothoids to generate continuous curvature trajectories feasible for the pasture robot [20].

2) *Robot control*

The control algorithm of the robot must perform three main functions, namely the accurate path following of previously planned trajectories, the management of obstacles, and the conservation of the robot stability.

To accurately guide the pasture robot along the previously planned trajectories at the speed requested by the mission, the control algorithm needs to continuously adapt the parameters considering the encountered off-road environment, in particular the soil conditions that may lead to important sliding phenomena.

Compared to indoor rigid and asphalted ground, the displacement with wheels on agricultural grounds, by nature (structure, compaction, humidity etc.) and varied topology (slope), can lead to uncertain kinematic and dynamic

behaviours of a mobile robot, in particular when the speed of displacement is relatively high. In such conditions, the pure rolling without sliding assumption (widely used in mobile robotics because it significantly simplifies the modelling of vehicle based on conventional wheels), cannot be directly exploited without obtaining low guidance performances. In order to adapt the control algorithm accordingly, the understanding of the interaction of the robot with the ground is essential. However, describing the physical phenomena during the interaction of the wheels of the vehicle with the ground is particularly complex, all the more on natural grounds. The models of such interactions are generally dedicated to the automobile industry (e.g. analytic approach based on the detailed description of the physical phenomena inside the tire, or empirical approaches from experimentations performing on test bench), and thus difficult to simply adapt for a vehicle rolling on a natural ground. Nonetheless, without aiming to come back to the forces occurring at the wheel level, the sliding phenomena at the interface of the wheel with the ground can be represented through the sideslip angle representing the difference between the theoretical direction of the linear velocity vector at the wheel centre (described by the wheel plane) and its actual direction. Assuming that this angle robustly represent the sliding influence on vehicle dynamics, the approach can be used to indirectly estimate the sideslip angles of the wheels of the robot within of a suited observation algorithm.

Although the trajectory planner generates obstacle-free trajectories, the robot must have capabilities to detect obstacles and avoid them (or immediately stop if not possible). Considering an example of an isolated obstacle inside one paddock, a simple approach can be defined to change the reference of the lateral deviation with respect to the current trajectory, taking the advantage of the capabilities of the previously developed controllers [16]. Another approach could be to redefine the trajectory to new feasible one which avoids the obstacle. This approach will be necessary to choose in case when the robot counteracts to several obstacles simultaneously and finding a feasible obstacle-free path between several obstacles in real-time is required.

IV. RESULTS

A. *Development of the pasture robot*

1) *Specification*

After an analysis of the surface and terrain conditions on pasture by detection of the soil profile vehicle parameter like ground clearance, track gauge, wheel base and axle articulation were defined (see Table 1).

TABLE I. REQUIREMENTS FOR THE ROBOT PLATFORM

Parameter	Value (up to)
Climbing ability [°]	35
Possible cross slope [°]	35
Min. axle articulation [mm]	150
Min. ground clearance [mm]	150
Wading depth [mm]	150

2) Scouting

Tests on cultivated grassland have shown that the estimation of the biomass quantity based on the grass height using a 2D-laser scanning technology (wavelength of 660nm) is possible. Figure 4 shows the result of measurements on cultivated grassland within one season (3 repetitions per sample area of 1 m²):

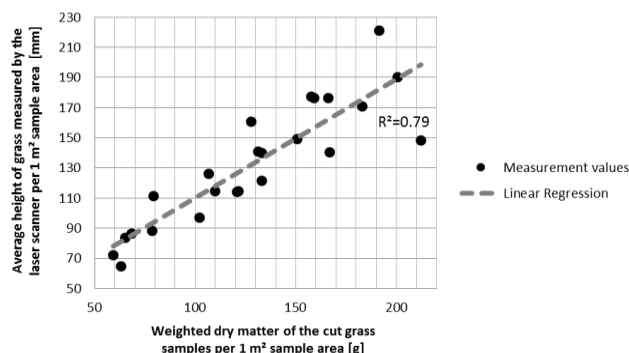


Figure 4. Relationship between measured grass height using the laserscanner and the actually measured dry matter

A linear regression resulted in a correlation coefficient R^2 of 0.79. Similar measurements are running on pasture areas to develop an algorithm for determining biomass on the basis of grass height data.

In regard to the detection of seeding spots for example, measurements under model conditions have shown that the 2D laser scanner R2000 (Pepperl&Fuchs) is able to distinguish between grass and soil spots under the described conditions via the in section III mentioned dimensionless echo amplitude value. The results are illustrated in diagram on Figure 3, showing inter alia amplitude values for one laser head rotation (resolution 1°) in relation to the y-position of the measured surface, calculated using the distance values of the laser for each measuring point.

The different scattering around a particular mean value (see Figure 3) of the measuring points for the two zones is clearly visible. The scattering of the amplitude values in the grass zone is much higher in comparison to the values of the soil zone. It is apparent that only one amplitude value cannot be used to state something about the surface zone. To determine the type of zone several neighbouring measuring values must be considered, especially their mean value and scattering. In the diagram calculated mean values in defined intervals ($y_{n1} < y < y_{n2}$) with an interval length of $\Delta y = 100$ mm were calculated for 500 repetitions. For the robot operation on pasture a resolution of $\Delta y = 100$ mm is necessary to detect sward faults in the size of a cattle footstep. Because of the circular movement of the laser beam the distances between neighbored points in y direction on the flat reference level ($z = 0$) increase with $|y|$. Consequently with increasing $|y|$ the intervals contain a lower number of measuring values. The depicted coefficients of variation of the amplitude values for the grass zone ($-600 < y < 0$ mm) are in the range from $\pm 10.8\%$ to $\pm 19.8\%$. The values for the soil zone ($0 < y < 600$ mm) vary in a smaller range between $\pm 2.8\%$ and $\pm 6.6\%$. The relative high mean value for area $y =$

$[-500 \text{ to } -400]$ mm () confirms the necessity to observe the scattering of measured values to identify the surface type.

The method for detection of seeding spots can be used under certain circumstances, (the definition of the amplitude as parameter needs to be considered [19]) for detection of suboptimal zones on pasture, like faults in the sward. Especially the scattering and the average values of echo amplitude data can be characteristic parameters of soil or rather grass zones. Further tests, considering different environmental and physical conditions (illumination, moisture of soil, sensor position etc.) and combination with additional sensors as well as measurements in motion are necessary to develop an algorithm, which can deliver enough information to identify zones on pasture.

3) Mulching and seeding

One of the most important criteria by using a mulcher implemented on an autonomous robot is safety. Objects appearing on the pasture such as stones etc. should not be thrown uncontrolled by the moving tools of the mulcher. If there is an animal or even a person near of the operating area, the mulcher has to stop immediately. Another very important point for the operation of the pasture robot is reliability. Objects appearing on the pasture such as stones etc., should not restrict the functionality or damage the machine. Under difficult conditions, e.g. lying vegetation, the machine should not be blocked with organic material, which under certain circumstances can lead to loss of functionality. Furthermore, due to the power autonomy and operational costs the energy consumption of the mulcher should be as low as possible. On pasture the surface can be quite rough and hilly. For this reason the mulcher must have appropriate height guidance and has to be designed quite short to avoid damaging the grass sward. The shorter the better is the ground adjustment of the tools of the mulcher. Large quantities of grass should be chopped as fine as possible spread evenly. Accumulation and clumping of chopped plants biomass have to be avoided, especially under wet conditions. Considering the energy consumption and the problems related to soil compaction, low weight of the mulcher is preferable. An evaluation of the mulcher types based on the above mentioned requirement criteria, resulted with a conclusion that the flail mulcher would be the most suitable one for mulching operations on cattle pasture.

The seeder should similarly have low energy consumption. Consequently, the drill seeding is not suitable, because of its traction power requirement for soil tillage. Broadcast seeding, methodology in which the seeds are casted onto the soil surface, corresponds more closely to the conditions of pasture maintenance. Considering the problems appearing by soil compaction low weight of the seeder is preferred. Furthermore, the seeding rate needs to be adjustable and the farmer has to have a possibility to change it before the robot starts its operation on the paddock. Considering different growth intensities within one paddock the final product of the pasture robot should provide variable seeding rates on different paddock zones. As there is a mixture of different seed types, a segregation of the seeds by vibrations during the transport on the rough pasture must be avoided by e.g. a stirrer if applicable. Under windy weather conditions

an even distribution must be provided. That means the flight path of the seed must be minimised by placing it very close to the ground. Finally the seed container must protect the seeds against rain or damp air. Based on these requirements a fertilizer spreader, which was developed at the Bavarian State Research Center for Agriculture [21], will be modified in order to provide controlled seeding on the pasture.

B. i-LEED Software

1) Mission planning

The mission planning interface allows either: selecting of waypoints on a georeferenced map directly, in order to define the trajectories for the robot, or generating of parallel trajectories to cover a whole paddock automatically, with respect to a chosen spacing. As an example, Figure 6 illustrates automatically generated trajectories to cover an entire paddock with 1.5m and 10m spacing respectively. At the end of each track, the half-turn (180 degrees turn) trajectories however needs to be calculated carefully, taking into account different parameters such as the dimensions of the vehicle wheel-base, the maximum front-wheel steering angle, the maximum angular velocity of the front-wheels with respect to the vertical axis and the velocity of the vehicle during the manoeuvre. Figure 5 presents several half-turn trajectories, calculated for differently defined working widths (spacing between adjacent trajectories). The tightest half-turn is illustrated with the thick black line, and the turn which reaches the null curvature at 90 degrees, allowing to insert a line segment at that point if higher spacing is required, with thick light grey line. If the distance between the adjacent trajectories needs to be arranged between these two previously described cases, a half turn with a slight overlapping of the headland is needed, as presented with the dotted black line. If the defined working width is too tight, a loop-turn (bulb-turn) is calculated, as presented with the dotted grey line.

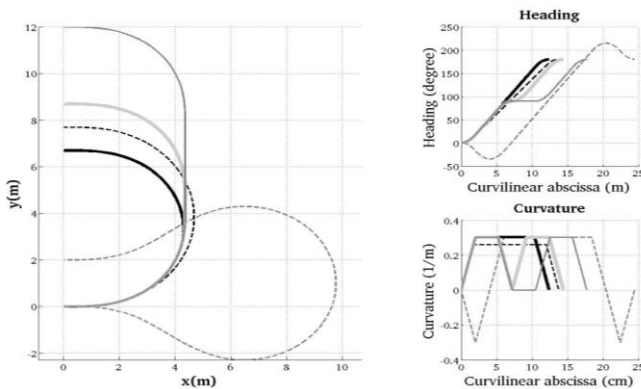


Figure 5. Half turn with respect to different inter-distances

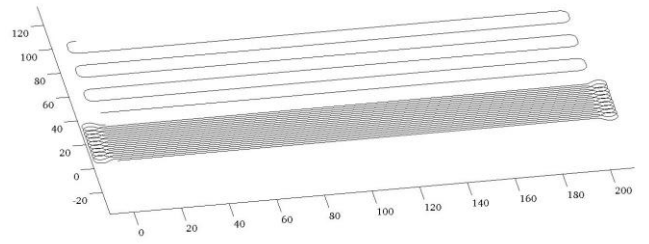


Figure 6. Full and partial coverage

1) Robot control

The classical kinematic modelling of a car-like vehicle can be complemented by sliding parameters. The approach is described through equations of motion of the robot with respect to the path to be followed (i.e. in terms of curvilinear abscissa, and lateral and angular deviations). This model can be converted into an almost linear one using the theory of chained forms [22]. The derivations with respect to the time are replaced by derivations with respect to the curvilinear abscissa, aiming to obtain control performances independent from the vehicle velocity. This step is essential while it enables in particular independent development of steering and speed controllers. The control theory of linear systems complemented with model predictive control techniques can then be used to compensate the delay of the steering actuator. The delay needs to be avoided because it could lead to significant overshoot, especially at each beginning and end of curves.

To ensure the stability of the robot and prevent the risk of rollover, for example during sharp turns at high speed, the proposed approach use the on-line estimation and prediction of a stability criterion - the lateral load transfer (LLT) [23], in order to limit and slow down the robot velocity in case of risk situations. The LLT represents the repartition of the normal components of the tire-ground contact forces. It can be calculated from the roll-model of the vehicle, requiring the knowledge of different parameters as the mass and track of the vehicle, the location of the center of gravity, but also the lateral acceleration. To predict the evolution of the LLT, it is therefore necessary to predict the lateral acceleration. For that, a yaw model of the vehicle is considered, which includes some variables which cannot be directly measured e.g. the global sideslip angle and the front and rear cornering stiffnesses. These variables can nevertheless be estimated through the design of observers.

V. CONCLUSIONS AND FURTHER WORK

The i-LEED project contributes to the following goals of the CAP and the Standing Committee on Agricultural Research (SCAR) of the European Commission:

1. Maintenance of permanent pasture [control of certain unfavourable plants (nettles, shrubs, trees etc.) without using herbicides; maintenance of a dense sward in order to avoid soil erosion and sward degeneration and enhancement of the pasture productivity for high quality products of ruminants

2. Sustainable agricultural production and resource conservation [optimised feed supply for the cattle due to known amount of available pasture, avoiding oversupply or feed shortages and therefore metabolism and health problems for animals; enhancement of the ecosystem permanent grassland by using site specific, indigenous seeds and site and phytocenosis specific management; better distribution of cowpats (and nutrients) and therefore reduced loss of nutrients due to higher growth rates and earlier grazing of areas around cowpats after regrowth and affecting and killing fewer insects with the mulcher, because with the robot only parts of the paddock, where it is necessary, will be mulched]

3. Facilitating the establishment of young farmers, fostering the employment in rural areas and improving the quality of life in rural areas [work activities shift to more control tasks involving modern technology, therefore the farm as the workplace will become more attractive for young farmers; acquired skills involving modern technologies will open opportunities for the young farmer for extra income from non-agricultural activities and better competitiveness of permanent grassland due to higher productivity, lower working time requirements and the proposed higher direct payment].

Highly automated machine function is an emerging technology within the agricultural sector. No standards exist today relating to this domain. Currently for outdoor agricultural robotic applications, the main referential to link up is the 2006/42/CE machine directive dedicated on health and safety protection of operators. This directive demands from the manufacturer to take all relevant solutions and necessary measures to reduce as much as possible the risks after a failure mode and effects analysis (FMEA), but without any considerations of robotic issues at the time of this directive elaboration in the last century. One important issue will be the further development of guidelines, directives and standardisation e.g. within the ISO working group "Agricultural autonomous machines", in order to allow straight forward development of robotics in field of agriculture.

REFERENCES

- [1] OECD/FAO (2012), OECD-FAO Agricultural Outlook 2012-2021, OECD Publishing and FAO. http://dx.doi.org/10.1787/agr_outlook-2012-en
- [2] Coyette, C., H.Schenk (eds.) (2011) Agriculture and fishery statistics, 2011 edition. Eurostat, European Union.
- [3] Brundtland-Report (1987). World Commission on Environment and Development. Our common future. Oxford University Press, N.Y.
- [4] A. A. Jongebreur (2012). Technology and Sustainability in Livestock Systems. A Review. International conference of agricultural engineering, CIGR-AgEng2012, Valencia 8-12 July 2012, Papers book, ISBN 978-84-615-9928-8 p.6.
- [5] Tai, M., Hingwe, P., and Tomizuka, M. (2004). Modeling and control of steering system of heavy vehicles for automated highway systems. IEEE/ASME Transactions on Mechatronics, 9(4):609-618
- [6] Ellouze, M. and Andra-Novet, B. d. (2000). Control of unicycle-type robots in the presence of sliding effects with only absolute longitudinal and yaw velocities measurement. European Journal of Control, 6(6):567-584.
- [7] Hac, A., Brown, T., and Martens J. (2004). Detection of vehicle rollover, In SAE World Congress, Detroit, USA
- [8] Wang, D. and Low, C. (2007). An analysis of wheeled mobile robots in the presence of skidding and slipping: Control design perspective. In IEEE International Conference on Robotics and Automation (ICRA) Roma, Italy, pp. 2379-2384
- [9] Vougioukas S. (2007). Path tracking control for autonomous tractors with reactive obstacle avoidance based on evidence grids. In Precision Agriculture 07. ed. J. Stafford, Wageningen (Netherlands), Wageningen Academic Publishers, 2009, pp. 483-490
- [10] Ayers, P.D. (1994). Environmental damage from tracked vehicle operation. Journal of Terramechanics 31:173-183
- [11] E.J. van Henten, C.J. van Asselt, S.K. Blaauw, M.H. Govers, J.W. Hofstee, R.M. Jansen, A.T. Nieuwenhuizen, S.L. Speetjens, J.D. Stigter, G. van Straten, L.G.E.J. van Willigenburg: WURking (2009). A small sized autonomous robot for the farm of the future, in Precision agriculture '09, E.J. van Henten, D. Goense and C. Lokhorst, Wageningen (Netherlands), Wageningen Academic Publishers, 2009, pp. 833-840
- [12] Ruckelshausen, A., Biber, P., Dorna, M., Gremmes, H., Klose, R., Linz, A., Resch, R., Thiel, M., Trautz, D., and Weiss, U. (2009). Bonirob: an autonomous field robot platform for individual plant phenotyping. in Precision agriculture '09, E.J. van Henten, D. Goense and C. Lokhorst, Wageningen (Netherlands), Wageningen Academic Publishers, 2009, pp. 841-847
- [13] Bakker T., Van Asselt C.J., Bontsema J., Müller J., Van Straten G., (2009). Simple tunable control for automatic guidance of four-wheel steered vehicles in Precision agriculture '09, E.J. van Henten, D. Goense and C. Lokhorst, Wageningen (Netherlands), Wageningen Academic Publishers, 2009, pp. 867-875
- [14] Eaton, R., Katupitiya, J., Siew, K. W., and Dang, K. S. (2008). Precision guidance of agricultural tractors for autonomous farming. In 2nd Annual IEEE Systems Conference, pp. 1-8
- [15] Lucet, E., Grand, C., Salle, D., and Bidaud, P. (2008). Stabilization algorithm for a high speed car-like robot achieving steering maneuver. In IEEE International Conference on Robotics and Automation (ICRA), Pasadena, CA, USA, pp. 2540-2545
- [16] Lenain R., Thuilot B., Cariou C., Martinet P., (2010). Mixed kinematic and dynamic sideslip angle observer for accurate control of fast off-road mobile robot. Journal of Field Robotics, 27(2):181-196, 2010
- [17] ENERGREEN (2014). Data sheet „RoboZero“, ENERGREEN srl., Cagnano di Pojana Maggiore, Italy, 2014.
- [18] Tekin, A. B., Yurdem, H., Zizis, T., F, Spyros, Aygun, T., (2013). "Design and implementation of RoboTurk robotic platform". EFITAWCCA-CIGR Conference "Sustainable Agriculture through ICT Innovation", Turin, Italy, 24-27 June 2013.
- [19] Pepper&Fuchs GmbH (2014). Operation Instructions - OMDxxx-R2000 - Ethernet communication protocol, Pepper&Fuchs GmbH, Mannheim, Germany, 2014 http://files.pepper-fuchs.com/selector_files/navi/productInfo/doct/doct3469a.pdf (accessed on: 16.09.2015)
- [20] Fraichard, T. and Scheuer A. (2004). From Reeds and Shepp's to continuous-curvature paths. IEEE Transactions on Robotics and Automation, 20(6):1025-1035
- [21] Fröhlich, G., Bröker, K., Link, H., Rödel, G., Wendling, F., & Wendl, G. (2007). Precision Experiments on Computer-controlled Fertilizer - Distribution on Experimental Plots. Landtechnik - Agricultural Engineering, 62(3), 150-151. doi:<http://dx.doi.org/10.1515/lt.2007.963>.
- [22] Samson, C. (1995). Control of chained systems. Application to path following and time-varying point stabilization of mobile robots. IEEE Transactions on Automatic Control, 40(1):64-77
- [23] Solmaz, S., Corless, M., and Shorten R. (2006). A methodology for the design of robust rollover prevention controller for automotive vehicles : Part 1 - differential braking. In 45th IEEE Conference on Decision and Control, San Diego, U.S.A, 2006.

Initial field-testing of Thorvald, a versatile robotic platform for agricultural applications

Lars Grimstad, Huynh N. T. Phan, Cong D. Pham, Nils Bjugstad, Pål J. From
Department of Mathematical Sciences and Technology,
Norwegian University of Life Sciences, 1432 Ås, Norway.
{larg, huph, coph, nilsbj, pafr}@nmbu.no

Abstract—Much effort has been put into developing robotic systems for the agricultural domain that are able to perform specific tasks such as yield estimation, phenotyping, sampling, precise application of pesticides, and so on. Some robots have also been developed for more energy-demanding tasks such as seeding, but little work has been done to make more versatile systems that are able to perform tasks of great variety in energy demand, required precision, operation speed, etc. In this paper we present a novel robotic platform capable of performing both the energy-demanding tasks previously performed by heavy tractors, and in addition the more precise around-the-clock operations normally identified with agricultural robotics. We present results from a field experiment on seeding patterns and densities, and from field-tests done in cooperation with researchers working in phenotyping of cereals. We also show that the robot is well suited for monitoring tasks, and that we can obtain valuable information about the condition of the plants and weed by a standard camera and simple image analysis.

I. INTRODUCTION

In agricultural robotics, effort is often put into developing task-specific robots. That is, robots that are custom built to solve one specific task in the field, like mechanical weeding, crop scouting or applying herbicides by precision spraying. There are many impressive robots and concepts, but most are not designed with exchangeable tools and energy demanding tasks in mind. There are some exceptions to this though, such as Robotti by Kongskilde [1]; a tracked robot which can be fitted with multiple implements. Robotti's effective traction capability is 10 hp, and it has a mass of less than 500 kg.

It is our belief that the farmer will not replace his or her tractors with robots, partially or completely, if it does not make sense economically. Robotic solutions are generally expensive, and will probably continue to be so in the foreseeable future. Independently of the task to be performed, they need to be equipped with advanced sensory systems such as RTK GNSS, LIDAR and cameras that represent a substantial cost increase. One way to make robotic solution more economically viable, is to make them more versatile. We believe strongly in developing robotic systems that are able to perform several different tasks, and in this way represent an added value to the farmer, both economically and in increased life quality, and to the consumer, in improved food quality and lower prices.

Another important aspect in this setting is the fact that heavy machinery damages the soil by causing soil com-

paction [2], [3]. Balckmore *et al.* [4] estimates that as much as 80-90 % of the energy input in the field may be eliminated by using lightweight machines. This is why efforts should be put into designing complete solutions based on lightweight robots that are capable of solving all required tasks, from seeding to harvesting, eliminating heavy machines from as much of the field as possible.

Robots that are to perform energy-demanding tasks in the field need to be constructed differently from robots that are merely made for collecting data. Even though some robots that are able to perform several different tasks are presented in literature, they are normally not capable of performing a wide variety of tasks. Robots that are constructed for monitoring are generally not powerful enough or the center of mass is too high for them to perform energy-demanding tasks in the soil. One example of such a robot is the BoniRob [5], [6], which can be fitted with several different tools for monitoring, data collection, and other tasks that are not too energy-demanding.

On the other end of the scale, we have large and heavy robots, or autonomous tractors for that sake, powerful enough to perform any task, but lack the benefits represented by the lightweight robots. Examples of such robots are the APU module [7] and the Spirit autonomous tractor [8].

We present *Thorvald*, a novel robotic platform that is powerful enough to perform energy-demanding operation in the soil, and at the same time has the beneficial properties of lightweight, autonomous robots. The Thorvald platform was designed and built at the Norwegian University of Life Sciences. It has a low center of gravity, and a total mass of approx. 150 kg. It uses four 600 W brushless motors connected via toothed belts to in-wheel gearboxes for propulsion, which is believed to sufficient to perform the most critical tasks in the field. Even though the robot itself is lightweight, the tools that are attached to the robot will add the necessary weight to perform each task. Thus, for monitoring and surveillance, the robot is sufficiently light weight not to damage the plants and the soil and to maintain a long operation time, while for more energy-demanding tasks, such as seeding, the seeding tool will add the necessary weight to obtain the required traction and stability.

The robot has individual steering motors for each wheel, which makes it highly maneuverable, and the frame members and frame joints are made somewhat flexible to ensure that

TABLE I: Thorvald Key Specifications

Drive power	4 x 600 W
Battery	48 V, 30 Ah, LiFePO4 (capacity can be doubled if needed)
Mass	~ 150 kg
Payload	200 kg
Ground clearance	59 cm



Fig. 1: The Thorvald platform. Attached is an early prototype of a precision seeding tool.

all wheels will remain in contact with the ground, even in rough terrain. This is critical for traction, which is especially important on Norwegian farms, where the fields often are uneven and hilly. The flexible frame design was chosen as it is lighter, less expensive and less complex than traditional suspension systems.

Thorvald has a waterproof on-board computer from Small PC, which runs ROS (Robotic Operating System) on Linux Ubuntu. A heavy-duty, weather-proof, high brightness touch screen from Small PC has been installed for easy operation together with an emergency stop button. The steering motors from JVL have built in motor controllers while the four propulsion motors are connected to two dual channel motor controllers from Roboteq. All motor controllers are connected to, and communicate with the on-board computer via a CANopen network. Table I lists the robot's key specifications. The Thorvald platform is depicted in Figure 1.

We are currently developing our own precision seeder as described in [9], which distributes the seeds evenly across the field in a hexagonal circle packing pattern. This paper presents results from a small experiment conducted in connection with the development of this tool.

The robot is equipped with all sensors required for reliable, autonomous navigation, and different tools, or implements, are attached within the robot frame according to the task that is to be performed. The tool is installed by backing the robot towards the tool until the tool is within the robot frame. The tool will then connect to the frame at three different points, as shown in Figure 2. Currently the tool is fastened manually, but in the future this will be done automatically.

We wish to show that with our simple design, we are able to perform both energy-demanding tasks and also the monitoring and information gathering part using the same robot.

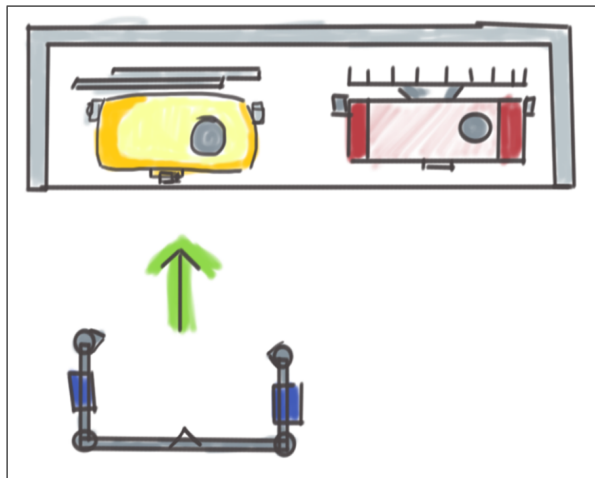


Fig. 2: Thorvald is designed to be used with multiple implements

The reader should note that we do not intend to plow the field, as plowing is highly energy demanding, and leaves the soil vulnerable to the elements, which in turns leads to soil erosion. Instead we wish to use no-till practices. By not plowing, there will be an increased problem with weeds. It is our belief that this problem can be reduced by seeding in a more uniform pattern, and by developing precision weeding tools to be used together with the robotic platform.

An important part of robotic farming is data collection. Modern technology allows us to do work in the field on a single-plant level, as opposed to treating all plants in a field or sub-field in the same way. The Thorvald platform will therefore be equipped with sensors for crop scouting, and the robot is currently being tested by researchers working in cereal phenotyping.

The paper is organized as follows: In Section II we discuss the effect of different seeding patterns and seeding densities, while Section III addresses crop scouting. Section IV presents results from a small experiment on seeding patterns conducted at our research farm, and Section V results from field-tests conducted in cooperation with plant researchers.

II. PRECISION SEEDING

Conventional seeding places seeds in rows, with short spacing within the row, and considerably larger spacing between rows. This means that inter-row weeds are free to develop while the crop is competing against itself within the rows (Figure 3a). The reason the seeds are placed in this way has to do with the way the machinery works (i.e., what is most easily obtained mechanically), and not what is ideal for growth and weed suppression. Studies show that seeds that are placed in a more uniform pattern (Figure 3b) are more capable of suppressing weeds, which can be directly translated into increased yield. For example, in Weiner *et al.* [10], [11] it is shown that the advantages of initial size in competition among individual plants is highly favorable to the crops and that weed is considerably more suppressed

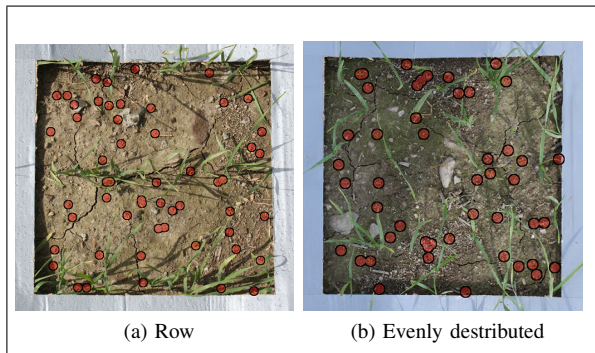


Fig. 3: With conventional row seeding, weeds (red circles) are free to develop undisturbed by the crop

when the crop density is increased and the crop is uniformly distributed in the field, as opposed to rows. Heege *et al.* [12] presents a detailed discussion on the effects of row distances from a more mechanical point of view. More recent studies show the same effects on crops normally sown with lower densities, such as maize [13].

Based on the the strong indications found in literature showing that crops can substantially gain from a more uniformly distributed seeding pattern, especially under high weed pressure and asymmetry, we believe there is a lot to gain from developing seeding tools that are able to place the seeds more uniformly and accurately. We are currently working on several different approaches that allow us to place seeds in this way. The main advantage, as we see it, is that by using a robot that is substantially cheaper than existing tractor-based systems, and therefore can be scaled up in numbers and not in size, and also allows for 24 hour operation, we can develop systems with less pressure on productivity (per unit) and speed. This allows for far more accurate seeding machines that are able to accurately place the seeds in a required pattern.

The first step of this process is to get a better understanding of what is the ideal density and pattern for different kinds of crops under different weed pressure. By distributing the seeds more evenly across the field, each plant will have more room to develop in all directions, not just on each side of a dense row. The plant will then be able to collect more sunlight, and of course take sunlight from slower developing plants such as most weeds. We study the effects of changing the seeding pattern in Section IV.

The seeder being developed for Thorvald, seeds in an hexagonal pattern. An early prototype is currently being tested with the robot (Figure 4). Based on the results from the experiment described in this paper, the seeder will be modified to place seeds in the optimal pattern, and the experiments will be repeated on a larger field and under different conditions, such a weed pressure, soil structure, fertilization practices, etc.

III. MONITORING

An ongoing project is to enable the robot to be used for crop scouting. A downward facing camera has therefore been



Fig. 4: Thorvald with an early precision seeding tool prototype



Fig. 5: Thorvald is taking pictures in the field

mounted on the robot (Figure 5). The camera is connected to the on-board computer via USB. A 2D laser scanner has been acquired. This will make the robot able to measure crop height and other parameters related to crop health, and also enable the robot to identify weed, calculate plant coverage and so on. All data collected will be tagged with position using the on-board RTK-GNSS system, which is also to be used for navigation.

Figure 6 shows early results from a test plot seeded with a hexagonal circle packing pattern. Image processing software, ImageJ [15] is used to separate the green plants from the surrounding ground (color thresholds in the HSB color space, no other filters are applied). Today plant coverage is often measured just by visual inspection, so the requirements for accuracy are not particularly high. With this dense pattern, we see that approx. 37 % of the ground is covered by the plants. Here the plants are still at an early stage, as the picture was captured only 16 days after seeding.

In the future we also wish to extend the robots sensor systems to include a pH-meter for measuring soil pH. If the pH gets too low, the yield will be affected in a negative manner. For best results, pH should be measured continuously and on site [14]. Measuring the pH across the field, will then allow us to apply the correct amount of lime where this is needed, and keep the entire field within the acceptable pH level.



Fig. 6: Hexagonal pattern with 2.5 cm seed spacing (pattern 3), with plant coverage of approx. 37 %. Picture with and without highlighted plants.

TABLE II: Number of crop and weed in a 25x25 cm area for the different sowing patterns

Pattern	Crop	Weed	Crop-weed ratio
Row, 2 cm	21	45	0.47
Uniform, 5 cm	30	47	0.64
Uniform, 2.5 cm	92	30	3.1

IV. SEEDING EXPERIMENT

To investigate the benefits of seeding in a more uniform pattern, simple tools for seeding (by hand) was designed and 3D printed. Some of the tools are depicted in Figure 7. The tools were made so that each seed would be placed at 3 cm depth with the correct spacing to neighboring seeds. Spring wheat was then seeded by hand in three different patterns using these tools:

- 1) Row: 12.5 cm between rows with 2 cm seed spacing (400 seeds/m²)
- 2) Hexagonal circle packing pattern: 5.0 cm seed spacing (462 seeds/m²)
- 3) Hexagonal circle packing pattern: 2.5 cm seed spacing (1848 seeds/m²)

Figure 8 shows examples of row and hexagonal patterns. For pattern 1 and 2, 1.5 m x 1.5 m squares were seeded. Because of the high number of seeds required for pattern 3, a smaller area was used for this plot.

Pattern 3 turned out to be difficult to seed with the aforementioned hand seeding tool, and the resulting plant pattern, although uniform, did not fully resemble the targeted hexagonal pattern.

Two months after seeding, four 25x25 cm squares were randomly selected for each seeding pattern, and the heights

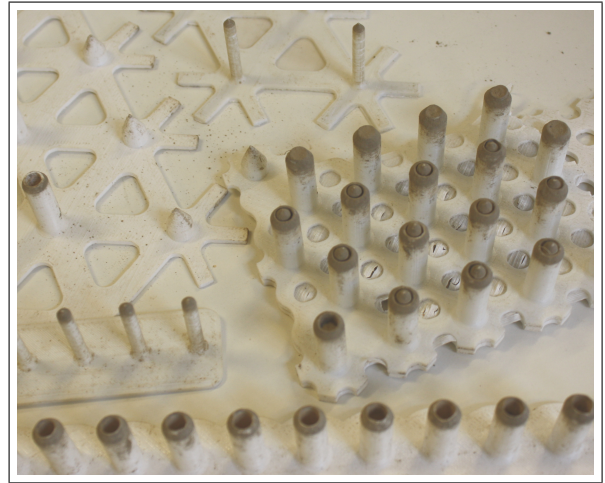


Fig. 7: Tools used for seeding in different patterns

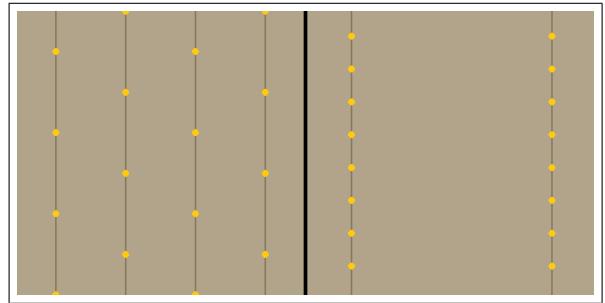


Fig. 8: Hexagonal (left) and row seeding pattern

of wheat plants and weeds were measured. We also counted the number of wheat plants and weeds in each case. The results were as follows:

- The 2 cm row pattern had the highest plants, with average wheat height of 55 cm and average weed height of 11 cm.
- The uniform 5 cm pattern had medium sized plants, with average wheat height of 48 cm and average weed height of 7.4 cm.
- The uniform pattern with 2.5 cm spacing had the smallest weeds size and a substantially better crop-weed ratio compared to the other plots, but it also had the smallest wheat plants.

Figure 9 and 10 compare the wheat height and weed height of the 2 cm row pattern and the 5 cm uniform pattern in more detail, as these have approximately the same seed density. From the figures we see that the wheat plants are somewhat higher for the row pattern, but for the weed the relative difference in size is considerably larger with an average size of about 11 cm for the row pattern and 7.4 cm for the uniform pattern. This is a strong indication that the uniform pattern is better than rows when it comes to suppressing weeds. However, it is not possible to draw a conclusion that this advantage in weed suppression translates in an advantage in growing conditions for the crop. Further experiments with larger test areas and where the plant density

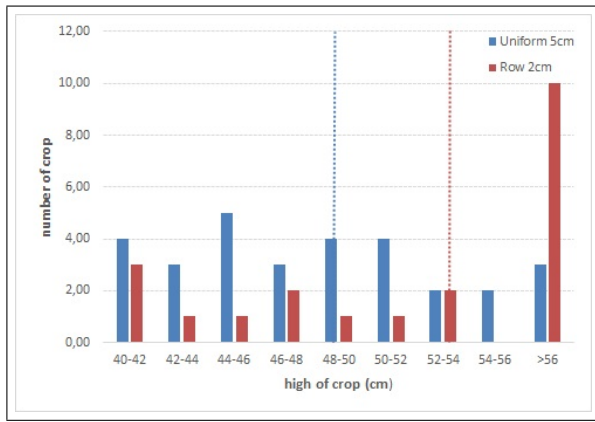


Fig. 9: Wheat size in 25x25 cm area of 2 cm row, and 5 cm uniform patterns. The dotted lines show the average heights.

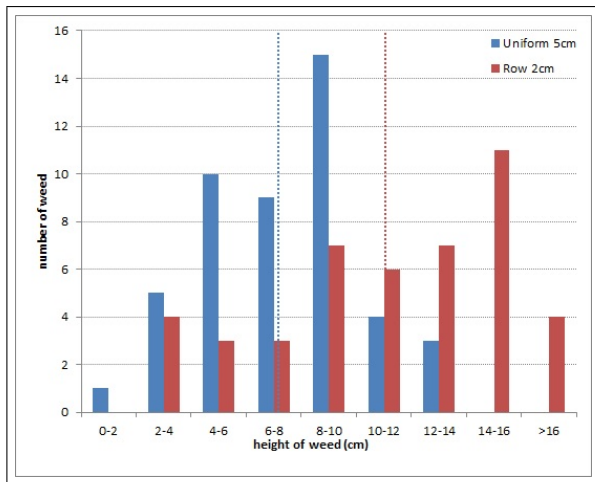


Fig. 10: Weed size in 25x25 cm area of 2 cm row, 5 cm and uniform patterns. The dotted lines show the average heights.

for the different patterns are equal are needed to conclude on this. The number of crop plants and weeds is shown in table II. We see that the crop-weed ratio is better for the uniform patterns.

V. FIELD-TESTS

In order to identify requirements for the aforementioned crop scouting system, Thorvald has been used in cooperation with researchers working with phenotyping of cereals. During these tests, the robot was teleoperated, taking pictures with the on-board camera at different locations in the test fields. Figure 11 shows pictures that have been captured by the robot in the field for an experiment on seeding density and fertilization. The pictures are used to estimate the plant coverage.

The feedback regarding the robot's performance was mainly positive, but as the researchers who used it are working with cereal, they found it to be somewhat low. During the tests the plants were still young and the robot was able to drive over the crop without any danger of harming the plants, but the researchers also require the robot to be

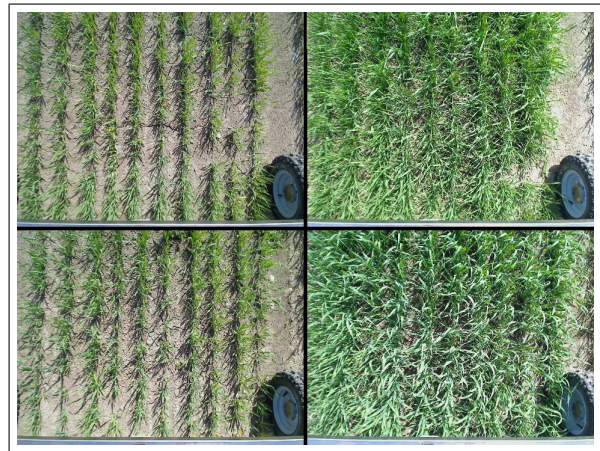


Fig. 11: Images captured by Thorvald's on-board camera

able to drive over fully grown crops. Fully grown crops are about 1 m high, and can in some cases reach heights of 1.5 m.

As Thorvald is designed to be used on farms, and not by plant researchers, a low center of gravity is more important than the ability to drive over fully grown cereal crops. The robot's ground clearance is similar to what one finds on a regular tractor, and it will be able to perform scouting and weed control tasks until the crop has grown to a size where it prevents sunlight from reaching the ground, and thus stops new weeds from developing.

The researchers also found the wheel modules to be a bit wide. Again the concern was that plants could get damaged. This is an issue we will address, and improvements to the design will be made.

As for the maneuverability and traction, the robot performed better than expected. It drives up steep slopes with ease and have good traction capabilities on a range of different surfaces. In rough terrain, all four wheels maintain contact with the ground, and the robot did not get stuck once during the tests.

Thorvald is frequently out in the field to test algorithms as well as the mechanical design of the platform and the tools. It is also recording data to be used in the development of new tools and systems, e.g. recording video of cereal crops to be used as reference when developing algorithms for weed identification. The development of the Thorvald platform will continue during the fall and winter of 2015/2016, and more extensive field-tests will be carried out in the spring and summer of 2016.

VI. CONCLUSION

The Thorvald project aims to develop a lightweight robot that is capable of performing all tasks in the field, also the energy demanding ones. Thus, we have constructed a powerful robot with low mass and a low center of gravity. The latter of these properties also renders it unsuited for phenotyping of cereal, as the robot is too low. However, Thorvald has a ground clearance similar to what one can

find on a normal tractor, and we therefore believe the height to be adequate for the average farmer.

The results from our small experiment on seeding patterns suggest that it may be beneficial to seed in a uniform pattern as opposed to seeding in rows, as the experiments show that a uniform seeding pattern can suppress weed more efficiently. It is, however, not possible to draw any conclusions from the experiments whether this advantage in weed suppression translates into improved growing conditions for the crop. Large-scale experiments need to be carried out to confirm, and better quantify the potential gain by utilizing the proposed seeding patterns.

The first field-tests of the Thorvald platform show promising results. The mechanical design, maneuverability and traction capabilities are shown to be as expected and in some cases somewhat better than expected.

REFERENCES

- [1] O. Green, T. Schmidt, R. Pietrkowski, K. Jensen, M. Larsen, G. Edwards, and R. Jørgensen, "Commercial autonomous agricultural platform - kongskilde robotti," *Second International Conference on Robotics and associated High-technologies and Equipment for Agriculture and Forestry*, 2014.
- [2] M. Nawaz, G. Bourrié, and F. Trolard, "Soil compaction impact and modelling. a review," *Agronomy for Sustainable Development*, vol. 33, no. 2, pp. 291–309, 2013.
- [3] T. Batey, "Soil compaction and soil management—a review," *Soil use and management*, vol. 25, no. 4, pp. 335–345, 2009.
- [4] B. Blackmore, H. Griepentrog, S. Fountas, and T. Gemtos, "A specification for an autonomous crop production mechanization system," *Agricultural Engineering International: the CIGR Ejournal*, 2007.
- [5] A. Ruckelshausen, P. Biber, M. Dorna, H. Gremmes, R. Klose, A. Linz, F. Rahe, R. Resch, M. Thiel, D. Trautz, and U. Weiss, "Bonirob: an autonomous field robot platform for individual plant phenotyping," *Precision agriculture*, vol. 9, no. 841, 2009.
- [6] W. Bangert, A. Kielhorn, F. Rahe, A. Albert, P. Biber, S. Grzonka, S. Haug, A. Michaels, D. Mentrup, M. Hänsel *et al.*, "Field-robot-based agriculture: "remotefarming. 1" and "bonirob-apps";" in *71th conference LAND. TECHNIK-AgEng 2013*, 2013, pp. 439–446.
- [7] T. Oksanen, "Accuracy and performance experiences of four wheel steered autonomous agricultural tractor in sowing operation," in *Field and Service Robotics*, ser. Springer Tracts in Advanced Robotics, L. Mejias, P. Corke, and J. Roberts, Eds. Springer International Publishing, 2015, vol. 105, pp. 425–438.
- [8] "Autonomous tractor corporation," <http://www.autonomoustractor.com/index.html>.
- [9] L. Grimstad, C. D. Pham, H. T. Phan, and P. J. From, "On the design of a low-cost, light-weight, and highly versatile agricultural robot," in *2015 IEEE Workshop on Advanced Robotics and its Social Impacts (ARSO 2015)*, to be published.
- [10] J. Weiner, H.-W. Griepentrog, and L. Kristensen, "Suppression of weeds by spring wheat triticumaestivum increases with crop density and spatial uniformity," *Journal of Applied Ecology*, vol. 38, no. 4, pp. 784–790, 2001.
- [11] J. Weiner, P. Stoll, H. Muller-Landau, and A. Jasentuliyana, "The effects of density, spatial pattern, and competitive symmetry on size variation in simulated plant populations." *The American Naturalist*, vol. 158, no. 4, pp. pp. 438–450, 2001.
- [12] H. Heege, "Site-specific sowing," in *Precision in Crop Farming*, H. J. Heege, Ed. Springer Netherlands, 2013, pp. 171–192.
- [13] C. Marín and J. Weiner, "Effects of density and sowing pattern on weed suppression and grain yield in three varieties of maize under high weed pressure," *Weed Research*, vol. 54, no. 5, pp. 467–474, 2014.
- [14] M. Pansu and J. Gautheyrou, *Handbook of soil analysis: mineralogical, organic and inorganic methods*. Springer Science & Business Media, 2007.
- [15] W. Rasband, "Imagej," U. S. National Institutes of Health, Bethesda, Maryland, USA, <http://imagej.nih.gov/ij/>, 1997-2014.

Increasing the Precision of Generic Crop Row Detection and Tracking and Row End Detection*

Georg Halmetschlager

Johann Prankl

Markus Vincze ¹

Abstract—Agricultural field robots need to navigate within crop rows. In order to efficiently perform cultivation work and to avoid damaging plants precise crop row detection and tracking is essential. Hence, we propose a probabilistic crop row detection and tracking approach that fuses visual odometry data with the results of the crop row measurement using a Kalman filter. However, before the Kalman filter can be integrated into our system, we have to explore if our existing solutions comply with several requirements. We test – with real-life in-field data – if and how the row information can be tracked with the information of the visual odometry and investigate if the estimated probability density of the row measurement can be used to adapt the corresponding covariance matrix entries of the Kalman filter. Preliminary results indicate that the fusion of the visual odometry data with the row measurement improve the tracking results and that the probability density of the row measurement can be used to determine its reliability.

I. INTRODUCTION

Most agricultural robots and guided tractors utilize real-time kinematic global positioning systems (RTK-GPS) or laser-based sensors to solve the task of autonomous navigation [1]. Vision systems promise to offer outstanding advantages compared to pure GPS solutions, as they provide higher dimensional information and are inexpensive compared to laser range finders [2]. Hence, we propose a pure machine vision system to solve the task of navigation in row-organized fields. Therefore, the crop rows have to be detected relatively to the robot for the determination of the negotiable track.

Most of the developed vision-based detection algorithms consist of a segmentation step and a subsequent state-of-the-art line detection algorithm such as the Hough transformation [3], [4], [5], [6], [7].

We introduced in [8] a near infrared and depth (NIRD) data based segmentation that enables a height-bias-free detection of the rows within the ground plane and is insensitive to geometric and season caused changes of the plants. The parameter free row detection is realized with a 3D cascaded particle filter and enables online crop row detection. Each hypothesis in the 3D state space describes a parallel line pattern within a 2D plane and consists of the orientation θ , the offset r , and the distance between the lines d . θ and r define a vector that is perpendicular to the closest line and points from the origin of the coordinate system to the

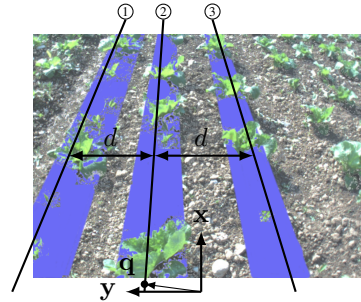


Fig. 1: Geometric model of the crop rows.

point q (cf. Fig. 1). The algorithm offers high detection rates for image sequences that show elongated row structures.

The introduced algorithm can be used to detect and track rows as long as they are in the field of view of the sensor system. However, at the end of the field a turning maneuver has to be executed and the rows disappear. Therefore, an additional solution is needed to track the rows even if they are no longer visible. Moreover, the additional tracking solution could be used to improve and filter the results of the inherent tracking.

Since our vision is to find a GPS-free, pure camera-based, adaptive, overall navigation solution for row organized fields that is independent from a-priori information, we extend our previous approach [8]. We propose to consider the movement of the robot by fusing the data of the (visual) odometry and the result of the row measurement with a Kalman filter to get more stable results.

First tests indicated that the Kalman filter improves the tracking results. Hence, we consider the Kalman filter to be an efficient overall crop row tracking solution even and especially during turn maneuvers at field ends where the row information is completely missing. For this purpose it is necessary to explore if the odometry and row measurement solutions comply with additional requirements. We come up with an approach how the two measurements can be combined within a Kalman filter, we investigate if the visual odometry data can be used to track the detected rows for a short period of time, and if the particle and cluster distribution indicate the reliability of the particle-filter-based crop row detection and how it can be quantized to adapt the covariance matrix of the Kalman filter.

Hence, our contributions are (i) a model to fuse tracked rows from a particle filter with visual odometry data, (ii) an evaluation of the particle filter with the goal to adapt the covariance matrix of the Kalman filter depending on the par-

*This work was funded by Sparkling Science - a programme of the Federal Ministry of Science and Research of Austria (SPA 04/84 - FRANZ).

¹All authors are with Faculty of Electrical Engineering, Automation and Control Institute, Vision for Robotics Laboratory, Vienna University of Technology, A-1040 Vienna, Austria. {gh, jp, mv}@ac.in.tuwien.ac.at

ticle distribution, which is further used (iii) to automatically switch from row tracking to odometry based navigation at the field endings.

II. APPROACH

The selected geometric representation of the crop rows allows modeling the orientation θ and the offset r of the crop rows with a single static point \mathbf{q}_w that lies inside the global coordinate system. In an undisturbed closed system that provides error free robot pose data, the equivalent position of \mathbf{q}_w inside the coordinate system of the robot \mathbf{q}_b can be directly derived from \mathbf{q}_w and tracked without any additional measurement data (cf. Fig. 2a). However, the available position data in our application derived from the visual odometry, is noise afflicted, and the position error accumulates over time.

The probabilistic crop row detection determines the best crop row parameter configuration for the observed scene and has the ability to compensate natural row failures like gaps or plant displacements. However, it can end in a wrong crop row measurement especially if the current scene is not representative for the rest of the field.

Therefore, we fuse the data of the pose measurement with the particle filter based row measurement, to compensate the errors of the one method with additional information from the other. In other words, our goal is to determine and track the position of \mathbf{q}_b based on both, the odometry data and the row measurement (cf. Fig. 1).

First, we come up with a linear model and the corresponding Kalman filter equations for the position (change) of $\mathbf{q}_{b,k}$.

Second, we approach the necessary equations for the odometry based row tracking for an undisturbed system.

Third, we analyze the particle distribution inside a particle filter and check if the modeled probability density functions allows determining the reliability of a measurement.

We introduce with (1) - (4) a linear model for the position and movement of \mathbf{q}_b within the coordinate system of the robot (subsequently the index b is omitted). With the k^{th} state \mathbf{x}_k that contains the position $[q_x, q_y]^T$, the first time derivative (velocity) $[\dot{q}_x, \dot{q}_y]^T$, and the second time derivative (acceleration) $[\ddot{q}_x, \ddot{q}_y]^T$ which is assumed to be zero, aside white noise. \mathbf{w}_k represents the disturbance of the system. Φ represents the dynamic matrix and the matrix \mathbf{G} models the influence of the disturbance on the state change. \mathbf{y}_k contains the k^{th} measurement and consists of the result of the current row measurement $[q_{x,m}, q_{y,m}]^T$ and the odometry based prediction of the position including its first derivative $[q_{x,odo}, q_{y,odo}, \dot{q}_{x,odo}, \dot{q}_{y,odo}]^T$. \mathbf{v}_k represents the measurement noise and the matrix \mathbf{H} models the influence of \mathbf{w}_k on the measurement. T_s represents the constant sampling interval and \mathbf{E} the identity matrix.

$$\begin{aligned} \mathbf{x}_{k+1} &= \Phi \mathbf{x}_k + \mathbf{G} \mathbf{w}_k \\ \mathbf{y}_k &= \mathbf{C} \mathbf{x}_k + \mathbf{H} \mathbf{w}_k + \mathbf{v}_k \end{aligned} \quad (1)$$

$$\mathbf{x}_k = \begin{bmatrix} q_{x,k} \\ q_{y,k} \\ \dot{q}_{x,k} \\ \dot{q}_{y,k} \\ \ddot{q}_{x,k} \\ \ddot{q}_{y,k} \end{bmatrix} \quad \mathbf{y}_k = \begin{bmatrix} q_{x,m} \\ q_{y,m} \\ q_{x,odo} \\ q_{y,odo} \\ \dot{q}_{x,odo} \\ \dot{q}_{y,odo} \end{bmatrix} \quad (2)$$

$$\Phi = \begin{bmatrix} 1 & 0 & T_s & 0 & 0 & 0 \\ 0 & 1 & 0 & T_s & 0 & 0 \\ 0 & 0 & 1 & 0 & T_s & 0 \\ 0 & 0 & 0 & 1 & 0 & T_s \\ 0 & 0 & 0 & 0 & 1 & 0 \\ 0 & 0 & 0 & 0 & 0 & 1 \end{bmatrix} \quad \mathbf{C} = \begin{bmatrix} 1 & 0 & 0 & 0 & 0 & 0 \\ 0 & 1 & 0 & 0 & 0 & 0 \\ 1 & 0 & 0 & 0 & 0 & 0 \\ 0 & 1 & 0 & 0 & 0 & 0 \\ 0 & 0 & 1 & 0 & 0 & 0 \\ 0 & 0 & 0 & 1 & 0 & 0 \end{bmatrix} \quad (3)$$

$$\mathbf{G} = \mathbf{E} \quad \mathbf{H} = \mathbf{E} \quad (4)$$

Equation (5)-(7) describe the approached Kalman filter.

$$\hat{\mathbf{x}}_{k+1} = \Phi \hat{\mathbf{x}}_k + \hat{\mathbf{K}}_k (\mathbf{y}_k - \mathbf{C} \hat{\mathbf{x}}_k) \quad (5)$$

$$\hat{\mathbf{K}}_k = \Phi \mathbf{P}_k \mathbf{C}^T (\mathbf{C} \mathbf{P}_k \mathbf{C}^T + \mathbf{Q} + \mathbf{R})^{-1} \quad (6)$$

with the best estimation $\hat{\mathbf{x}}_{k+1}$ for \mathbf{x}_{k+1} , based on k measurements, and the covariance of the estimation error \mathbf{P}_{k+1} that can be calculated with the discrete Riccati equation. The covariance matrices

$$\text{cov}(\mathbf{v}_k) = \mathbf{R} \delta_{kj} \quad \text{cov}(\mathbf{w}_k) = \mathbf{Q} \delta_{kj} \quad (7)$$

with the $[6 \times 6]$ matrices \mathbf{R} and \mathbf{Q} , and $\delta_{kj} = 1$ for $k = j$, else $\delta_{kj} = 0$. The covariance matrix \mathbf{R} is used to model the reliability of the measurement and influences the significance of the measurement for the state estimation $\hat{\mathbf{x}}_{k+1}$. Hence, the reliability of the current row measurement has to be determined.

A. Row Tracking With Position Data

Equation (8)-(10) describe the position and velocity of \mathbf{q}_b dependent on the position and velocity of the robot. Figure 2b depicts the position change of \mathbf{q}_b if the robot drives along the x axes.

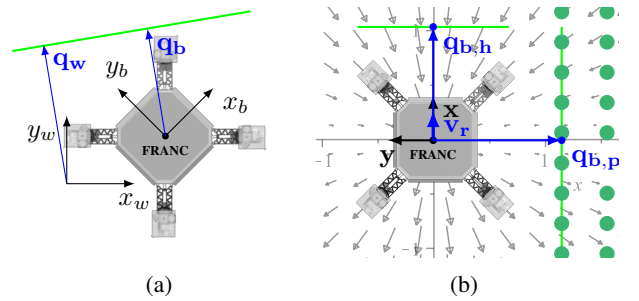


Fig. 2: (a) Parametrization vector for a crop row in the global coordinate system \mathbf{q}_w and inside the coordinate system of the robot \mathbf{q}_b . (b) Movement of the hypotheses depicted with a vectorfield, if the robot moves along its x axes. $\mathbf{q}_{b,h}$: line equation vector of a horizontal line, $\mathbf{q}_{b,p}$: line equation vector of a parallel line, \mathbf{v}_r : velocity of the robot, vectorfield: velocity vectors of the hypotheses in the state space for the given \mathbf{v}_r .

$$r_{b,t} = x_{b,t}\cos(\theta_w) + y_{b,t}\sin(\theta_w) - r_w\sin(\theta_w) \quad (8)$$

$$\theta_{b,t} = \alpha_{b,t} - \theta_w \quad (9)$$

$$\mathbf{q} = \begin{bmatrix} q_x \\ q_y \end{bmatrix} = \begin{bmatrix} r_{b,t}\sin(\theta_{b,t}) \\ r_{b,t}\cos(\theta_{b,t}) \end{bmatrix} \quad (10)$$

$r_{b,t}$ represents the offset of the coordinate system of the robot relative to the line that is static in the world coordinate system, modeled with θ_w and r_w . $x_{b,t}$, $y_{b,t}$ and $\alpha_{b,t}$ describe the pose of the robot inside the world coordinate system, the index b stands for the base of the robot, and t indicates that the variable is time variant.

B. Reliability of the Row Measurement

We aim to derive the reliability of the row measurement dependent on the probability of the parameter configuration for the observed scene.

We sample the state space initially with N randomly generated hypotheses. After each iteration, we redraw $N - M$ hypotheses and reseed M randomly generated hypotheses. The reseeding avoids a degeneration of the particle filter and keeps the estimation dynamic and adaptable. Hence, the particle filter models the probability density function of the parameter configurations for the current observed scene [9]. If the segmentation results in clear row structures, the particles will accumulate in a single region that offers a high particle concentration. If the segmented image contains only sparse information, the particle filter will model the probability density function for the current measurement with several particle clusters that represent different configuration.

III. TESTS AND RESULTS

We tested the row tracking and analyzed the particle distribution of the probabilistic crop row detection with real-life data recorded with the robot FRANC¹ during in-field trials (cf. Fig. 3). We implemented the necessary algorithms in the robot operation system and used an existing visual odometry solution (LIBVISO2, [10]) to gather the position data.



Fig. 3: FRANC during in-field trials.

A. Row Tracking With Position Data

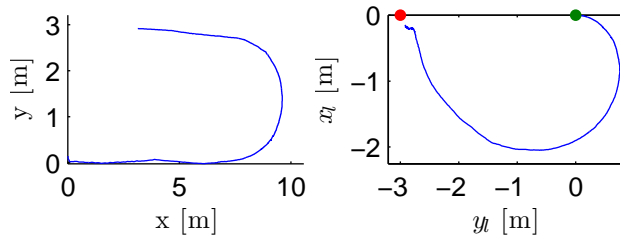
The recorded data contain several turn maneuvers at the end of rows. We selected exactly one of those sequences because of two reasons.

- The turn maneuver offers the biggest variation in the movement of the robot compared to a straight motion parallel to the crop rows.

¹<http://franc.acin.tuwien.ac.at>

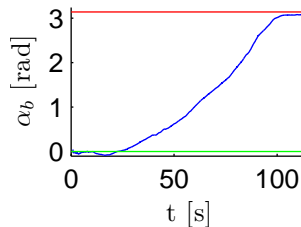
- The crop row detection cannot provide a reliable measurement at the end of a field because the necessary information is missing. However, an overall tracking solution has to provide information even at field ends. Hence, the tracking has to rely on the pure odometry data during turn maneuvers.

We determined the ground truth crop row parameters at the beginning and end of the sequence and compare the results (cf. Fig. 4). The visual odometry fails to track the offset with

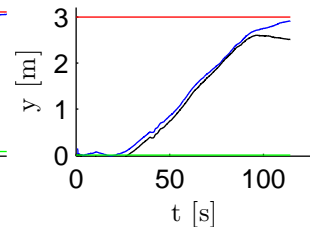


(a) Position change of the robot during the turn maneuver.

(b) Visual odometry based crop row tracking (blue). Green dot: ground truth at start, red dot: ground truth at the end.



(c) Orientation α_b of the robot during the turn maneuver. Green line: ground truth at start, red line: ground truth at the end.



(d) y position of the robot during the turn maneuver. Blue: 1st run, black: 2nd run, green line: ground truth at start, red line: ground truth at the end.

Fig. 4: Odometry data and tracking results.

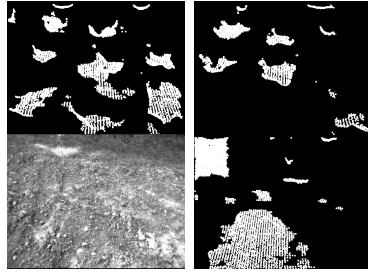
a sufficient accuracy (tracking error: 0.1m to 0.4m) but offers good results for the tracking of the crop row orientation (tracking error: 0.055rad to 0.088rad).

B. Probability Densities of Different Row Measurements

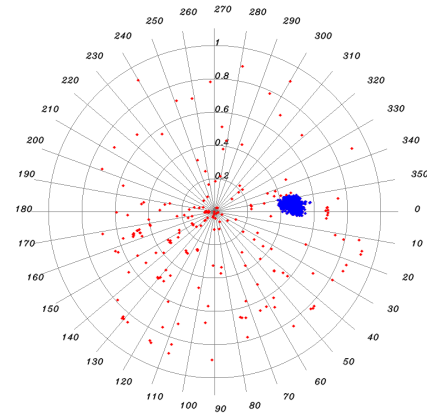
Figure 5 shows several results of the crop row measurement, the better the provided information of the segmentation, the more definite is the row measurement result.

IV. CONCLUSION AND OUTLOOK

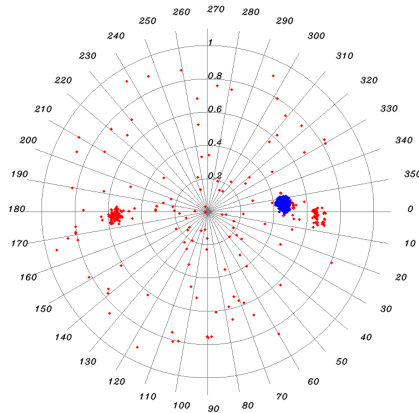
We introduced a simple linear model and approach a Kalman filter as crop row tracking solution to enable a precise GPS-free navigation. Our preliminary results indicate that an odometry based crop row tracking can be used at field endings and have the ability to improve the tracking results of in-field row measurements. However, a better and more precise visual odometry algorithm can further improve the



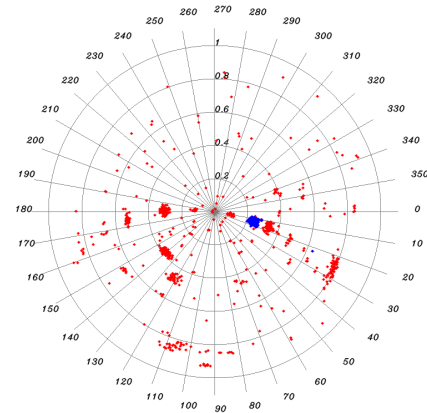
(a) Upper images: dense (left) and sparse (right) segmentation results. Lower images: field ending (left) and corresponding segmentation result (right).



(b) Correct and stable row parameter estimation for dense segmentation results and clear row structures.



(c) Correct estimation for sparse segmentation results, the two biggest cluster can be transformed into each other, a third cluster starts to appear on the right side.



(d) Transition between crop rows and a field ending. The particle filter contains several clusters and the probability that the biggest cluster represents a correct measurement decreases.

Fig. 5: Particle distribution for different field regions and segmentation results.

tracking results. Furthermore, our tests lead to the conclusion that the modeled probability density can be used to determine the reliability of the current crop row parameter estimation, hence enables automatic switching from row tracking to odometry based navigation at the field endings.

REFERENCES

- [1] D. Slaughter, D. Giles, and D. Downey, "Autonomous robotic weed control systems: A review," *Computers and Electronics in Agriculture*, vol. 61, no. 1, pp. 63 – 78, 2008.
- [2] U. Weiss and P. Biber, "Plant detection and mapping for agricultural robots using a 3d lidar sensor," *Robotics and Autonomous Systems*, vol. 59, no. 5, pp. 265 – 273, 2011, special Issue ECMR 2009.
- [3] B. Åstrand and A.-J. Baerveldt, "A vision based row-following system for agricultural field machinery," *Mechatronics*, vol. 15, no. 2, pp. 251 – 269, 2005.
- [4] G.-Q. Jiang, C.-J. Zhao, and Y.-S. Si, "A machine vision based crop rows detection for agricultural robots," in *Wavelet Analysis and Pattern Recognition (ICWAPR), 2010 International Conference on*, 2010, pp. 114–118.
- [5] G. R. Ruiz, L. M. N. Gracia, J. G. Gil, and M. C. S. Junior, "Sequence correlation for row tracking and weed detection using computer vision," in *Workshop on Image Analysis in Agriculture*, 26–27., 2010.
- [6] J. Romeo, G. Pajares, M. Montalvo, J. Guerrero, M. Guijarro, and A. Ribeiro, "Crop row detection in maize fields inspired on the human visual perception," *The Scientific World Journal*, vol. 2012, 2012.
- [7] V. Fontaine and T. Crowe, "Development of line-detection algorithms for local positioning in densely seeded crops," *Canadian biosystems engineering*, vol. 48, p. 7, 2006.
- [8] G. Halmetschlager, J. Prankl, and M. Vincze, "Probabilistic near infrared and depth based crop line identification," in *IAS-13, Workshop on Recent Advances in Agricultural Robotics, Workshop Proceedings of IAS-13 Conference on*, 2014, pp. 474–482.
- [9] S. Thrun, W. Burgard, and D. Fox, *Probabilistic Robotics (Intelligent Robotics and Autonomous Agents)*. The MIT Press, 2005.
- [10] A. Geiger, J. Ziegler, and C. Stiller, "Stereoscan: Dense 3d reconstruction in real-time," in *Intelligent Vehicles Symposium (IV)*, 2011.

Studying Phenotypic Variability in Crops using a Hand-held Sensor Platform

Raghav Khanna, Joern Rehder, Martin Möller, Enric Galceran and Roland Siegwart

Abstract—Recent developments in visual-inertial and LiDAR sensors and simultaneous localization and mapping (SLAM) enable recording and digital reconstruction of the physical world. In this paper we utilize a hand-held multi-sensor platform for remotely recording and characterizing physical properties of crops on a field. The platform consists of a visual-inertial sensor, color camera and 2D LiDAR. We synchronize the data from this platform and fuse them in a standard SLAM framework to obtain a detailed model of the field environment in the form of a 3D point cloud. Such a model is then fed into semi-automated crop parameter estimation pipelines to extract the spatio-temporal variation of physical crop height and canopy cover, which may be used to support decision making for breeding and precision agriculture. We present experimental results with data collected on a winter wheat field in Eschikon, Switzerland, showing the utility of our approach towards automating variability studies in crops.

Index Terms—Precision agriculture, visual-inertial sensor, 3D reconstruction, agricultural robotics, crop phenotyping, point cloud processing

I. INTRODUCTION

Remote, non-invasive monitoring of crops has garnered significant interest in recent times. Crop phenotyping, the application of high throughput methods to characterize plant architecture and performance, is currently a focus in crop research and breeding programs [1], [2]. However, most crop breeding programs currently employ human expert breeders who primarily evaluate plant growth visually. This process is time consuming and expensive, and may be error prone. High throughput phenotyping facilities allow crop variability data collection in controlled environments that can be extrapolated to large-scale crops. These facilities are typically run by large seed and crop care companies and plant research institutions within large, controlled environments, such as greenhouses or growth chambers. This limits their ability to extrapolate and predict plant behavior under heterogeneous field conditions [3]. Large-scale field phenotyping platforms are typically expensive, take a long time for construction and are limited in their area of operation. The increased demand for on-field phenotyping to support breeding [4] has spurred the development of mobile platforms, [5], [6] and [7], based on ground vehicles. Ground vehicles, however, are intrusive, limiting the frequency of the measurements, and have an adverse impact on the soil.

This research was sponsored by the European Communitys framework programme Horizon 2020 under grant agreement no. 644227-Flourish. The authors are with the Autonomous Systems Lab at ETH Zürich (e-mail: {raghav.khanna, joern.rehder, enric.galceran}@mavt.ethz.ch, mar-moell@student.ethz.ch, r.siegwart@ieee.org).



Fig. 1. The hand-held sensor platform used in this work for studying crop variability, comprising of a visual-inertial sensor, a color camera and laser range finder.

Therefore, an easy-to-use, flexible and mobile sensor platform (such as the one shown in Figure 1) can enable breeders and agronomists to quickly and frequently collect real world data about their crops, offering valuable insights into crop status and field variation.

In light of these considerations, we present a light-weight, hand-held system consisting of a high resolution color camera, a laser scanner and a visual-inertial sensor, offering flexibility and ease of use to monitor crops. We show preliminary results in the form of user-readable crop height and canopy cover maps which can be used to study the spatio-temporal growth of the crops on the field. Our height estimates, based on the sensor platform measurements, are also shown to compare favorably with manual measurements. An overview of the pipeline is shown in Figure 2.

II. SENSOR PLATFORM AND CALIBRATION

We employed a combination of the visual-inertial sensor developed at the Autonomous Systems Lab [8], a Hokuyo UTM-30LX laser range finder (LRF) and a rigidly attached Point Grey Flea3 color camera for data collection, as shown in Figure 1. The visual-inertial sensor and LRF were synchronized in hardware, while software synchronization according to Zhang et al. [9] was performed for the color camera. We

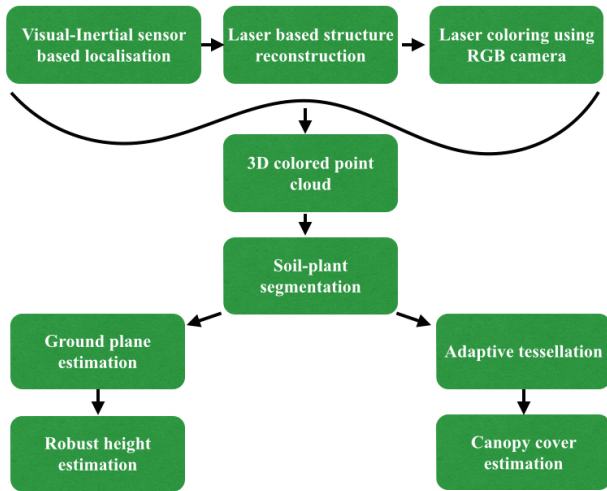


Fig. 2. A schematic overview of our hand-held scanner based phenotypic pipeline.

used the *kalibr*¹[10] framework for calibrating the cameras intrinsically and extrinsically with respect to the inertial measurement unit (IMU), and for determining the communication delay of the color camera. The transformation between IMU and LRF was estimated according to our previous work [11].

Our plant segmentation is based on data acquired with the color camera, exploiting that the spectra of light reflected by plants and soil are generally different. Besides irradiance, image intensity is dependent on the camera response function as well as on the optical transmission of the lens system. We estimated these quantities using the well established empirical model of response [12] as well as a simple polynomial model for vignetting [13], and subsequently compensated for these influences to facilitate segmentation.

III. 3D RECONSTRUCTION

Our 3D reconstruction follows a two-step procedure. In a first step, non-linear optimization [14] over a sliding window of measurements from the visual-inertial sensor provides an initial estimate of the sensor trajectory. While this approach is real-time capable and has been demonstrated to provide state-of-the-art accuracy, we subject the initial trajectory estimate to a full batch optimization [15] in a second step, taking all visual and inertial measurements into account. This offline post-processing step further improves the accuracy of the reconstruction. Given the sensor trajectory, range measurements are transformed into the coordinate frame of our map to produce a point cloud. Subsequently, an irradiance² value is sampled for every point by projecting it into the temporally closest color image.

¹Available at <https://github.com/ethz-asl/kalibr>

²We follow Debevec et al. [16] in using this term. For insights on why this term is not strictly correct and a justification for its use, please see their work.

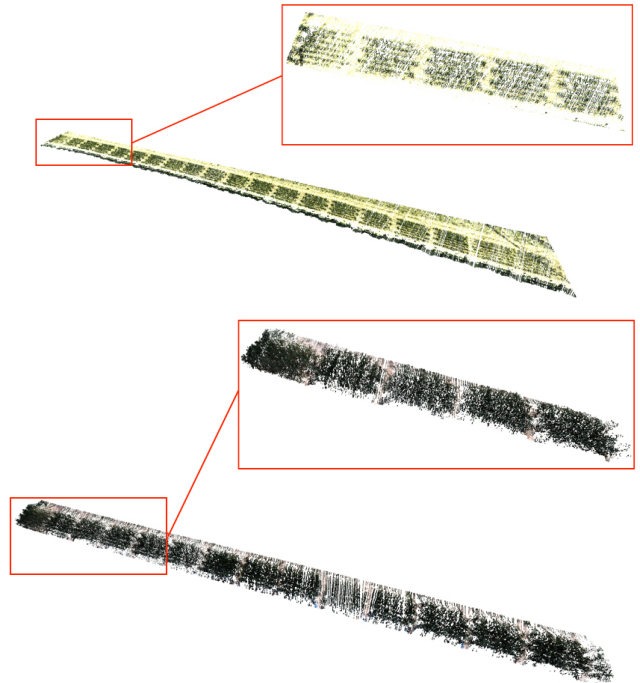


Fig. 3. 3D reconstructions of the winter wheat field on 10-04-2015 (top) and 12-05-2015 (bottom). The plot sizes are 1.5 m x 1 m with different genotypes planted for breeding experiments. One can observe the dramatic variation in the appearance of the crops which presents a challenge for automated segmentation and analysis pipelines.

IV. QUANTIFYING PHENOTYPIC VARIATION ON THE FIELD

There exist well established parameters to characterize the differences between crops growing on the field, such as height, canopy cover, leaf area index (LAI) and chlorophyll fluorescence. We use the point clouds generated using our hand-held platform to estimate the crop height and canopy cover. These estimates, converted into human-readable maps, can be used to assist and verify breeders' rating values for different plots and provide an estimate of the growth rate of plants and its spatial variation.

A. Height Estimation

We use our previously developed height estimation pipeline, described in detail in [17]. An overview is provided here for completeness. The point clouds are first segmented using a color threshold to separate the vegetation from the soil. A linear regression surface is then fitted through all the soil points to get the global orientation of the scene. For height estimation, a finer tessellation of this ground surface is performed and a local multinomial regression surface is fit through the soil points in each region. The ground plane is further subdivided into regions with dimensions approximating the plant size of the crop under study. The height of each plant region is then estimated as the height of the vegetation point corresponding to the 99th percentile within that region.

B. Canopy Cover Estimation

We define canopy cover as the percentage of the ground covered by vegetation when looking down along the normal to the ground plane. We compute it by subdividing the field into small areas, each of which we consider covered by vegetation, if we find at least one plant vertex above them. The canopy cover is then found as the ratio of the sum of all covered areas to the area of the entire field. The challenge now lies in accurately choosing the tessellation size. If chosen too high, large areas would inadvertently be considered covered even if they contained only one point (which might be an outlier from the reconstruction). On the other hand, a leaf can only be represented by a finite number of points which have no volume themselves. Thus, if the tile size is chosen too small the areas between closely neighboring points would not be considered covered even though it is quite likely that the points belong to the same leaf. In the limit, the estimated crop cover would eventually converge towards zero when the tile size approaches zero.

It is therefore reasonable to choose the tile size based on the individual density of each point cloud. For this purpose we compute the distances from all points in the point cloud to their corresponding nearest neighbor. Among all these inter-vertex distances we look for the median. We then subdivide the field into squares and choose their side-length as twice the median found in the previous step. Finally the canopy cover is found as the ratio of the number of squares that have at least one plant vertex above them to the overall number of squares.

V. RESULTS AND DISCUSSION

We collected two datasets on an experimental winter wheat field at Lindau, Eschikon in Switzerland. An overview of the field is shown in Figure 4. The field is used for breeding experiments and consists of $1.5\text{ m} \times 1\text{ m}$ plots with different wheat genotypes. The purpose of such experiments is to determine which of the genotypes are better suited to a certain type of environment or abiotic stress, by measuring and quantifying plant growth over time and comparing the different plots. The datasets were collected on April 10 and May 12, 2015 during the growth period of the plants. Data collection was performed in a nadir configuration, recording images at 20 Hz, range scans at 40 Hz and inertial measurements at 800 Hz. We oriented the sensor suite in a way that optimized coverage for our push-broom approach to reconstruction and walked at normal speed (approximately 1 m/s).

The point clouds for one row of plots for both days are shown in Figure 3. One can clearly observe the large variability in the visual appearance of the crops at different times. This is attributed to the ambient illumination and the change in the physical structure of the plants which has an influence on the shadows and occlusions. The dramatic change was observed to cause issues with automated segmentation procedures and hence the segmentation thresholds had to be set manually. One can observe that the number of soil points reduces dramatically in the second point cloud due to occlusions caused by plant growth. While a limited number of ground points makes it



Fig. 4. Aerial orthomosaic of the research field at Lindau, Eschikon. The red rectangle shows the area where the data was collected.



Fig. 5. Image of the winter wheat plots within the field. The red lines depict the area where the data was collected.

difficult to obtain an accurate reconstruction of the ground profile, there are still enough points for our regression method to generate the height estimates. A height map of 5 selected plots on the field is shown in Figure 6 for the two days. The canopy cover is estimated using the procedure described in section IV-B. Figure 7 shows a top view of the field with squares classified as vegetation depicted in green. Using the point clouds, we seek to simulate traditional imaging-based canopy cover estimation techniques which estimate the canopy cover based on images of the field taken using a camera looking down towards the plots. However, as seen in Figure 7, it is difficult to accurately assess the spatial variation of the canopy cover between different plots using such a binary map with high resolution. In order to support discrimination between the different plots, average canopy cover values over a larger ground area are calculated and depicted in Figure 8. This averaging makes it easy to identify the plots with higher canopy density compared to the others.

From these height and canopy cover maps, one can observe the relative growth of the plants over time in all three dimensions and the variation between the different plots becomes apparent, enabling better decision making while rating different plots or identifying areas of high/low growth within a large farm.

In order to determine the accuracy and reliability of the height estimates, 5 plant heights were measured for each plot using a yardstick on both days. The average height per plot was determined by averaging these plant heights for each plot. These were then compared with the average height per plot

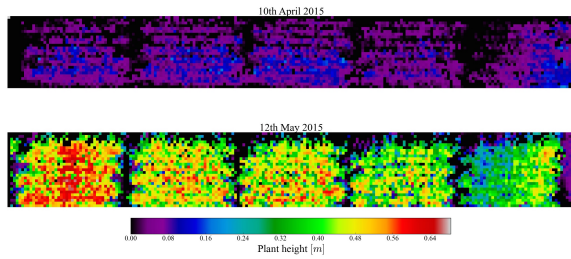


Fig. 6. Height map of a winter wheat field. The plot sizes are 1.5m x 1m and different genotypes are planted for a breeding experiment.

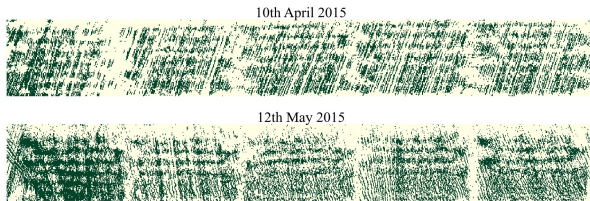


Fig. 7. Image showing a top down view of the winter wheat plot canopy. Green represents pixels covered by plant and yellow the ground. The pixel size is defined adaptively based on the density of the point cloud.

computed by averaging the maximum plant heights in five areas in the reconstruction corresponding to the spatial location of the plants used for the yardstick measurements. The results are shown in Figure 9 in the form of a bar chart with the mean and standard deviation of the yardstick and scanner based height estimates per plot for the 5 plots.

VI. CONCLUSION AND FUTURE WORK

In this work we have proposed using a flexible, hand-held multi-sensor platform for collecting crop data on a winter wheat field. Preliminary results show that the collected data and semi-automated post processing of the point clouds enable the quantification of important phenotypic parameters of the crops. Average crop height and canopy cover are estimated and presented in the form of user readable maps, such as those in Figures 6 and 8, useful for agronomists, farmers and crop scientists.

While our work shows promising preliminary results, it also highlights some limitations. Errors affecting reconstruction and subsequently crop height estimation may arise from inaccuracies in the estimated sensor trajectory and in the range measurements. In the first case, noise on estimating roll and pitch angle as well as drift in the estimated height of the sensor will presumably have the largest effect. Range measurements are corrupted by different deterministic biases [18] as well as random noise. In addition, the laser beam covers a certain solid angle, and depth discontinuities inside this cone yield "mixed pixels", weighted averages of the sampled depths. Since floral environments are rich in discontinuities, we expect a significant amount of these artifacts. For plants with sufficient leaf area, the effect of this is mitigated by taking the 99th percentile, as there is a high probability of acquiring samples that are not

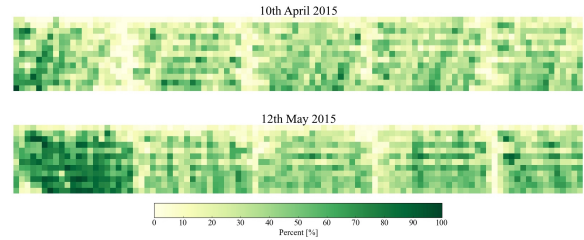


Fig. 8. User readable map for canopy cover density. One can easily observe the relative variation between different plots and their growth over time.

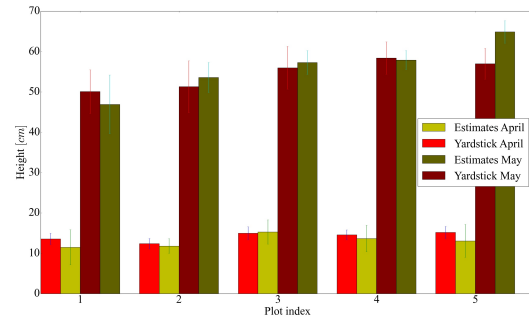


Fig. 9. Comparison of average height per plot using yardstick measurements and our sensor setup for both days.

affected by discontinuities. Improved robustness of the ground plane estimation process to outliers in the segmentation may be obtained by replacing the linear regression by fitting based on a RANSAC scheme [19].

Future work will focus on integrating additional sensors to overcome the challenges mentioned above. Segmentation based on normalized difference vegetation index (NDVI) using a multi-spectral camera could improve the accuracy and robustness of the soil-plant segmentation. The addition of an RTK GPS system can improve the robustness of the localization and prevent drifts, leading to more accurate trajectories and longer operating times with which larger areas may be covered in one cycle.

ACKNOWLEDGMENT

The authors would like to thank Dr. Johannes Pfeifer, Dr. Frank Liebisch and Prof. Dr. Achim Walter at the Chair of Crop Science at ETH Zürich for access to the research fields and valuable discussions.

REFERENCES

- [1] A. Walter, B. Studer, and R. Kölliker, "Advanced phenotyping offers opportunities for improved breeding of forage and turf species," *Annals of botany*, p. mcs026, 2012.
- [2] A. Walter, F. Liebisch, and A. Hund, "Plant phenotyping: from bean weighing to image analysis," *Plant methods*, vol. 11, no. 1, p. 14, 2015.
- [3] J. L. Araus and J. E. Cairns, "Field high-throughput phenotyping: the new crop breeding frontier," *Trends in Plant Science*, vol. 19, no. 1, pp. 52–61, 2014.
- [4] J. M. Montes, A. E. Melchinger, and J. C. Reif, "Novel throughput phenotyping platforms in plant genetic studies," *Trends in plant science*, vol. 12, no. 10, pp. 433–436, 2007.

- [5] L. Busemeyer, D. Mentrup, K. Möller, E. Wunder, K. Alheit, V. Hahn, H. P. Maurer, J. C. Reif, T. Würschum, J. Müller *et al.*, “Breedvisiona multi-sensor platform for non-destructive field-based phenotyping in plant breeding,” *Sensors*, vol. 13, no. 3, pp. 2830–2847, 2013.
- [6] D. Deery, J. Jimenez-Berni, H. Jones, X. Sirault, and R. Furbank, “Proximal remote sensing buggies and potential applications for field-based phenotyping,” *Agronomy*, vol. 4, no. 3, pp. 349–379, 2014.
- [7] G. R. T. C. J. Dong, L. Carlone and F. Dellaert, “4d mapping of fields using autonomous ground and aerial vehicles,” in *CSBE/ASABE Joint Meeting Presentation, 2014*, 2014.
- [8] J. Nikolic, J. Rehder, M. Burri, P. Gohl, S. Leutenegger, P. T. Furgale, and R. Siegwart, “A synchronized visual-inertial sensor system with fpga pre-processing for accurate real-time slam,” in *Robotics and Automation (ICRA), 2014 IEEE International Conference on*. IEEE, 2014, pp. 431–437.
- [9] L. Zhang, Z. Liu, and C. Honghui Xia, “Clock synchronization algorithms for network measurements,” in *INFOCOM 2002. Twenty-First Annual Joint Conference of the IEEE Computer and Communications Societies. Proceedings. IEEE*, vol. 1. IEEE, 2002, pp. 160–169.
- [10] P. Furgale, J. Rehder, and R. Siegwart, “Unified temporal and spatial calibration for multi-sensor systems,” in *Intelligent Robots and Systems (IROS), 2013 IEEE/RSJ International Conference on*. IEEE, 2013, pp. 1280–1286.
- [11] J. Rehder, P. Beardsley, R. Siegwart, and P. Furgale, “Spatio-temporal laser to visual/inertial calibration with applications to hand-held, large scale scanning,” in *Intelligent Robots and Systems (IROS 2014), 2014 IEEE/RSJ International Conference on*. IEEE, 2014, pp. 459–465.
- [12] M. D. Grossberg and S. K. Nayar, “What is the space of camera response functions?” in *Computer Vision and Pattern Recognition, 2003. Proceedings. 2003 IEEE Computer Society Conference on*, vol. 2. IEEE, 2003, pp. II–602.
- [13] D. B. Goldman, “Vignette and exposure calibration and compensation,” *Pattern Analysis and Machine Intelligence, IEEE Transactions on*, vol. 32, no. 12, pp. 2276–2288, 2010.
- [14] S. Leutenegger, S. Lynen, M. Bosse, R. Siegwart, and P. Furgale, “Keyframe-based visual-inertial odometry using nonlinear optimization,” *The International Journal of Robotics Research*, vol. 34, no. 3, pp. 314–334, 2015.
- [15] T. Cieslewski, S. Lynen, M. Dymczyk, S. Magnenat, and R. Siegwart, “Map api - scalable decentralized map building for robots,” in *International Conference on Robotics and Automation*. IEEE, 2015.
- [16] P. E. Debevec and J. Malik, “Recovering high dynamic range radiance maps from photographs,” in *ACM SIGGRAPH 2008 classes*. ACM, 2008, p. 31.
- [17] R. Khanna, M. Möller, J. Pfeifer, F. Liebisch, A. Walter, and R. Siegwart, “Beyond point clouds - 3d mapping and field parameter measurements using uavs,” p. to appear, 2015.
- [18] P. Demski, M. Mikulski, and R. Koterak, “Characterization of hokuyo utm-30lx laser range finder for an autonomous mobile robot,” in *Advanced Technologies for Intelligent Systems of National Border Security*. Springer, 2013, pp. 143–153.
- [19] M. A. Fischler and R. C. Bolles, “Random sample consensus: a paradigm for model fitting with applications to image analysis and automated cartography,” *Communications of the ACM*, vol. 24, no. 6, pp. 381–395, 1981.

Design and Flight Testing of an Integrated Solar Powered UAV and WSN for Greenhouse Gas Monitoring Emissions in Agricultural Farms*

Alexander Jairo Rojas Malaver *CPME*, Luis Felipe Gonzalez *ARCAA*, Nunzio Motta *CPME* and Tommaso Francesco Villa *CPME*, Victor Kwesi Etse *SEF*, Eduard Puig *ARCAA*

Abstract—There is an increased interest in measuring the amount of greenhouse gases produced by farming practices. This paper describes an integrated solar powered Unmanned Air Vehicles (UAV) and Wireless Sensor Network (WSN) gas sensing system for greenhouse gas emissions in agricultural lands. The system uses a generic gas sensing system for CH₄ and CO₂ concentrations using metal oxide (MoX) and non-dispersive infrared sensors, and a new solar cell encapsulation method to power the unmanned aerial system (UAS) as well as a data management platform to store, analyze and share the information with operators and external users. The system was successfully field tested at ground and low altitudes, collecting, storing and transmitting data in real time to a central node for analysis and 3D mapping. The system can be used in a wide range of outdoor applications at a relatively low operational cost. In particular, agricultural environments are increasingly subject to emissions mitigation policies. Accurate measurements of CH₄ and CO₂ with its temporal and spatial variability can provide farm managers key information to plan agricultural practices. A video of the bench and flight test performed can be seen in the following link:

<https://www.youtube.com/watch?v=Bwas7stYIxQ>.

I. INTRODUCTION

Agricultural greenhouse gas emissions can come from several sources; soil management, enteric fermentation, manure management as well as CO₂ from fossil fuel consumption, Agricultural soil management emissions for instance are nitrous oxide emissions which can account for about 55-65% of the total emissions from the agricultural sector. The large increase in the use of nitrogen fertilizer for the production of high nitrogen consuming crops like corn or wheat has increased the emissions of nitrous oxide. The use of nitrogen fertilizer is essential for profitable crop production. Some practices that use nitrogen fertilizer more efficiently have the potential to reduce nitrous oxide emissions while reducing production costs. Additionally reducing nitrogen fertilizer volumes reduces the risk of polluting ground waters. Methane is produced by ruminant animals such as cattle, goats and sheep during the digestive process as a result of a microbial fermentation. Beef cattle for example can account for about 70 percent and dairy cattle for about 25 percent of methane emissions. If beef and dairy cattle numbers increase, methane emissions will also increase [1].

Even though there are several methods used for measuring emissions in farms they have some limitations mainly in being restricted to be at a static location and cost of deploying several measuring stations around a farm also presents some changes in limited available power around a large broad acre farm [2].

This paper discusses the development, integration, and flight testing of a gas sensing system installed on a UAV and a WSN. This methodology represents a new opportunity to measure the spatial and temporal distribution of emissions. By monitoring the variability of agricultural emissions, farm managers can adapt agricultural practices to existing and future emissions mitigation policies. Figure 1 illustrates the concept developed.

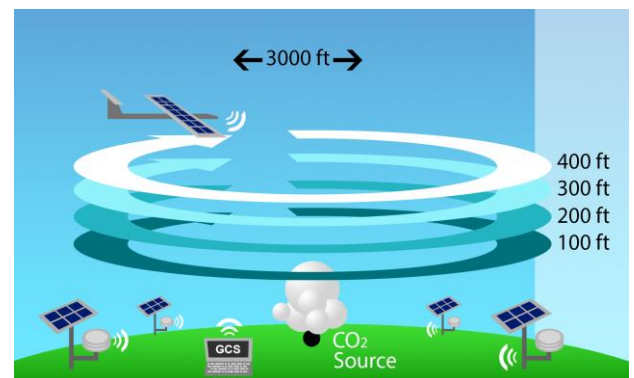


Figure 1 – Concept of a solar powered WSN and UAV gas sensing system.

UAVs have been used as an aerial remote sensing platform to measure environmental gases. UAV technologies are becoming a low cost but powerful tool to reach remote areas and survey relatively large regions [3,4]. In recent years, optical gas sensing devices have been widely integrated into UAV platforms. Watai et al.[5] for instance discussed a non-dispersive infrared (NDIR) sensing system to monitor atmospheric CO₂ concentration onboard a small UAV, and designed an economic and accurate gas sensor system (± 0.26 ppm precision). The system performed several flight tests and achieved one hour flight autonomy with a 3.5 kg payload. McGonigle et al.[6] reported the first measurements of volcanic gases with a helicopter UAV at La Fossa crater, Volcano, Italy using an ultraviolet and infrared spectrometer to

* Queensland Government through the NIRAP project. ARCAA for their technical support.

measure SO₂ and CO₂ gas concentrations. The UAV had 12 minutes of flight autonomy, carrying a 3 kg payload. Astuti et al.[7] developed a UAV for volcanic monitoring on Mt Etna using a fixed wing UAV to carry a CO₂ infrared spectrometer and a SO₂ electrochemical sensor. All these earlier research have achieved to autonomously sense gases using UAVs but the need to design and develop an efficient integrated system to continuously monitor and estimate gas concentrations has not been undertaken. Hence this paper is intended to tackle this issue by combining UAVs and WSN. The rest of the paper is organized as follows: section 2 discusses Solar Powered Wireless Sensor Network (WSN) Subsystem, section 4 describes the solar powered UAV, section 4 discusses WSN and UAV field tests, and section 5 presents conclusions and future work.

II. SOLAR POWERED WIRELESS SENSORS NETWORK (WSN) SUBSYSTEM

Malaver et al described a generic gas sensing system and its application to WSN [8], developed as part of a collaborative research project between Brescia University (Italy) and QUT (Australia). We integrate a CO₂ NDIR sensor also termed as the nano-sensor (CDM30K, Figaro Inc., Osaka, Japan), which is pre-calibrated from factory at 0 and 400 ppm, however the accuracy of the reading were cross checked with a LI-840A CO₂ analyzer showing an overall error in the measurements of 5%. The signal output of the module is a DC voltage between 0 and 4 V, which represents 0–2000 ppm, respectively [9].

In This paper we extend the earlier work by adapting the gas sensor system to be installed on a Solar Powered UAV. The four principal components of the gas sensing system are shown in Figure 2: a network board, a gas sensor and sensor board interface, a humidity sensor, a heat sensor and control and solar panel and power electronics. The network card acquires the signal from the gas sensors and is able to propagate the data throughout multiple wireless sensor nodes in order to reach the base node. The base node communicates the data to the field computer, data of which can be stored, displayed and shared on a live webpage.

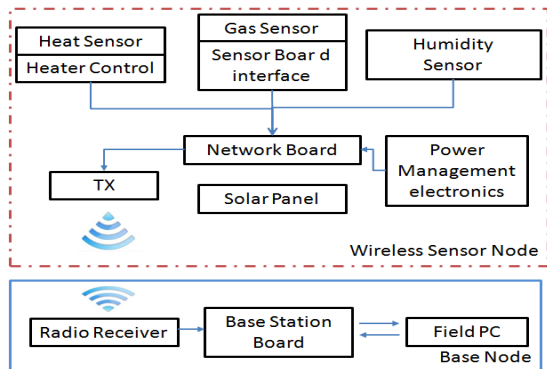


Figure 2 – Wireless gas sensing system node and base node configuration.

III. SOLAR POWERED UAV

The UAV has three main sub-systems that are integrated with the airframe in order to estimate gas concentration, navigate, and keep powered during operations. These sub-systems are depicted in Figure 3.

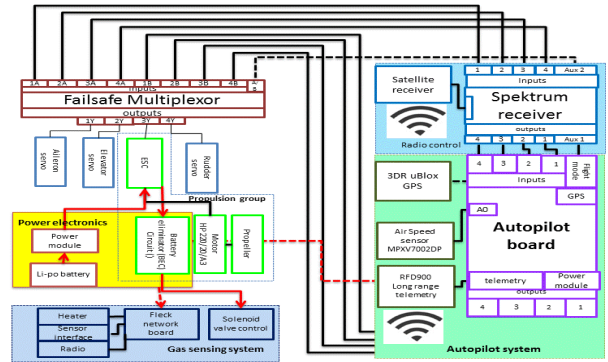


Figure 3 – General configuration of the UAV avionics integrated with the gas sensing system.

A. Gas Sensing System

The same gas sensing technology described in section 2 and used on the WSN was integrated to the UAV platform with some modifications in size, weight and power. Figure 4 illustrates these adaptations. The sample intake was adapted to allow the volume of gas volume for measurements.

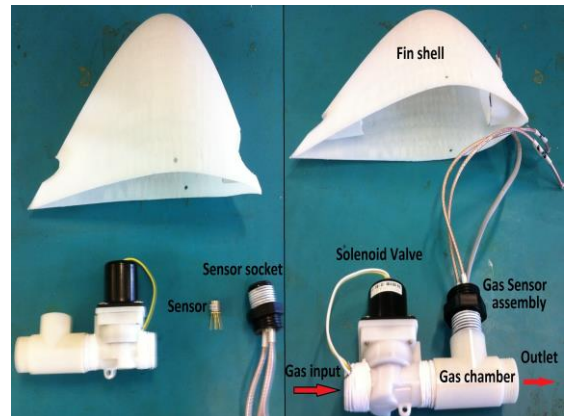


Figure 4 – Airborne gas sensing system: aerodynamic fin shell, gas sensor, sensor socket, gas chamber and solenoid valve.

The power for the gas sensing system is provided by an electronic battery eliminator circuit (BEC) that provides up to 5 VDC, 2 A. The 6 V required by the solenoid valve is provided by a step-up converter circuit attached to the BEC. Once the sensor board acquires the sensor signal, the information is transmitted to the base node using the radio module, antenna of which is installed on the top of the airframe.

B. UAV and Navigation System

The UAS developed in this work was based on the Green Falcon UAV[8,10]. The UAV airframe is easy to transport for fast deployment and hand launch. It has a wingspan of 2.52 m, AR of 13, and fuselage length of 960 mm.

The main component of the navigation system is the autopilot, which is equipped with an air speed sensor, gyro sensor, accelerometer, magnetometer, barometric pressure, GPS, airspeed and fail safe system. The principal goal of this device is to navigate the aircraft by controlling the altitude, speed, and direction. The autopilot used for the UAS was the ArduPilot Mega 2.5, which is a complete open source autopilot system with a high benefit/cost ratio and low weight (23 g). The autopilot system works mainly in three modes: (i) autonomous mode to fully perform unmanned mission by pre-programming waypoints from the ground control station (GCS); (ii) stabilised mode to assist a ground pilot in controlling and stabilising the flight of an aircraft where the pilot has partial control of the aircraft and when there is no pilot input the autopilot will maintain a level flight; (iii) and manual mode, which is useful to perform the pre-flight check as the autopilot acts as a pass-through for all RC commands and also allows the pilot to freely preform manual take-offs, manoeuvres and landings when the autopilot is not pre-programmed to perform these tasks. In all modes, the autopilot is capable of transmitting relevant flight information such as roll, pitch, yaw, airspeed, GPS position and battery status to the GCS by using the telemetry module. The GPS system used was a LEA-6 (UBlox), which consumes low power, is small and lightweight (16.8 g) it has an update rate up to 5 Hz and is ideal for UAV applications. When the GPS is connected to the autopilot the coordinates are transmitted to the GCS using the same telemetry module of the autopilot. The GPS connects directly to the autopilot GPS port, and uses the RX, TX, GND and 5 V connections.

C. Power Management and Solar Wing

The total energy demand of the UAV was calculated based on the power consumption of the avionics, motor and gas sensing system, plus the lost energy caused by the efficiency of electronics and avionics (equation 1).

$$E_{demand_total} = \frac{(E_{avionics} + E_{gas_s})}{\eta_{power\ electronics} \times \eta_{avionics}} \quad (1)$$

Where the efficiency of the power electronics (η_{pe}) is 0.86, and the avionics (η_{av}) is 0.90.

Replacing values in Equation (1):

$$E_{demand_total} = \frac{(42.12\ Wh + 0.8\ Wh)}{0.86 \times 0.9}$$

$$E_{demand_total} = 55.4\ Wh$$

The total energy demand (55.4 Wh) needs to be supplied by the solar wing and the battery. The solar wing was constructed using small silicon solar cell (SSC) ribbons connected in serial and parallel configuration to achieve the voltage and current required. Each SSC ribbon has an area of 0.00375 m² and an average of 12 % efficiency. The maximum area for the solar panels is limited by the wing area (490 cm²), ailerons, narrow ends, and the area allocated for the gas sensor system (53 cm²). Careful analysis of the location and configuration of the solar panels lead to 70 SSC ribbons were distributed along the three parts of the wing by placing 19 units on each side wing (total 38), and 32 units in the middle, for a total of 70 SSC units (0.2625 m²). The weight density of a single SSC ribbon with the tabbing wire installed is 0.53 kg/m². A flexible capsule with the shape of the wing was made to allocate the SSC panels, to avoid losses in aerodynamic performance and to withstand mechanical stress due to in flight vibrations of the UAV. The solar panels were encapsulated using a clear resin, which is flexible and totally transparent to avoid output power losses. Figure 5 shows the UAV with the solar wing in flight.

The internal connections are in serial configuration to obtain the desired voltage of each panel. The side wing panels were connected in series to reach a V_{oc} of 19 V, which produced a current flow of 1.16 A. The middle wing panel is the main section, and consisted of 32 SSC ribbons in serial configuration to produce a V_{oc} of 16 V, and I_{sc} of 1.16 A. The right and the left wing panels in serial configuration were connected in parallel to the middle wing panel to produce a final V_{oc} and I_{sc} value between 16-19 V, 2 A, respectively.



Figure 5 – Green Falcon UAV in flight at Christmas Creek farm.

The total wing weight is 1610 g which means that 650 g is due to the SSC panel and encapsulation mass.

A commercial battery that complements the solar panel to meet the energy demand of the aircraft is a 4 cell, 3.0 Ah lithium polymer battery, which provides a nominal energy output of 44.4 Wh. However, for safety reasons and technical limitations, only 80 % of the battery capacity (35.52 Wh) was

taken into account. The total energy available is therefore 59.14 Wh, which is enough energy to satisfy the demand of 55.4 Wh. The electronic board used to manage the solar and battery power is based on the BQ 24650 EVB from Texas Instruments [11]. The board works as a Maximum Power Point Tracker (MPPT), battery charger, and power path manager. This chip is from the same family as the nodes used for the WSN, with a battery charge/discharge efficiency of 86 %. The system is easy to setup, as the circuit board has only three ports; one for the solar power inlet, one for the lithium battery, and the output power to energise the UAV systems.

D. Some Propulsion System and Total Aircraft System

The main components of the propulsion group of the aircraft are the electronics speed controller (ESC); the brushless motor; and the propeller. The ESC used was the Plush 40 A, which can provide up to 40 A to the motor with a smooth throttle response, integrated battery eliminator circuit (BEC, 5V/3A), small size, weights 33 g, and is compatible with lithium polymer batteries with 2 to 6 cells.

The ESC regulates the power from the battery to run the avionics and gas sensing system simultaneously. In the case of an energy shortage, the ESC cuts the motor off and maintains a minimum power to allow the pilot manoeuvre an emergency landing. The brushless motor used was the Plettenberg HP/220/20/A3 P6 SL 5:1.

The weight distribution of the UAS with the sensing system installed is illustrated in Figure 6 which shows the breakdown for the CO₂ system only, similar results were obtained for the nano-sensor system. The total weight of the UAS with the CO₂ system was 2573 g, and with the nano-sensor system 2615 g. It is clear from Figure 6 that the wing and fuselage were the heaviest parts in the UAV, while the CO₂ gas sensing system or the nano-sensor system represents only 12 % and 14 % of the total weight, respectively.

The power electronics had an average output voltage of 14.2 V, and the current intensity reached its maximum peak of about 6.5 A (consuming about 80 W), during take-off manoeuvres; however the average current consumption fluctuated between 1 A to 3 A (about 15 to 40 W), during regular flight operation.

According to the GCS, the energy consumption of the UAV during the flight operation was in average 25 Wh, which is lower than the average energy measured in the bench test of about 40 Wh. The possible reason for this lower consumption is that the throttle of the motor was more active during the bench test than in the real flight operation, which is a positive feedback for the final design of the solar powered UAV for continuous flight during sun-light hours.

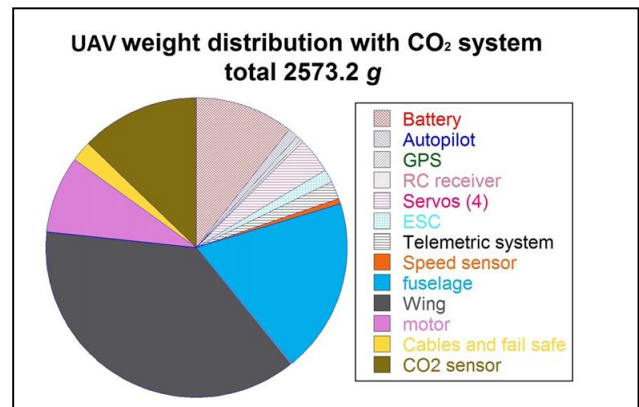


Figure 6 – Weight distribution of the Green Falcon UAV with CO₂ gas sensing system.

IV. WSN AND UAV FIELD TEST

The target gas of the experiments was CO₂ measurements due to the availability of the gas in the field testing area and the possibility of creating a contaminant source. Testing NO₂ and CH₄ in the field requires a different scenario that will be considered in future work. The WSN was calibrated and tested at Samford Ecological Research Facility (SERF) [8] however only two of the four nodes developed for the WSN were tested in conjunction with the UAV as a proof of concept.

The complete system was tested at Christmas Creek, QLD, 23th July, 2013. The base station was located at the beginning of the airstrip, the pollutant source was located 30 m from the GCS, the CO₂ ground node and the weather station was deployed 20 m from the GCS, all south of the base node. The UAV mission was to fly in a circular trajectory up to an altitude of 50 m above ground level over the area monitored, above the sensor node and pollutant source. The CO₂ was released for 6 min at 0.0027 kg/s rate and average wind speed of 1.09 m/s.

CO₂ concentration values taken from ground and aerial nodes during the experiments are plotted in figure 7. The average CO₂ concentration registered by the ground node was 404 ppm during the first 164 s. Then, the average concentration increased slightly until it reached a peak of 442 ppm at the end of the experiment. The average CO₂ concentration registered by the aerial node was 400 ppm, with few CO₂ peaks above the average. The volume monitored by the UAV was 0.0012 km³, based on the circular area travelled and flight altitude (~50 m AGL). The horizontal sampling resolution of the UAV was 88 m/s as the average cruise speed was 12.6 m/s and sampling frequency 7s. Vertical resolution of the samples was 10 m based on the uncertainty of the GPS and autopilot navigation. Figure 8 shows the UAV tracks during the experiment, the contaminant source origin and direction of the dispersion due to wind effect. The average wind speed was 1.5 m/s, mostly in North-east direction.

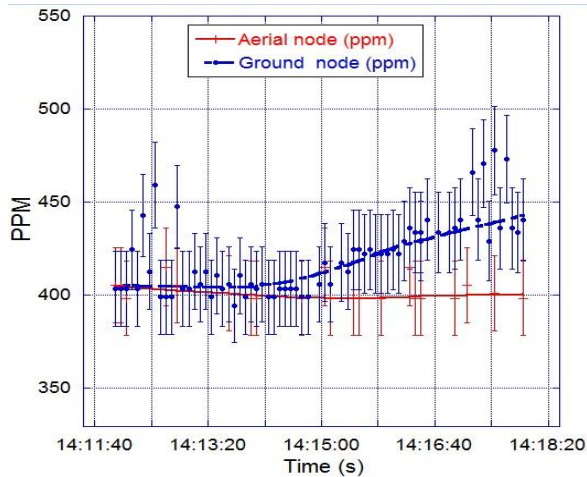


Figure 7 – CO₂ readings from the ground and aerial nodes during the experiment at Christmas Creek, QLD, Australia in 23/07/2013.

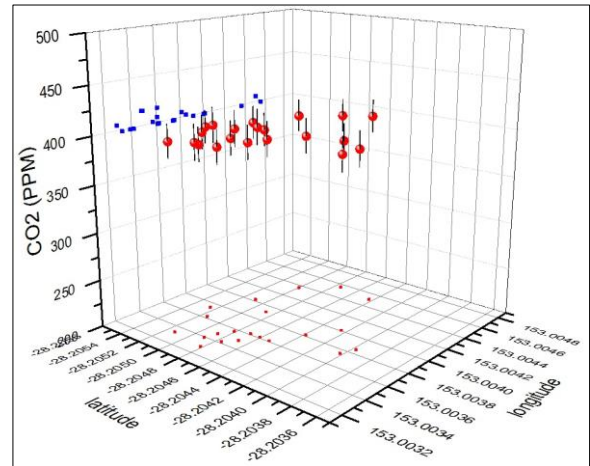


Figure 9 – Readings of the CO₂ gas sensing system on board Green Falcon UAV, showing the latitude, longitude and concentration of each sample.

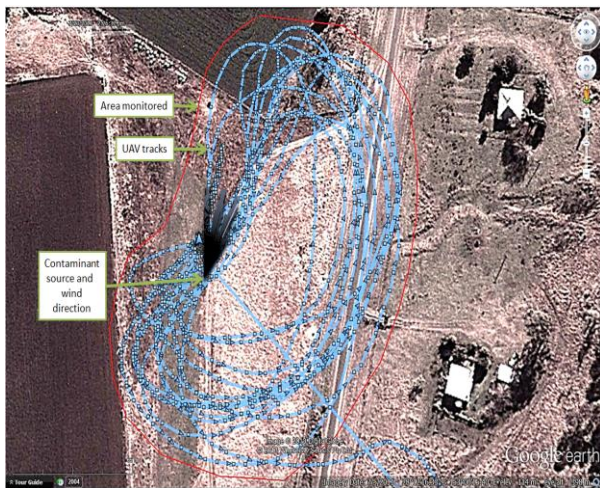


Figure 8 – GPS tracks of the UAV during the mission, the source of contamination and the wind direction.

Figure 9 shows the latitude and longitude coordinates of each sample with its respective CO₂ concentration. The fact that the CO₂ readings from the UAV did not show significant variations indicates that the contaminant release rate and duration were not long enough to affect significantly a volume of 0.0012 km³ within the time span of the experiment (6 min). In addition, the wind strength diluted the pollutant emissions to levels below the sensitivity of the equipment. Geo-location of each sample was achieved by synchronising the logs of the network board and autopilot before the mission started. The ability to geo-locate the sample and register the time allows the reconstruction of the samples in three dimensions and facilitates the visualisation of local concentrations, analysis of their dynamics and correlations with variables such as temperature and pressure.

V. CONCLUSION

This paper described a generic gas sensing and monitoring system of a solar powered WSN and UAV for environmental monitoring. The solar powered UAV was assembled, equipped with the gas sensing system, and successfully tested in the field. It is recommended for further experiments to increase the contaminant rate release and duration to produce significant CO₂ variation in the volume monitored by the UAV. Faster sampling frequency is also desirable, especially when the wind blows in a specific direction, which narrows the detection area.

A video of the extensive bench test performed for this work on the Green Falcon UAV can be seen in the following link <https://www.youtube.com/watch?v=Bwas7stYIxQ>.

VI. ACKNOWLEDGMENT

The authors would like to acknowledge the financial support from the Queensland Government through the NIRAP project, "Solar powered Nano sensors", ARCAA for their technical support, Fazl Alabodi and Mandeep Saini as well as the support from Steven Bulmer the Green Falcon pilot.

REFERENCES

- [1] Takle, Eugene, Hofstrand D., "Global Warming - Agriculture's Impact on Greenhouse Gas Emissions." <http://www.extension.iastate.edu/agdm/homepage.html>. Iowa State University: University Extension, 20 Apr. 2008. Web. 7 June 2015.
- [2] Jaichandran, R., and A. Anthony Irudhayarj. "Prototype system for monitoring and computing greenhouse gases." Carbon 1998 2005.
- [3] Hung, J. Y. and Gonzalez, L. F. On parallel hybrid-electric propulsion system for unmanned aerial vehicles. *Progress in Aerospace Sciences*, 51, pp. 1-17, 2012.

- [4] Gonzalez, F., Castro, M. P. G., Narayan, P., Walker, R., & Zeller, L. (2011). *Development of an autonomous unmanned aerial system to collect time-stamped samples from the atmosphere and localize potential pathogen sources*. *Journal of Field Robotics*, 28(6), 961–976.
- [5] Watai, T. Machida, T. Ishizaki, N. Inoue, G. *A Lightweight Observation System for Atmospheric Carbon Dioxide Concentration Using a Small Unmanned Aerial Vehicle*. *Journal of Atmospheric and Oceanic Technology*, 23(5): p. 700-710, 2005.
- [6] McGonigle, A. J. S. Giudice, G. Tamburello, A. Hodson, J. Gurrieri, S. *Unmanned aerial vehicle measurements of volcanic carbon dioxide fluxes*. *Geophysical Research Letters*, 35(6), 2008.
- [7] Astuti, G. Longo, D. Melita, C.D. Muscato, G. Orlando, A. *HIL tuning of UAV for exploration of risky environments*. *International Journal of Advanced Robotic Systems*, 5(4): p. 419-424, 2008.
- [8] Malaver Rojas, J.A. Motta, N. Gonzalez, L. F. Corke, P. Depari, A. *Towards the development of a gas sensor system for monitoring pollutant gases in the low troposphere using small unmanned aerial vehicles*. *Workshop on Robotics for Environmental Monitoring*, 2012.
- [9] FIGARO. CDM30K Carbon Dioxide Sensor Module. Available online: <http://www.figaro.co.jp/en/topic/2012/01/announcement-of-co2-gas-sensor-module-cdm30k.html> (accessed on 9 September 2014)
- [10] Malaver Rojas, J.A. Motta, N. Corke, P. Bell, J. *Development of a gas nanosensor node powered by solar cells*. In *Solar2011, the 49th AuSES Annual Conference*, Australian Solar Energy Society, 2011.
- [11] *bq24650EVM Synchronous, Switch-Mode, Battery Charge Controller for Solar Power*, T. Instrument, Editor. 2010.

Attentively Finding and Moving Among Apples

Çağatay Odabaşı and H. Işıl Bozma

Abstract—An apple harvesting robot needs to detect apples and visually move among them as to be able process each apple in detail. This is a difficult problem since orchard scenes are generally complicated. This paper proposes a novel approach to this problem based on attentive vision. The robot processes each subimage in an incoming scene attentively in order to find the apples and visually move between candidate apple locations via a family of artificial potential functions where each artificial potential function encodes saliency in a given subimage based on unvisited and visited apple locations. The robot then visually moves from the current apple location to the next via following the closed-loop dynamics of the corresponding gradient vector field. Experimental results demonstrate that - differing from previous work - the proposed approach is robust with respect to specular reflection and background vegetation.

I. INTRODUCTION

One of the integral problems in robotic apple harvesting is finding the fruits and visually moving among them as to process as many of the apples as possible [9]. This is a difficult problem since apples of same orchard or even same tree can differ dramatically in shape or color. Furthermore, the background vegetation may be confusing.

The proposed approaches may be divided into two groups. Those in the first group focus mainly on the color property of apples. In particular, red apples have distinguishable colors; however the reliability of using color is decreased by specular reflection. Approaches in the second group view the problem as an object detection problem and use state-of-the-art object detection algorithms. While these may precisely put bounding boxes around the apples, they are generally computationally expensive. Furthermore, in all of these approaches, the problem of detecting apples is considered separately from that of moving among them efficiently. The visual processing of apple harvester robot must not only enable it to identify the precise location of fruits, but also attend to it covertly as to be able to process each fruit in detail.

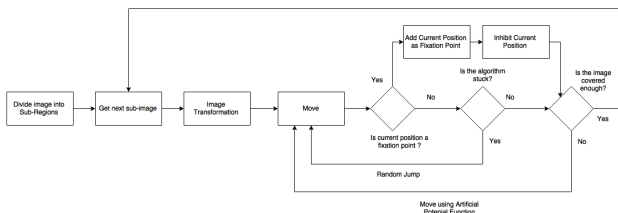


Fig. 1: The flow of processing.

Ç. Odabaşı & H.I. Bozma with the Intelligent Systems Laboratory, Electric Electronic Engineering Department, Boğaziçi University, Istanbul, Turkey {cagatay.odabasi, bozma}@boun.edu.tr

In this paper, we propose a novel approach that addresses both issues simultaneously. We assume a robot equipped with a color camera mounted on a pan-tilt mechanism. In this approach, the robot divides an incoming image into subimages and processes each subimage attentively in order to find the apples and visually move among them. This is achieved via a family of artificial potential functions based on previous work [8]. Each artificial potential function encodes saliency in a given subimage based on unvisited and visited apple locations. The robot then moves its optical axis from the current apple location to the next via following the closed-loop dynamics of the corresponding gradient vector field - in a manner similar to [8]. This is repeated until the scene is sufficiently covered. The advantage of this approach is that as the robot is able to focus on each individual fruit, it sets up a basis for picking them. If the robot actually moves its optical axis, this movement corresponds to overt attention [4]. On the other hand, if its optical axis remains fixed, the corresponding movement is known as covert orienting. Of course, such a system will need to consider the integration of the proposed approach with an arm-gripper mechanism on a mobile robot along with the appropriate range sensing and motion control algorithms.

The outline of the paper is as follows: First, we briefly review the related literature in Section II. Next, we explain the construction of a family of artificial potential functions in Section III. The movement algorithm is then explained in Section IV. Experimental results as presented in Section V demonstrate that the proposed approach enables the robot to find and move among apples with high coverage of the harvest region. The paper concludes with a brief summary and future directions.

II. RELATED LITERATURE

There has been growing interest in robotic fruit harvesting. The proposed approaches are categorized into two groups - namely local based and shape based [1], [10].

In local approaches, image acquisition is followed by pre-processing in order to improve the quality of images followed by segmentation and localization. As such, color has played a major role in the segmentation part. For example, hue and saturation components are used as chrominance information in order to segment the fruits from the background [3], [14]. Some color indices have been applied to segment the image data using a combination of color and texture properties [19]. In [18], color information is used together with depth information. While these approaches enable fruit detection with around 70-90% detection rates in certain scenarios, their robustness is greatly affected by fruit size, proximity, density

and illumination conditions [18]. Furthermore, the robot has to do additional reasoning in order to decide how to move between apples during harvesting.

Alternatively, in shape based approach, the input scene is searched for apples. However this is a highly computational process since most classifiers are generally non-linear. While some algorithms are exact via considering exhaustive search [6], most approaches are inexact as to reduce the complexity [17]. In this perspective, approaches that selectively search have been proposed [16]. These are based on attentive vision which enables agents to react to natural environments like human visual system via constantly directing its optical axis towards most salient areas. As the whole scene need not to be processed with high accuracy, computational efficiency becomes possible. In this framework, saccades swiftly change fixated regions [11], [12], [5], [8]. In this work, we integrate color-based reasoning and attentive processing in order to enable the robot to find apples and move between them.

III. FAMILY OF ARTIFICIAL POTENTIAL FUNCTIONS

Consider the robot's camera with an image plane P . Each artificial potential function $\varphi_k : P \rightarrow [0, 1]$ encodes saliency and inhibition on P during $t \in [t_k, t_{k+1}]$ when the robot moves from one region to the next.

Salient locations are candidate apple locations $\mathcal{C} \subset P$. The set \mathcal{C} can be determined using a variety of visual cues. Here, we consider color as the primary cue. Suppose the color of apples is specified as a given hue H_g . First we define salient regions $\mathcal{X} \subset P$ as:

$$\mathcal{X} = \{x \in P \mid (H(x) - H_g)^2 \leq \tau_h, \quad V(x) \leq \tau_v\}$$

where $H(x)$ and $V(x)$ denote the hue and value associated with the given pixel $x \in P$. They are subjected to a priori specified thresholds τ_h and τ_v respectively. The latter threshold is used to eliminate regions where hue value is not meaningful. Next, connected component analysis is applied on \mathcal{X} followed by opening to find a set of components $\{\mathcal{C}_i\}_{i=1}^{N_c}$. The respective centroids μ_i are used to define \mathcal{C} as:

$$\mathcal{C} = \left\{ \mu_i \in \mathcal{X} \mid \mu_i = \frac{1}{|C_i|} \sum_{x \in C_i} x, \quad i = 1, \dots, N_c \right\}$$

The weight $a(\mu_i)$ associated with each component $\mu_i \in \mathcal{C}$ is defined based on the size of the respective component C_i as:

$$a(\mu_i) = |C_i|$$

Next, inhibition is considered based on visited apple locations \mathcal{V}_k as:

$$\mathcal{V}_k = \{\mu(l) \mid 0 \leq l < k\}$$

Each artificial potential function is defined based on \mathcal{C} and \mathcal{V}_k as:

$$\varphi_k(x) = \sum_{\mu \in \mathcal{C} - \mathcal{V}_k} a(\mu) e^{\frac{1}{2\sigma^2} (x-\mu)^T (x-\mu)} \quad (1)$$

Initially, $\mathcal{V}_0 = \emptyset$, because there are no visited apple locations. The construction of each artificial potential function is such

that it is minimal at the candidate apple locations. This is preferred over being maximal since the flow field properties of gradient systems dictate that maximal points are unstable equilibrium points which means under little perturbations the system starts moving away from these points.

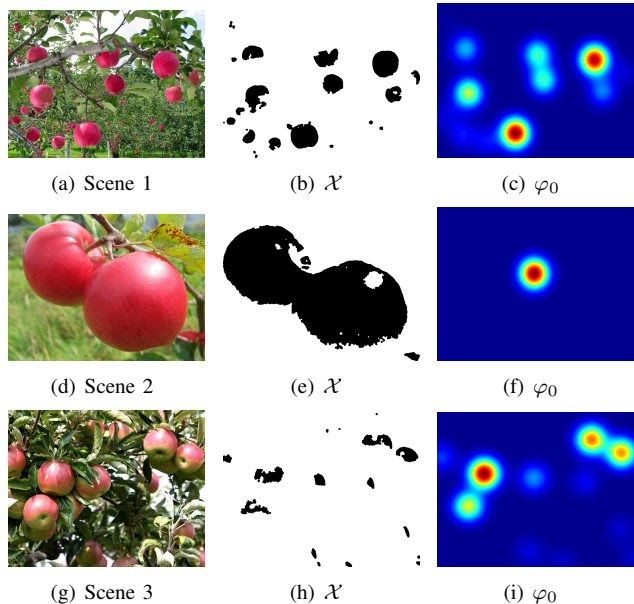


Fig. 2: Saliency via artificial potential function.

Three varying scenes are considered in Fig. 2. The first considers a typical scene as seen in Fig. 2(a). Salient regions \mathcal{X} are shown in Fig. 2(b) with the corresponding φ_0 given in Fig. 2(c). As such, most of the apples are covered. In a second scene of two big apples as seen in Fig. 2(d), as one occludes the other, there is only one salient region as encoded by the corresponding φ_0 as seen in Fig. 2(f). In Scene 3 of Fig. 2(g), some apples are badly illuminated. As such, there are missing salient locations as seen in Fig. 2(i).

IV. MOVING BETWEEN APPLES

While the robot is engaged in harvesting, its camera moves from one apple location $x_k \in \mathcal{C}$ to the next $x_{k+1} \in \mathcal{C}$. The system dynamics is defined based on the negative gradient field of φ_k as:

$$\dot{x}(t) = -D_x \varphi_k(x) \quad (2)$$

starting at initial point

$$x(0) = x_k \quad (3)$$

The camera motion is accomplished simply by “sliding” into the equilibrium point of the associated dynamical system:

$$D_x \varphi_k(x) = 0 \quad (4)$$

The equilibrium point is then designated as the next apple location x_{k+1} . Note that the termination time t_{k+1} is defined implicitly by the time taken to reach to x_{k+1} . This closed loop system inherits the critical qualitative behavior of gradient trajectories.

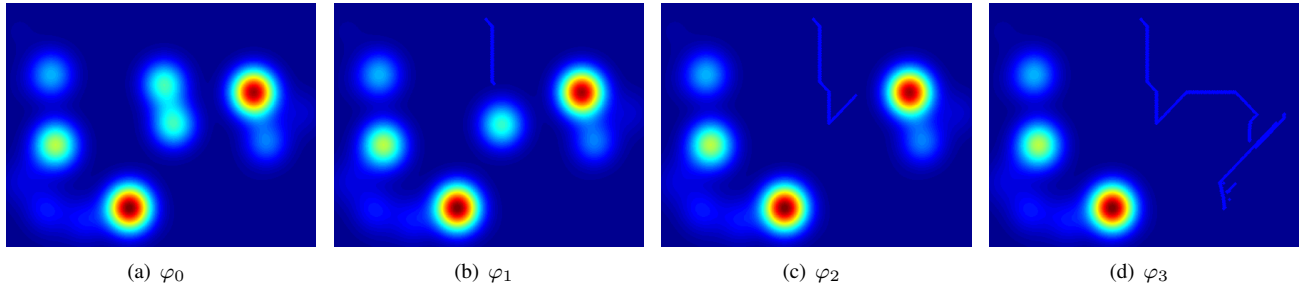


Fig. 3: Sample evolution of φ_k , $k = 0, 1, 2, 3$ as the robot moves between different apples.

The robot’s visual behavior during harvesting is generated via the sequential composition of camera movements. Each visited location x_k gets added to \mathcal{V}_k where $N_v \leq N_c$ denotes the number of apple locations that have been visited. Once one movement terminates, the robot switches to the controller induced by the artificial potential function φ_{k+1} associated with the new apple location x_{k+1} and the movement process is repeated. For a sample image as given in Fig. 2(a), the first couple of φ_k , $k = 0, 1, 2, 2$ are as shown in Fig. 3(a)-3(c) respectively. The scanpath trajectory $x : [t_0, t_{N_v}] \rightarrow P$ is given by the concatenation of the state maps x for each interval $[t_k, t_{k+1}]$ as defined by Eq. 2. The corresponding trajectory may look jagged and even become non-differentiable at times.

V. EXPERIMENTAL RESULTS

We conduct experiments with a wide range of images of red apple orchards and trees as obtained from ImageNet dataset[7] and varying in the proximity and the number of apples as well as illumination conditions. We consider 4 equally sized subregions in each of the test images.

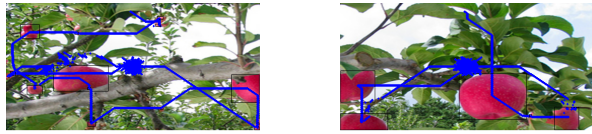
Our results for four different scenes are given in Fig. 4. Each sub-figure (4(a), 4(b), 4(c), 4(d)) presents an apple orchard scene which are selected to cover a variety of scenarios for an apple harvester robot. The first scene Fig. 4(a) contains both close and far range apples where most are visible without any occlusion of leaves, branches or other apples. It is observed that the proposed algorithm is able to cover most of the apples. Some of the further away apples are eliminated by the morphological operations - such as those in the bottom-right sub-image of Fig. 4(a). However, this is actually desirable as these apples are too far to be picked by an harvester robot in practical applications. As such, the resulting path goes from larger apples to smaller apples which suggests that larger and thereby closer apples will be picked up first. Fig. 4(b) contains a scene of apples from medium range under bright illumination. This scene is more complicated as compared to the first as there are many apples that are partly occluded by leaves or other apples. As expected, leaves or branches divide an apple into several parts. Thus, a single apple may be seen as multiple apples. Again, the resulting path goes through the majority of apples in scene in spite of the confusing background. The scene in Fig. 4(c) contains a high number of apples whose count is

difficult even for human. Some of the apples in the bottom-left sub-image of Fig. 4(c) are not detected since they are in the shadows and are relatively darker than other apples. Another observation is the occlusion by other apples due to the huge number of apples in scene so that a group may be counted as one. Even so, the picking path covers nearly all apples in scene in spite of bright illumination. When apples are visually clear as in Fig. 4(d), nearly all of apples are visited. It is observed that occlusion by leaves or branches also poses problems in close-up scenes since different parts of apples may be counted separately such as seen in bottom-left sub-image of Fig. 4(d). However, in practical applications, this may not be a problem since once such apples are picked, the artificial potential function will be updated accordingly.

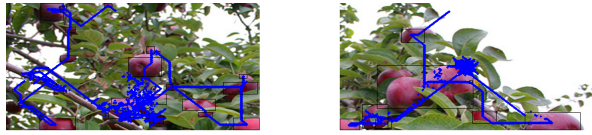
A simple analysis of coverage performance with respect to the number of apples as counted by a human is presented in Table I. In the human count, just too small or too far apples are not taken into account, because counting them won’t give us a practical result. It is observed that the coverage percentage varies between 54-75% with the two scenes while this number goes up to 153-200% with the remaining two in scenes of Fig. 4(b) and Fig. 4(d). This situation is due to counting some of the fruits multiple times since they appear as multiple components due to the illumination difference on their surfaces. In practical applications, this is less likely to be problematic since the location of apples that are picked up are completely inhibited. In the literature, apple coverage rates are cited to be between 70% and 90% [13]. For example, assuming that apples have diameters between 6 - 11 cm, a coverage rate of 80% is reported in [2]. A rate of 93.04% is achieved in laboratory environment [15]. As such, our results are comparable with the state-of-the art approaches with respect to the coverage of apples. Furthermore, the robot is automatically guided from one apple to the next.

TABLE I: Visited apple locations N_v vs number of apples N_a .

	N_v	N_a
Image (a)	51	95
Image (b)	61	40
Image (c)	98	130
Image (d)	28	14



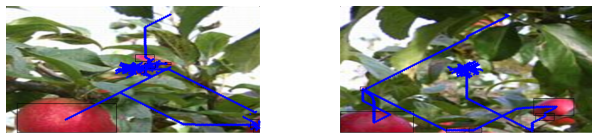
(a) Apples with close and far range.



(b) Apples from medium range under bright illumination



(c) High volume apples from medium range under bright illumination



(d) Apples from close-up

Fig. 4: Apple picking paths.

VI. CONCLUSION

Detecting apples or other fruits in an orchard is integral to fruit harvester robots. However, the detection problem is difficult since fruits can vary in size and color in same orchard or even same tree. Furthermore, the harvester robot must not only locate the fruit, but also visually move between them as to process as many fruit as possible in detail. This paper proposes a novel approach that addresses both issues simultaneously. The robot processes each subimage in an

incoming scene attentively in order to find the apples and visually move between candidate apple locations. This is achieved via a family of artificial potential functions where each artificial potential function encodes saliency in a given subimage based on unvisited and visited apple locations. The robot then visually moves from the current apple location to the next via following the closed-loop dynamics of the corresponding gradient vector field. This is repeated until enough image coverage is achieved. Experimental results demonstrate that the robot is able to covertly move its visual system so that it covers a high percentage of apples - regardless of the proximity of the scene, density of apples and illumination. Thus, as the robot is able to focus on each individual fruit, the proposed approach sets up a basis for picking them. We are currently working on improving the robustness of the proposed approach via addressing problems that arise due to occlusion and varying illumination. However, both are difficult problems in machine vision in general. In future work, we plan to implement the proposed approach on an attentive robot in order to assess real-time applicability. The attentive robot will use closed loop dynamics in order to overtly orient its visual system on many apples as possible. Our ultimate goal is to develop a complete automated picking system on a mobile robot equipped with an arm-gripper mechanism where the proposed approach will be integrated with the appropriate range sensing and motion control algorithms.

ACKNOWLEDGMENT

This work has been supported in part by Bogazici University BAP Project # 9164. We thank Mahmut Demir for insightful discussions on machine vision.

REFERENCES

- [1] R. Ceres A.R. Jimenez and J.L. Pons. A survey of computer vision methods for locating fruit on trees. *Transaction of the ASAE*, 43(6):1911–1920, 2000.
- [2] Johan Baeten, Kevin Donné, Sven Boedrij, Wim Beckers, and Eric Claesen. Autonomous fruit picking machine: A robotic apple harvester. In *Field and Service Robotics*, pages 531–539. Springer, 2008.
- [3] Slaughter David C and Harrell Roy C. Color vision in robotic fruit harvesting. *American Society of Agricultural Engineers*, 30(4):1144–1148, 1987.
- [4] M. Carrasco. Visual attention: the past 25 years. *Vision Res.*, 51(13):1484–525, 2011.
- [5] Henrik I Christensen and Kevin Bowyer. *Active Robot Vision: camera heads, model based navigation and reactive control*, volume 6. World Scientific, 1993.
- [6] Navneet Dalal and Bill Triggs. Histograms of oriented gradients for human detection. In Cordelia Schmid, Stefano Soatto, and Carlo Tomasi, editors, *International Conference on Computer Vision & Pattern Recognition*, volume 2, pages 886–893, INRIA Rhône-Alpes, ZIRST-655, av. de l’Europe, Montbonnot-38334, June 2005.
- [7] J. Deng, W. Dong, R. Socher, L.-J. Li, K. Li, and L. Fei-Fei. ImageNet: A Large-Scale Hierarchical Image Database. In *CVPR09*, 2009.
- [8] Özgür Ercent and H Işıl Bozma. Artificial potential functions based camera movements and visual behaviors in attentive robots. *Autonomous Robots*, 32(1):15–34, 2012.
- [9] Keren Kapach, Ehud Barnea, Rotem Mairon, Yael Edan, and Ohad Ben-Shahar. Computer vision for fruit harvesting robots – state of the art and challenges ahead. *Int. J. Comput. Vision Robot.*, 3(1/2):4–34, 2012.

- [10] Jang-Yoon Kim, M. Vogl, and Shin-Dug Kim. A code based fruit recognition method via image conversion using multiple features. In *IT Convergence and Security (ICITCS), 2014 International Conference on*, pages 1–4, 2014.
- [11] Eileen Kowler. Eye movements. *Visual cognition*, 2:215–265, 1995.
- [12] R John Leigh and David S Zee. *The neurology of eye movements*. Oxford University Press, 1999.
- [13] Peilin Li, Sang-heon Lee, and Hung-Yao Hsu. Review on fruit harvesting method for potential use of automatic fruit harvesting systems. *Procedia Engineering*, 23:351–366, 2011.
- [14] Jidong Lv, De An Zhao, Wei Ji, Yu Chen, and Huiliang Shen. Design and research on vision system of apple harvesting robot. *Proceedings - 2011 3rd International Conference on Intelligent Human-Machine Systems and Cybernetics, IHMSC 2011*, 1:177–180, 2011.
- [15] Amy L Tabb, Donald L Peterson, and Johnny Park. Segmentation of apple fruit from video via background modeling. In *ASABE*, 2006.
- [16] K. E. A. van de Sande, J. R. R. Uijlings, T. Gevers, and A. W. M. Smeulders. Segmentation as selective search for object recognition. In *IEEE International Conference on Computer Vision*, 2011.
- [17] Paul Viola and Michael J. Jones. Robust real-time face detection. *Int. J. Comput. Vision*, 57(2):137–154, May 2004.
- [18] Lv Xiao-Lian, Lv Xiao-Rong, and Lu Bing-Fu. Identification and location of picking tomatoes based on machine vision. *Proceedings - 4th International Conference on Intelligent Computation Technology and Automation, ICICTA 2011*, 2:101–107, 2011.
- [19] Jun Zhao, Joel Tow, and Jayantha Katupitiya. On-tree fruit recognition using texture properties and color data. In *Intelligent Robots and Systems, 2005.(2005). 2005 IEEE/RSJ International Conference on*, pages 263–268. IEEE, 2005.

Robotic mowing of agricultural grass fields with spatial variability using adaptive cruise control system

Timo Oksanen

Abstract— In agriculture, mowing operation is used to cut the grass before collecting for feed or non-food purposes. Mowers cut the grass and the grass is left on the field for wilting, to decrease the moisture content before collection. In this study, a drum type mower was used, which cuts the grass on knife impact without counter shears and therefore the velocity of blades needs to be high, up to 80 m/s. The required power to drive the drums depends on the driving speed. On the other hand, the grass fields are not homogenous, so higher speeds may be used in the areas of light grass density and vice versa. In this study, the autonomous tractor was equipped with an agricultural size mower. The system requires various subsystems to be autonomous and durable. The subsystem discussed in this paper is adaptive cruise control for an autonomous mower, to maximize operational efficiency with constrained power available. The system utilizes a mechanical torque sensing of the power train and coupled with the dynamics of the vehicle, an automatic control system was developed.

I. INTRODUCTION

In agricultural operations, autonomous and semiautonomous machines are considered becoming common in the near future. Currently, the fields are considered partially open structure, even if the boundaries of the field plot are known in global coordinate system, the conditions are changing year to year and operation to operation. Another challenge is that the field plots are not usually bounded by fences that guarantee keeping human beings or large wildlife off the field. Therefore, robotics in arable farming is still under development.

Agricultural fields are not only used for crop production, but also for energy production. In this study, the focus is in harvesting grass from the areas that are not suitable for crop farming, to be used for bio gas production. Lightweight robotic vehicles enable utilizing such land areas that are not otherwise suitable for production, like wetlands.

The main function of an autonomous mower is the mowing system itself. The mower has two tasks: cut the plant and transport it to form a windrow, for wilting. Mowers cut the grass, either by using knives with or without countershear. In this study, we use a mower without countershear and in that type of mower the cutting is based on impact, so the velocity of blade tip needs to be high, up to 80 m/s. Both drum mowers and disc mowers cut the plant with the same principle. [1]

T. Oksanen is University Lecturer at Aalto University, Dept. of Electrical Engineering and Automation, Espoo, Finland. phone: +358947001, email: timo.oksanen@aalto.fi

The basic shape of power consumption of a drum mower depends on power losses which is constant and on the forward speed of the mower which increases power consumption linearly. The power loss can be divided into two parts, for a tip speed related factor and a constant describing the internal friction. However, it is not necessary to split the power loss as long as the angular speed is constant in mowing. [2]

To control the driving speed based on biomass density, two approaches to sensing can be used: direct or indirect measurement. The direct measurement requires a mechanical torque sensor and thus it is possible to create a feedback control system for regulation. The indirect measurement could be based on other sensors measuring the biomass, like pendulum-meter [3] or grass weight measurement in mower-conditioner [4]. In indirect measurement, the control principle has to be feed-forward; or estimation methods are required to estimate the power.

The function in a vehicle regulating the speed is commonly called the cruise control system, or auto-cruise. These are common not only in passenger cars, but also in modern tractors [5]. Automotive industry has used a term adaptive cruise control (ACC) for any system that has some ability to adjust the speed, not only regulate to fixed level. For instance, a system that is using a sensor to detect the distance to the car in front and keeping the distance fixed is an example of ACC.

In this paper, we use direct measurement to regulate the mowing power in the drum type mower. An adaptive cruise control system for a mower is presented. The objective of the system is to regulate the power used by the mower by adapting the forward speed of the autonomous tractor.

The main motivation to regulate the power of the mower by controlling the driving speed is to prevent the continuous overloading of the mower parts and to maximize the operational efficiency with the set constraint. For autonomous usage, the durability of the system is crucial for continuous operation, as there is no human being to replace the parts.

II. MATERIALS

The autonomous tractor is a prototype, originally built in 1990's and completely refurbished and modernized in the years 2009-2013. The tractor is powered with a diesel engine and the power train is hydrostatic. The tractor weighs 5800 kg and standard agricultural implements may be attached to three point hitch with category 2. The tractor

provides power for the implements with 540 RPM power take-off (PTO) and auxiliary hydraulic valves.

The mower used in the study was JF 265 F (model 2013) manufactured by Kongskilde Industries A/S. The mower was connected to the tractor with three point hitch and 540 RPM type 1 PTO shaft. The measured working width of the mower as 2.62 m. The mower consists of four drums, three blades / knives attached to each of them, for impact cutting. The internal drive train of the mower contains three gearings: 13:23 angular gear, 25:34 belt drive and 17:23 rotor gearbox on top of drums. With the nominal PTO speed, the peripheral velocity of blades is 60 m/s. The system is presented in Fig. 1.



Figure 1. The autonomous tractor and the mower

The tractor is equipped with four wheel steering and the maximum steering angle is 17 degrees. The wheelbase is 2.7 m, which leads into the minimum turning radius of 4.4 m. The internal speed control of the vehicle limits the acceleration to 1.0 m/s^2 electronically, to prevent failures. Fig. 2. presents the velocity response of the vehicle, with the stepwise input signal which is filtered to 1.0 m/s^2 rate. The figure shows that the response follows the trajectory well, but a clear time delay is identified. The identified transfer function to explain the dynamics is presented in (1).

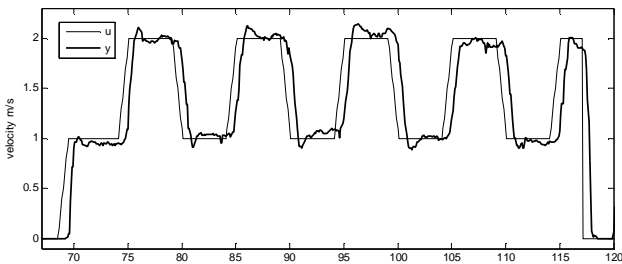


Figure 2. Velocity control of the tractor.

$$v(s) = \frac{1}{0.045s^2 + 0.32s + 1} e^{-0.3s} \quad (1)$$

III. MEASUREMENT

The mower is powered with PTO shaft. A torque sensor was installed on PTO drive shaft, to measure the maximum torque of 1800 Nm at 100 Hz (Datum 420-series with RS-

232 interface). The sensor also transmits the angular speed of the shaft, or RPM.

The speed of the tractor is measured both in the wheels of the tractor, by using encoders. However, the encoders have some mechanical backlash [6], which causes error while changing the direction of travel. In one way driving, the backlash is closed on the other side constantly.

The other measurement, for speed, is based on RTK-GPS receiver with the virtual base station. The speed of GPS antenna measures the course of the tractor, so it is not the true forward speed of the mower when the steering angles are non-zero. On the other hand, GPS speed is on average the true speed, but contains shorter term noise compared with the encoders.

To fuse the encoder and GPS speeds, a full Kalman filter was done, to fuse both the wheel encoders with the steering angles of each wheel, to GPS speed and course and also GPS position signals. The extended Kalman filter also estimates the longitudinal wheel slip, but with the mower the slip is relatively small. Fig. 3. shows a snapshot of measurements and the estimated (fused) speed.

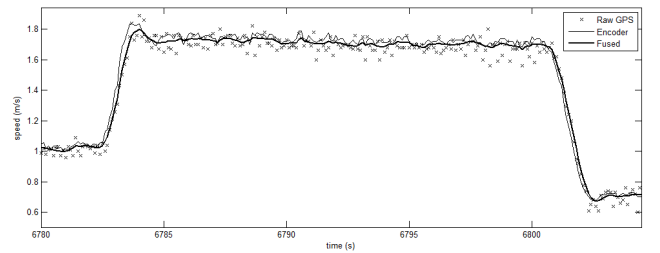


Figure 3. Example of fused signal with Kalman filter.

IV. CONTROL DESIGN

The control design is feedback-feedforward.

The model for the needed for the feedforward part was derived in the tests of the first test plot. The test was carried out autonomously, by using pseudo-random step-wise input for the forward speed and the by measuring the power consumption of the mower, in PTO shaft. The measurements are presented in Fig. 4, showing the linear trend as expected by the model presented in [2]. The linear function identified by using robust regression is presented in (2), the unit of v_f is m/s and the unit of P is kW.

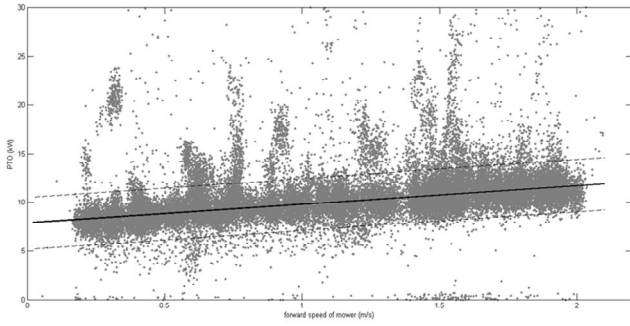


Figure 4. Example of fused signal with Kalman filter.

$$P(v_f) = 7.8 + 1.94v_f \quad (2)$$

Thus, the inverse function of (2) is utilized in the feedforward part.

Due to the maximum acceleration of the tractor drive, or rate limited speed control reference signal, it was decided to use the differential form of PID controller in the feedback. That form supports better the differential constraint of the reference signal to the speed controller of the vehicle. The feedback controller incorporates the saturation of the output, with the anti-windup function.

The overall design architecture is presented in Fig. 5. r_p indicates the reference power for the mower, y_p is the measured power and u_v is the control signal to the vehicle, for the setpoint of velocity. The feedback controller is type P. The driving speed is constrained to range 0.8 to 2.2 m/s externally, to prevent the vehicle from stopping in case of a small blockage and on the other hand the maximum speed for navigation is 2.2 m/s.

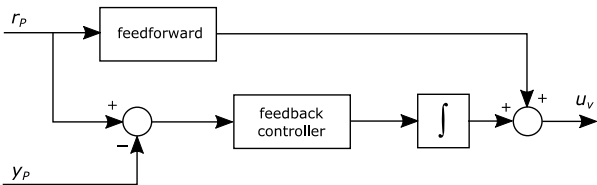


Figure 5. The control design architecture.

V. RESULTS

The control system was tested in the test plot, with light grass. The test plot was prepared by removing the grass in the middle of test swaths, to create a stepwise pattern to the field to mimic maximal variation. The width of the step was 27.6 m and before and after the natural variation of the grass field appeared.

During the test, the autonomous mode of the tractor was used. The guidance system is able to navigate with accuracy of ± 10 cm [7]. In the test, the swath width was set to 2.5 m, which results in 12 cm overlap. However, in each swath the mowed width was 2.5 m, except in the first one.

Fig. 6. presents the control result of a single swath. On the top, the true driving speed is presented, the dashed lines show the constraints. On the bottom, the measured power for the mower is presented. The intentionally created step is in the range from 1296 to 1311 s. During that period, the control system accelerates and reaches the maximum speed and after decreases the speed back to the level before. At the end of the swath the natural variation and previous tests in the field cause acceleration. Fig. 7. illustrates the setup where the autonomous tractor is approaching the step, approximate at time 1290 s.

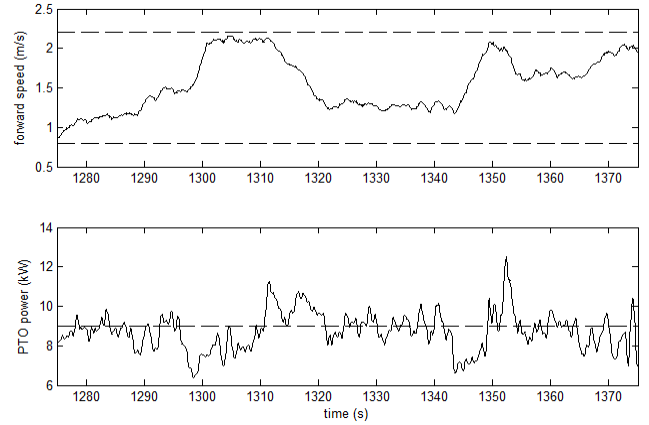


Figure 6. The control response.



Figure 7. The autonomous tractor-mower is approaching the the cleaned area in the test plot.

VI. CONCLUSIONS

For the type of mower used, it is necessary to regulate the tractor speed to reduce the stress on the mower when mowing dense grass. An experimental adaptive cruise control system for the autonomous mower tractor was developed and tested in the field. It was found that the power consumption response to the forward speed follows the textbook pattern and the parameters for the model were found in the test plot. For the system with rate limitation, a control design with the differential form of PID controller with feedforward was utilized.

ACKNOWLEDGMENT

The author acknowledges funding for the research from ICT-AGRI GrassBots project. The research was supported by MTT Agrifood Research Finland, during years 2013-2014 by giving permission to use their facilities including equipment and test fields in Vihti. The author acknowledges especially support by Mr. Antti Suokannas and Mr. Raimo Linkolehto. GrassBots project partner Kongskilde supported the research with the mower and the sensor. The author wants to thank especially Dr. Ole Green, Mr. Thomas Schmidt and Mr. Ole Skau for the support.

REFERENCES

- [1] A.K. Srivastava, C.E. Goering, R.P. Rohrbach & R. Buckmaster, *Engineering Principles of Agricultural Machines, 2nd Edition*. American Society of Agricultural Engineers, St. Joseph, MI, USA. 2006.
- [2] S. Persson, *Mechanics of cutting plant material*. American Society of Agricultural Engineers. 1987.
- [3] D. Ehlert, V. Hammen & R. Adamek, "On-line Sensor Pendulum-Meter for Determination of Plant Mass". *Precision Agriculture*, 4, 139–148.
- [4] F. Kumhala, M. Kroulik & V. Prosek, "Development and evaluation of forage yield measure sensors in a moving-conditioning machine". *Computers and Electronics in Agriculture*, 58(2), 154–163. 2007.
- [5] C. Foster, R. Strosser, J. Peters & J.Q. Sun, "Automatic velocity control of a self-propelled windrower". *Computers and Electronics in Agriculture*, 47, 41–58. 2005.
- [6] T. Oksanen, "Modeling and control of hydraulic drivetrain in agricultural tractor with Position backlash in speed sensor feedback", in *Proc. of IFAC Workshop on Dynamics and Control in Agriculture and Food Processing (DYCAF2012)*, Plovdiv, Bulgaria, 2012. pp. 13–17.
- [7] T. Oksanen, "Accuracy and performance experiences of four wheel steered autonomous agricultural tractor in sowing operation", in *Field and Service Robotics, Results of the 9th International Conference*, Springer. 2013. pp. 425–438.

Object segmentation in poultry housings using spectral reflectivity*

Bastiaan A. Vroegindeweij, Steven van Hell, Joris IJsselmuiden and Eldert J. van Henten, *Member, IEEE*

Abstract— We present a simple and robust method for pixel segmentation based on spectral reflectance properties. Of four object categories that are relevant for PoultryBot, a mobile robot for poultry housings, the spectral reflectance was measured at wavelengths between 400 and 1000 nm. From this information, the distribution of reflectance values was determined for each combination of object category and wavelength band measured. From this, the wavelength band could be selected where the overlap between objects was lowest. This was found to be around 467 nm, with 16% overlap for chickens vs. eggs, 12% overlap for housing vs. litter, and lower overlap for other combinations. Images were taken with a standard monochrome camera and a band pass filter around 470 nm in a commercial poultry house, to test segmentation using this method. Preliminary results indicate that this method is a promising direction for future work.

I. INTRODUCTION

A. Background

In current poultry production systems in western Europe, but also in increasing amounts in other parts of the world, laying hens have freedom to move around. Compared to cage housing, this requires more advanced management, and more manual labour under unfavourable conditions, for example for the collection of floor eggs [1, 2]. In previous work, a poultry house robot (*PoultryBot*) was introduced that should assist in such tasks. For this robot, localisation and path planning methods were presented and evaluated in [3, 4]. In order to allow autonomous function of such robot, it should also be aware of which objects surround it. In this work, we explore the possibility of using spectral information for this task, by analysing the spectral features of objects that are common in poultry houses. Environmental conditions in a poultry house are described in [1, 4, 5]. With respect to the application of vision methods, the low amounts of light (around 5 to 20 lux), in combination with a crowded environment are the most problematic. When functioning inside a poultry house, four main object categories are of relevance for PoultryBot: 1) eggs, being target objects that have to be collected, 2) chickens, being moving obstacles that can be ignored while driving, because they move away from the robot themselves, 3) housing, being static obstacles that should be avoided, like metal poles and walls, and 4) litter, covering the floor area and indicating the driveable surface.

B. Object detection

For the detection of objects around a mobile robot, various methods exist, such as tactile feedback and distance sensors. Most methods however, rely on vision systems as

they can provide much more information on what kind of obstacle is observed. Main disadvantage of vision sensors is that sophisticated processing is required to come up with correct and reliable results under varying conditions. This not only relates to computation time, but involves also more complex algorithms, which might still suffer from variation in objects and environment. In the computer vision domain, much work is done on improving the methods used, by evaluating them on standard sets of images. Common methods make use of color, texture, shape or SIFT/SURF, combined with classifiers like support vector machines or neural networks to locate and classify features or objects. More information can be found in [6], while [7] is one of many examples present. Another variety of vision methods takes advantage of spectral information on objects. In agriculture, this method has been applied for example to distinguish between various kinds of green plants [8, 9]. Van Henten et al. [10] used a known difference between the spectral reflectance of cucumbers and leaves to distinguish these two object types in cucumber harvesting. In egg quality inspection, the transmission spectrum of eggs is used to assess internal quality parameters, like age and contamination [11-13]. Although methods based on spectral properties require more effort and complex equipment in the development stage, the resulting method is usually more simple and robust, and works with common and cheap equipment like monochrome cameras. Furthermore, if only specific wavelength bands are used, the results are less sensitive towards the color and intensity of the environmental light, as long as it is evenly distributed over the area. If required, other object detection methods can still be added in a later stage to increase detection performance.

With respect to our problem of object detection for PoultryBot, already some information on spectral properties of the relevant object categories can be found in literature. Prescott and Wathes [14] have presented an extensive review of reflective properties of poultry, their housing and the light characteristics therein. They presented results of 15 hen species, of which several are closely related to current commercial hybrids. Furthermore, they showed spectral results of various materials present in commercial poultry houses. Thus, their results provide a good starting point for our research. Spectral characteristics of hen eggs were used mainly for transmission measurements to determine the quality of shelled eggs [11, 12]. Less work has been done on spectral reflectance of eggs. In [14], only the spectral reflectance of a brown egg was reported. Gloag et al. [15] presented also other egg colors (although from a different bird), with similar results.

C. Contribution and paper outline

To see whether these results still hold in our conditions, we sampled spectral reflectance of the four object categories

*Research supported by Fonds Pluimveebelangen.

All authors are with the Farm Technology Group of Wageningen University, Wageningen, 6708 PB (phone: +31 317 482154; fax: +31 317 484819; e-mail: bastiaan.vroegindeweij@wur.nl).

relevant to PoultryBot. Based on the sampled spectral reflectance, we segmented images from a monochrome camera with a wavelength filter into these four categories. For a reliable operation of PoultryBot, it is desired that in the initial stage, at least 80% of the pixels (so not objects) in these four categories are correctly segmented. Most likely, this will lead to at least partial detection of the objects present in the image. Further processing can then be used to ensure that all objects are correctly identified. Finally, objects can appear in more than one image, so their chance of being detected is not completely depending on the results of processing a single image only.

Our main contribution is a generic method to develop simple and robust segmentation based on spectral information. Furthermore, we demonstrate its applicability to the segmentation of four object categories present in a modern aviary poultry house with white hens. Although other objects and environments (like greenhouse crops or arable fields) could be tested as well, we decided to limit ourselves to the poultry house. In Section II, we present the methods and materials used. In Section III, we offer the results, which are then discussed in Section IV. Conclusions and indications for future work are given in Section V.

II. MATERIALS & METHODS

The approach used in this work consists of the 10 steps below, and leads from the selection of relevant objects to the definition of threshold values for image segmentation.

1. Define which objects are relevant.
2. Measure the spectral reflection for each object category at all relevant wavelengths.
3. Select which measurements have to be included in the sample for each object category.
4. Find the distribution of reflections for each combination of wavelength and object category, based on the selected measurements.
5. Find the wavelength with the largest discriminative power, i.e. the one with the least overlap in reflection between the object categories.
6. Select a suitable band pass filter for this wavelength.
7. Acquire images using this band pass filter and a standard monochrome camera.
8. Find the distribution of intensity values for each object category in these images.
9. Use this information to define threshold values for segmentation.
10. Segment the image on pixel-level using these thresholds.

A. Materials tested

In step 1, the four main object categories considered relevant in this research where *eggs*, *chickens*, *housing*, and *litter*. As representatives of these, white eggs, feathers of white hens (Dekalb White), galvanized steel, and a litter sample from a poultry house were used. In step 2, spectral reflection of these objects was measured using the setup

described below. For this, the objects were placed on a white cardboard plate in the imaging setup. Other instances of the object categories (like brown eggs and feathers and clean wood shavings) were also measured in step 2, but not used in further processing.

B. Spectral measurement setup

The data on spectral reflection was collected using a hyperspectral line scan setup, based on the one mentioned in [16, 17] and shown in Fig. 1. This setup used an ImSpector V10E spectrograph (Spectral Imaging Ltd.) with a slit size of 30 μm , attached to a Photonfocus MV1_DV1320 camera and a 25 mm lens. Data was binned by 2 cells spatially and 4 cells spectrally, and the outside spectral cells were removed as they contained no relevant data. Thus, each scan contained a line of 656 pixels with 192 spectral bands between 400 and 1000 nm. As light source two tungsten halogen lamps of 150 W with a fibre and a rod lens were placed below the camera. The camera/spectrograph and the light source were attached to a stepper motor, such that they moved over the object with a fixed step size (0.5 mm), and an area with a length of 150 mm and a width of about 300 mm was measured. Before measurements, the camera and light source were on for at least 20 minutes to avoid start-up effects. Furthermore, a dark room was used to avoid influence from ambient light. In the setup, the reflectance of the object R is normalized from the measured intensity I . It is corrected for the background noise B , and expressed as fraction of the white reference W using

$$R = \frac{I - B}{W - B} \quad (1)$$

which is based on [17]. This normalization was performed automatically in the ISAAC2 software that controlled the imaging setup. Both references were acquired at the start of the measurement. The background noise B was acquired using a covered lens, while the white reference W was acquired using a 98% reflecting white plate.

C. Processing methods used

Processing of the spectral data was performed using Matlab. For each object category, between 38000 and 45000 pixels were manually selected from the acquired spectral

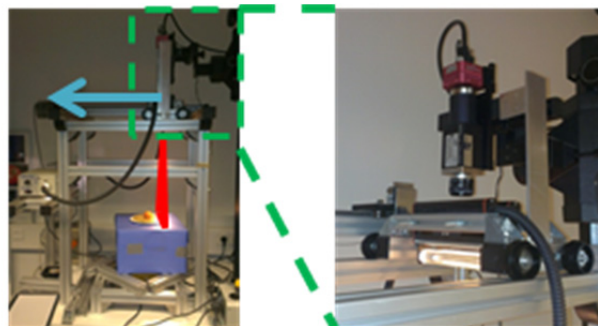


Figure 1: The hyperspectral imaging setup used for the experiments in step 2. On the left, the full setup is shown, with an indication of the linear motion of the camera (blue arrow) and the scan line (red triangle). The blue box is used to place the sample upon, in this case a brown egg on wood shavings. On the right, a close up of the moving construction for the camera, spectrograph and light source.

data. By using such a large number of pixels, the sample set covers more of the variation in the objects. For this, reconstructed RGB images were used to identify the objects, on which rectangles were drawn manually to select pixels to include in the sample (step 3). From these samples, the reflectance distribution at each wavelength band was determined (step 4). Next, a normal distribution was fitted on this data. From these results, the percentage of overlap between the distributions was calculated, for both the measured and fitted distributions. This was done for all 192 wavelength bands by Riemann integration of the overlapping area on the measured distributions and by trapezoidal integration on the fitted distributions. Next, the total amount of overlap per wavelength band was calculated by summing the values of all object categories. Based on this, the wavelength band could be selected where the sum of the overlap between the four groups was lowest (step 5).

D. Application of filtering at the selected wavelength band

The next step was to evaluate whether the chosen wavelength band was also effective under the conditions found in a commercial poultry house. Thus, images were acquired under such conditions, in the same poultry house as used in [3, 4]. In the house, animals of the same breed as used for the collection of the spectral data (Dekalb White) were present. Ambient light intensities were measured using a Voltcraft MS-1300 photometer, and ranged between 5 and 15 lux.

For image acquisition (step 7), a standard monochrome camera and a band pass filter at the selected wavelength band suffice. Thus, a band pass filter (470 nm, with a spectral width of 85 nm FWHM) was attached to an Ueye UI148xSE monochrome camera equipped with a lens with 4 mm focal distance. Frame rate was set to 3 fps, with the diaphragm fully opened and a fixed gain was applied inside the camera. Additional light was added to the scene using a 14-led white-blue light source, to better distribute the measured pixel intensities over the available sensor range.

Processing was performed with LabVIEW and started by taking the square root of each pixel, to correct for the uneven

illumination in the images. Next, the threshold levels for the various object categories were empirically determined from the images using visual feedback (step 9). Using these intensity values, pixel-wise segmentation was applied, to distinguish between the object categories (step 10). To improve the segmentation results, and allow for object detection, more (advanced) processing steps can be added in a later stage. Furthermore, a corresponding ground-truth image was obtained by manually labelling all pixels in the image into 5 categories: eggs, hens, housing, litter, and unknown.

III. RESULTS

The hyperspectral imaging (step 2) resulted for each pixel in a stack of 192 wavelength bands a 2D frame. From this, explanatory pictures like Fig. 2 could be made to inspect the results, before continuing to process them. Fig. 2 shows on the left side an RGB image (reconstructed from the wavelength bands), containing the four main object categories. On the right side, the spectra corresponding to locations indicated on the left are given. It can be seen that eggs had the highest reflectance, followed by chickens, housing and litter, although the latter two switch order in the second half of the spectrum. Furthermore, the difference between litter and both eggs and chickens was large at lower wavelengths, but reduced with increasing wavelengths. For housing and litter, the difference was initially small, but increased at larger wavelengths.

In step 3, multiple pixels for the same object category were selected, as described in Section IIC. The resulting reflectance distributions for the four object categories and two wavelength bands are shown in Fig. 3, together with normal distributions fitted to this data (step 4). Clear differences exist in the distribution of data. Litter and housing have narrower distributions than chickens and eggs. In addition, there is some overlap between litter and housing, as well as between feathers and eggs. Furthermore, this overlap turns out to differ between the various wavelength bands.

In step 5, overlap between all combinations of object types was quantified for each wavelength band, as described in section IIC. The least overlap was found for wavelength

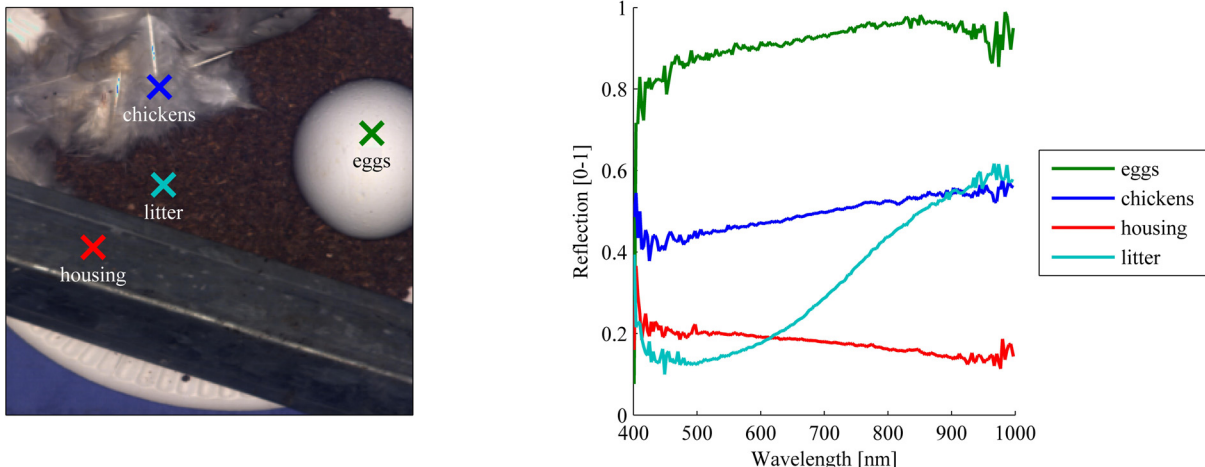


Figure 2: Results of hyperspectral imaging for the four object categories. On the left side an RGB image reconstructed from the spectral data, on the right side the spectra that correspond to the locations indicated on the left.

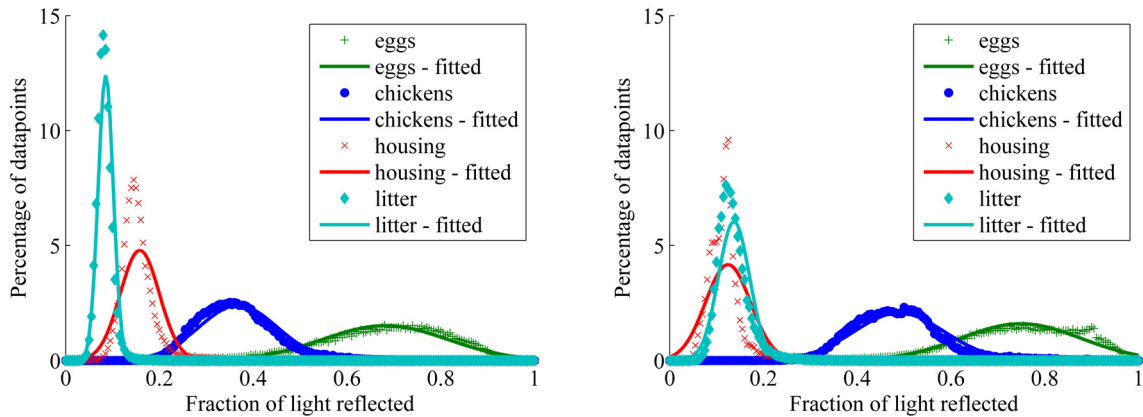


Figure 3: Distribution of reflectance for the 4 main object categories, at the 467 nm (left) and 663 nm (right) wavelength bands. Points indicate measured data, while lines represent the fitted distributions.

TABLE I. RESULTS OF WAVELENGTH SELECTION, SHOWING THE OVERLAP BETWEEN VARIOUS CATEGORIES IN PERCENTAGES. DATA IS PRESENTED FOR BOTH MEASURED AND FITTED DISTRIBUTIONS, AT THE BEST WAVELENGTH BAND (467 NM) AND A LESS SUITABLE WAVELENGTH BAND (663 NM).

Wavelength	Data type	Eggs vs. Chickens	Eggs vs. Housing	Eggs vs. Litter	Chickens vs. Housing	Chickens vs. Litter	Housing vs. Litter	Summed
467	measured	16.2	1.7	0.0	6.9	0.2	11.5	36.5
467	fitted	14.2	0.2	0.0	8.8	0.3	18.1	41.6
663	measured	23.0	1.0	0.3	2.7	0.8	78.1	105.7
663	fitted	24.4	0.0	0.0	1.1	0.6	79.1	105.3

bands between 430 and 515 nm. Among this range, the lowest overlap is found at the 467 nm band. In Table I, the overlap percentages are given for the best wavelength band (467 nm) and a clearly deviating one (663 nm), on both the measured and fitted data. Data in Table I corresponds to Fig. 3. There are clear differences in overlap between both wavelength bands and the various object combinations. At the 467 nm band, the overlap is quite evenly distributed over the categories, whereas at other wavelength bands, it has moved more towards one or two combinations. Most overlap is found between eggs vs. chickens and housing vs. litter, whereas the combinations eggs vs. housing, eggs vs. litter and chickens vs. litter have hardly any overlap.

Based on the lowest amount of overlap, a band pass filter around 470 nm was selected for image acquisition in the poultry house (step 6-7). Two of the acquired images are shown in Fig. 4, together with the preliminary results from segmentation (step 9) and the associated ground truth. The artificial illumination pattern that is visible in the images affected the segmentation results. For example, part of the litter was segmented as hens or housing and some mixing of object categories was present on pixel level. In some images, housing objects had similar intensities as hens and litter, and could thus not be segmented separately. Also, ambient light intensity varied considerably within some images, which made accurate setting of the threshold values difficult. Depending on the object category, the requirement of correctly segmenting 80% of the pixels in the correct group seemed possible.

DISCUSSION

In the results, significant variation in the reflectance can be observed at the ends of the measured spectra. A likely explanation is the limited amount of light available at these wavelengths, especially around 400 nm, as the light source emitted hardly any UV light. Combined with limited sensitivity of the camera chip at the ends of its spectral range, this might result in reflectance values that are largely determined by sensor noise [17]. Prescott and Wathes [14] indicate similar findings from their measurements, especially around 400 nm. They did not indicate whether this originated from technical limitations of their setup instead or if it was a specific feature of the sample measured. To investigate whether any relevant features are present in the wavelength range below 450 nm, it is advised to add a UV light source to the hyperspectral imaging setup. However, the amount of UV available in a poultry house is limited, and artificially adding UV light might have undesirable consequences for animal welfare. Thus, investigating or using UV wavelengths seems of limited use for our case.

Furthermore, measurements on housing material were performed using relatively clean materials. In the poultry house however, it can be expected that there is some contamination with dust and poultry droppings. As result, the reflectance of objects might vary from the values presented and the spectral response might change. Also, reflectance of housing was constant throughout the spectrum, but sensitive to the angle towards the light source during hyperspectral imaging. Thus, this requires substantial attention when using

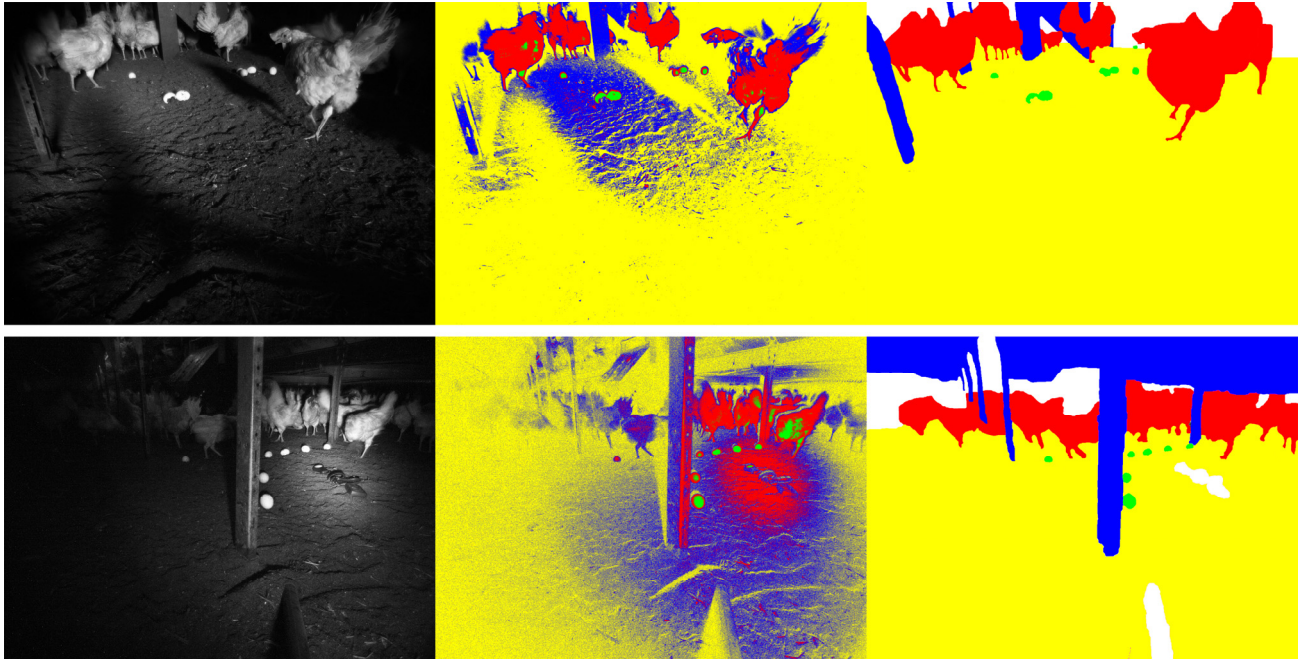


Figure 4: First segmentation results. From left to right: original image (brightness increased by 100), segmentation result, ground truth.

the presented approach and data to test and develop methods for practical applications.

For the selection of the most suitable wavelength band, the sum of the overlap percentage was used. Here, segmentation was weighted equally for each object combination. For practical applications however, it might be relevant to apply different weight factors, to allow better discrimination of objects that are of higher importance. For improving the segmentation results, using multiple spectral bands simultaneously seems also promising. In this way, separate wavelength bands can be selected for different object categories, such that differences in reflectance become more distinct. Initial testing on segmentation for brown eggs indicated that overlap could be reduced from 40 to 10% using this method.

Initial results from applying this approach in a poultry house show that segmenting multiple object categories using this method is quite promising. However, still some difficulties arise, especially with respect to the light distribution in the image and setting the thresholds for the segmentation of housing. Both problems might be related, and have to do with the low amounts of ambient light. Thus, additional illumination was required. As a result, illumination spots appear, which require correction during processing. Also, they lead to a wider range of intensities for a single object category than was expected from step 4. Thus, object categories tend to overlap more, which makes it more difficult to segment them correctly. Possible options to deal with this are the adding of more homogeneous illumination or an improved illumination correction to improve the input image. As processing is currently done using a very simple threshold, segmenting by more advanced methods like considering adjacent pixels or using fuzzy methods to relate pixels to multiple object categories might be used as well.

Such methods can be combined with morphologic image processing like erode, dilate and shape filtering to reconstruct object shapes and thus improve the final classification result. The first results of the method presented are promising, and can be extended to reach the desired level of 80% correctly segmented pixels. Future work will address improvement of results by adding more advanced processing, and evaluation under a wider range of conditions.

CONCLUSION

In this work, a simple and robust segmentation method based on spectral reflectance properties was presented. Spectral reflectance of four object categories that are relevant for PoultryBot (eggs, chickens, housing and litter) was investigated in the range between 400 and 1000 nm. Between the four object categories that are relevant for PoultryBot (eggs, chickens, housing, and litter), clear differences could be observed in the amount of reflectance. At the wavelength band around 467 nm, the overlap of the four object categories was found to be the lowest, and was 16% for chickens and eggs, 12% for litter and housing, and lower for the other combinations. Images taken in a commercial poultry house, using a standard monochrome camera and a band pass filter around 470 nm, indicated that pixel-based segmentation of the object categories is possible using this method. First results showed that the desired level of 80% correctly segmented pixels seems possible, making this method a promising direction for future work.

ACKNOWLEDGMENT

The authors like to thank Gerrit Polder from Wageningen UR Greenhouse Horticulture for the use of their hyperspectral imaging facilities.

REFERENCES

- [1] H. J. Blokhuis and J. H. M. Metz, *Aviary housing for laying hens*. Wageningen, 1995.
- [2] D. Claeys, *Socio-economische gevolgen van verschillende huisvestingssystemen in de leghennenhouderij*. Merelbeke-Lemberge: Instituut voor Landbouw- en Visserijonderzoek, Eenheid Landbouw & Maatschappij, 2007.
- [3] B. A. Vroegindeweyj, L. G. van Willigenburg, P. W. G. Groot Koerkamp, and E. J. van Henten, "Path planning for the autonomous collection of eggs on floors," *Biosystems Engineering*, vol. 121, pp. 186-199, 2014.
- [4] B. A. Vroegindeweyj, J. IJsselmuiden, and E. J. v. Henten, "Probabilistic localisation in repetitive environments: estimating a robot's position in an aviary poultryhouse," *submitted to Computers and Electronics in Agriculture*, 2015.
- [5] V. Sandilands and P. M. Hocking, *Alternative systems for poultry : health, welfare and productivity*. Wallingford [etc.]: CABI, 2012.
- [6] R. Szeliski, *Computer vision: algorithms and applications*. Springer Science & Business Media, 2010.
- [7] L. Chang, M. M. Duarte, L. E. Sucar, and E. F. Morales, "A Bayesian approach for object classification based on clusters of SIFT local features," *Expert Systems with Applications*, vol. 39, pp. 1679-1686, 2012.
- [8] A. Piron, V. Leemans, O. Kleynen, F. Lebeau, and M. F. Destain, "Selection of the most efficient wavelength bands for discriminating weeds from crop," *Computers and Electronics in Agriculture*, vol. 62, pp. 141-148, 2008.
- [9] A. T. Nieuwenhuizen, J. W. Hofstee, J. C. van de Zande, J. Meuleman, and E. J. van Henten, "Classification of sugar beet and volunteer potato reflection spectra with a neural network and statistical discriminant analysis to select discriminative wavelengths," *Computers and Electronics in Agriculture*, vol. 73, pp. 146-153, 2010.
- [10] E. J. van Henten, J. Hemming, B. A. J. van Tuijl, J. G. Kornet, J. Meuleman, J. Bontsema, *et al.*, "An Autonomous Robot for Harvesting Cucumbers in Greenhouses," *Autonomous Robots*, vol. 13, pp. 241-258, 2002.
- [11] B. De Ketelaere, F. Bamelis, B. Kemps, E. Decuypere, and J. De Baerdemaeker, "Non-destructive measurements of the egg quality," *World's Poultry Science Journal*, vol. 60, pp. 289-302, 2004.
- [12] K. Mertens, I. Vaesen, J. Loffel, B. Kemps, B. Kamers, C. Perianu, *et al.*, "The transmission color value: A novel egg quality measure for recording shell color used for monitoring the stress and health status of a brown layer flock," *Poultry Science*, vol. 89, pp. 609-617, 2010.
- [13] M. Chen, L. Zhang, and H. Xu, "On-line detection of blood spot introduced into brown-shell eggs using visible absorbance spectroscopy," *Biosystems Engineering*, vol. 131, pp. 95-101, 2015.
- [14] N. B. Prescott and C. M. Wathes, "Reflective properties of domestic fowl (*Gallus g. domesticus*), the fabric of their housing and the characteristics of the light environment in environmentally controlled poultry houses," *British poultry science*, vol. 40, pp. 185-193, 1999.
- [15] R. Gloag, L.-A. Keller, and N. E. Langmore, *Cryptic cuckoo eggs hide from competing cuckoos* vol. 281, 2014.
- [16] G. Polder, E. J. Pekkeriet, and M. Snickers, "A Spectral Imaging System for Detection of Botrytis in Greenhouses," in *Proceedings of the EFITA-WCCA-CIGR Conference Sustainable Agriculture through ICT innovation, 23-27 June, 2013, Turin, Italy*, 2013.
- [17] G. Polder and I. T. Young, "Calibration and characterisation of imaging spectrographs," *Journal of Near Infrared Spectroscopy*, vol. 11, pp. 193-210, 2003.

Recognizing Apples by Piecing Together the Segmentation Puzzle

Kyle Wilshusen¹ and Stephen Nuske²

Abstract—This paper presents a system that can provide yield estimates in apple orchards. This is done by collecting and processing image datasets of the apple orchard. The algorithm introduced in this paper provides 3 contributions. First, the apple detection algorithm is shown to provide a very high level of apple segmentation and classification accuracy. Second, the algorithm is an automated system that requires mask images, instead of user specified parameters to create an apple detection classifier. Finally, the algorithm labels semantic information such as apple parts, such as apple edges, which is unique from previous apple detection methods.

I. PREVIOUS WORK

The problem of apple detection in orchards is still a relatively new problem. The largest strides have been made using image detection models that use multiple cameras and very accurate state estimation to estimate the position of individual apples within an orchard [6]. This previous work requires calibrated saturation and hue values, which vary by dataset and are set manually in configuration files. In contrast to this previous approach, this work aims to evaluate detection performance in images only, and is not extended to apple registration on the ground. Our algorithm requires user annotated training images, which are input to a machine learning algorithm to dynamically learn a classifier.

A larger body of research has been completed on grape detection in vineyards. Accurate solutions have been developed that can correctly count grape yield to within 10% of the actual yield on the ground (Nuske, et al. 2014). The system used to detect grapes does not focus on calculating individual fruit positions throughout the vineyard, but instead calculates a fruit per meter estimate for every position that the vehicle traverses. To detect fruit in images for this approach, texture and color features are used to create the grape/non-grape classifier, and a focus on detecting grape keypoints takes precedence over batch processing of pixel values from across the image.

There are other processes that are more focused on the batch processing approach, where many pixels are analyzed with texture descriptors before being considered as possible fruit locations. One such method uses superpixels to create certainty maps for fruits such as pineapples. This idea directly influenced our work, and is the reason that we create superpixel certainty maps for green apples [2]. In another set of work, green fruit's are detected on plants, which is similar to the problem that we approach of detecting green apples in orchards [1]. In this work, a less exhaustive approach

is employed, as an attempt is made to focus the search on particular areas of the image that are likely to have fruit.

A number of research works have mentioned the theory that in orchard environments there is a constant occlusion factor, which can be used to calibrate detections from the visible fruit that is detected in images to the actual fruit that occurs on the ground[4], [6]. This paper aims to both increase the accuracy of detection of fruit that is in full view through structural features, and also introduce the idea of "partial" apple detection that represent partial fruit detections, allowing highly uncertain fruit detections to contribute an amount to the total fruit estimate that is less than one.

One of the most important cues on fruit that has been imaged at night is the spot of specular reflectance [4], [6]. Methods using a point of specular reflectance require that a point of specular reflectance be in full view of the camera imaging the fruit. For both methods, the intensity is evaluated to steadily decrease off the sides of the maximal point. While the steady descent of intensity is telling, this steady descent can be observed on any part of a spherical fruit in the form of intensity rings on a particular edge of the fruit. These rings can both be used to evaluate the spherical shape of the fruit and also to find the edge of the fruit by evaluating when the intensity decrease pattern stops at an abrupt edge. This paper creates a "maximal detector" similar to the detector used in [4], which is adaptable for use anywhere on the apple. This method isolates apple edges, instead of apple peaks.

The previous apple segmentation approach of [6] was to filter every pixel in the image through hue and saturation filters. Processing every pixel is reasonable for color processing, but for more advanced machine learning operations it can take too long. An alternative is to representatively subsample an image. We follow the subsampling technique that was developed in the work of [5]. The idea is that powerful machine learning techniques are often required to accurately segment an image, but because of processing constraints these techniques cannot be computed on the pixel level over large images. Superpixels can be computed to group image features into homogeneous groups of color and texture features before additional processing is completed. This paper utilizes the current state of the art in 2015: SLIC superpixels [7].

II. METHODOLOGY

A. Three Goals

The three goals of this work are to increase the accuracy of apple segmentation algorithms, to create an apple classifier through the use of user annotated images, in place of user specified classification parameters, and to semantically label

¹Kyle is a PhD student at University of Pennsylvania wilshusen.kyle@gmail.com

²Stephen Nuske is a Systems Scientist at Carnegie Mellon University

image features that are not full apples, specifically to find the edges of heavily occluded apple segments.

B. User Annotated Classifier Creation

A training set is the one piece of user input that is required by our algorithm. A training set is created by the user. This training set consists of mask images that specify the pixels in an image that are fruit and the pixels in an image that are not fruit. A supervised training method is used to setup a random forest classifier from these training images. A grid of features is extracted over the image with a 10 pixel spacing between grid points for 2 MegaPixel images. Features are extracted over the grid, and then a label for each of the features extracted is determined from the training mask images that correspond to the raw images in the training set. The training set can be seen below, including the grid configuration that shows feature extraction locations.



Fig. 1. Training Images are Mask Images

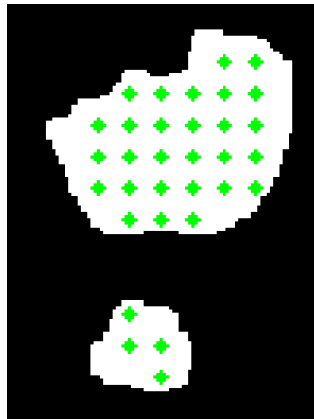


Fig. 2. Automatically label a grid of points to sample



Fig. 3. Raw Image

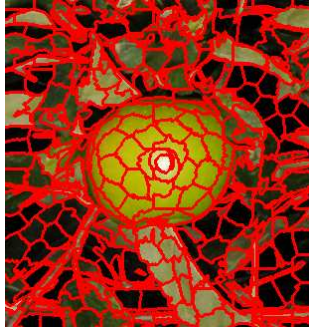


Fig. 4. SLIC Superpixels

Over each grid location, color and texture features are extracted. In our implementation, HSV features are used to quantify color and SURF features are used to quantify texture. These training set features are normalized and combined together using a PCA transform to reduce the feature set size. The random forest classifier is then created from the normalized and reduced feature set.

To segment images into apple and non-apple pixels, a four step process is completed. First, superpixels are computed

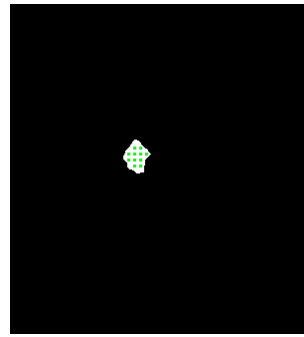


Fig. 5. Individual Superpixel

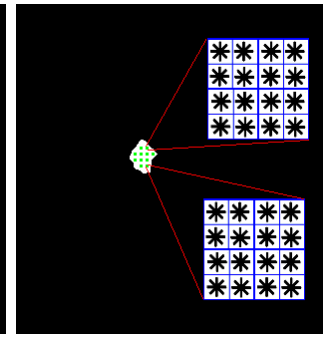


Fig. 6. Features are extracted in a grid pattern over each superpixel. The SIFT feature descriptor is depicted here, but any filter could be used.

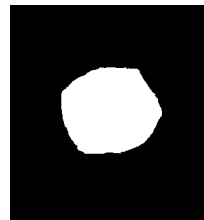


Fig. 7. Apple segmentation

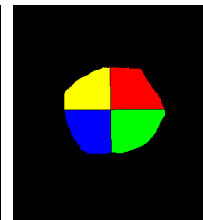


Fig. 8. Apple parts

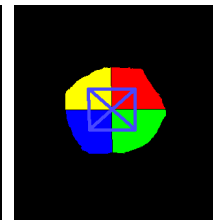


Fig. 9. Apple parts grouping to full apple detection

using the SLIC superpixel algorithm. Second, features are extracted in a grid over each superpixel. Third, grid points are classified using the random forest classifier created at train time. Fourth, the ratio of apple to non-apple pixels within each superpixel is computed, and is recorded in the apple confidence map, which can be seen in section III-A.

After apple confidence is determined over the image, apple pixels can be segmented into different levels of apple certainty. Individual apple detection then becomes the goal. We use a two step process, whereby full apples are labelled first, and heavily occluded apples are labelled afterwards with detection magnitudes less than 1.

Fruit detection from this point forward in our method is completed exclusively by analyzing the direction and magnitude of the image's intensity gradient. Gradients classifications are used to identify an apple's spherical shape. Gradients could belong to four different classifications: upward gradient, right gradient, left gradient, or downward gradient. There is a correct orientation for these apple components in a valid apple. For example, a downward sloping region is likely below an upward sloping apple region, as apples are spherical. The superpixels that were used earlier to group pixel classifications are used again to group gradient classifications into configurations that make sense and agree with one another.

Full Apple Detection Process:

- Superpixels are Computed.
- SURF and HSV Features are Extracted Across Superpixels.

- Superpixels are Labelled as "Apple" or "Non-Apple" by Querying the Classifier
- Apple Superpixels are Labelled by Regions Classifications (Upward Left, etc.).
- Merge Neighboring Region Classifications w/ Valid Relationships (Downward Gradient Region below Upward Gradient Region, etc.).
- Merged Groups with Sufficient Area are Individual Fruit Detections.

After full apple detections have been identified, the objective is to label apples that are not in full view but are partially visible. Previous apple detection approaches have labelled partial apple detections as full apples, but this is a tricky and risky business, as often leaves can be classified as green apples. Partial apple detections can be completed by evaluating apples to find the dominant gradient direction if available, and hopefully finding part of the apple's edge. The dominant gradient can be found by obtaining the maximal gradient in the region and ensuring that the normalized standard deviation of the gradients within the region is under a certain value.

While the intensity gradient within a region is important, the edge of the region is also important. The maximal keypoint descriptor described in [4] was used to detect points of maximal specular reflectance. The method is accurate if a maximal point is visible. Often in orchards a clear maximal specular reflectance point is not visible, due to occlusion. A maximal point can be interpreted from the decreasing intensity. Edge detection is used to verify partial apple detection regions. The region can be verified and the edge of the region can be labelled by verifying that the intensity rings decrease in a predictable way from the apple center until a very strong intensity change is encountered.

Partial Apple Detection Process: Completed After Full Apple Detection Process

- Removal of Pixels Corresponding to Full Apple Detections from Data
- Connected Components (CC) of Remaining Pixels Form the Search Space for Partial Detections
- Obtain the Dominant Gradient Direction (DGD) of each CC
- Verify the CC is Consistent Relative to its DGD (Apple Edges match DGD, Absence of Conflicting Gradient Directions, Size of CC)

Semantic labeling throughout orchard images is important beyond apple curves as in the highly occluded, highly similar scene correlations are needed to label objects. Apple orchards often have guidewire that supports the orchard trees. The guidewire is identified by locating points that form a sharp horizontal line and have high intensity. With a hough transform, it is very simple to find these lines consistently. The stereo pair for this dataset was setup vertically, so the horizontal guidewires occur at different heights in both stereo images. 3D lines can be calculated from the guidewire appearances in both images of the stereo pair.

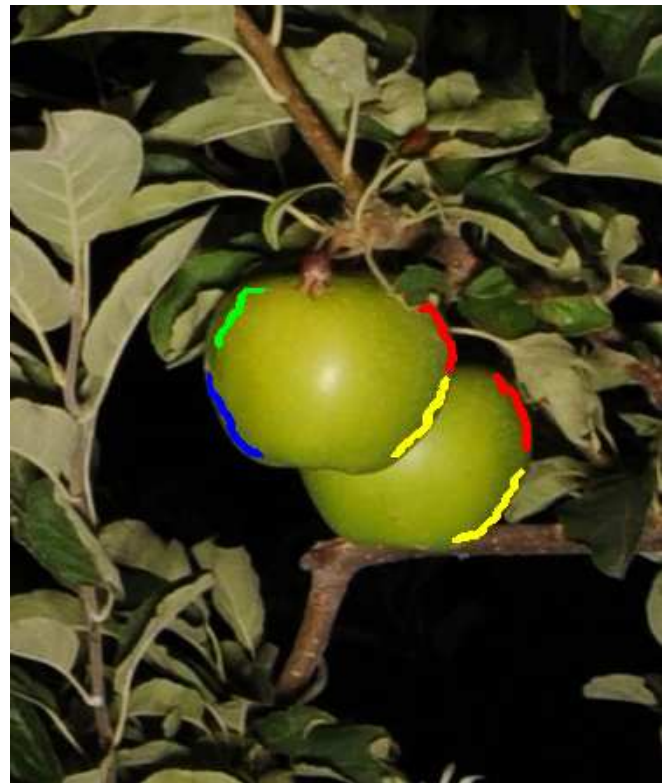


Fig. 10. Finding the Apple's Edge is Vital to Detecting Occluded Apples in Images.

III. RESULTS

Results start with the segmentation of apple pixels from non-apple pixels. Second, semantic labelling performance and apple detection performance are evaluated. And, finally, apples are registered to ground detections.

A. Apple Segmentation

From the confidence map, it is easy to see that the apple pixels are very brightly illuminated, signifying the classifier has some understanding of the difference between apple and non-apple.

An evaluation over the training set can be done with the confidence map and the labelled mask image. Using both the confidence map and the labelled mask image, a precision/recall curve can be produced to quantify the results. This is done by including different points in the confidence map. From the pixels that are 100% likely to be apple to the pixels that just might be apple. The precision/recall curve shows that apple segmentation is stable and quite accurate.

B. Apple Detection

Apple segmentation is only important for apple detection. In natural environments, there are a number of problems that arise in apple detection. First, apples occur in different orientations and scales. Second, many apples are occluded by other objects in the orchard. This means that many apples will not be detected by any other features other than hue and saturation. The bounding box images are shown below. Apple



Fig. 11. Raw Image

Fig. 12. Confidence Map



Fig. 14. Bounding Boxes for the Visual Apple Counting Trial.

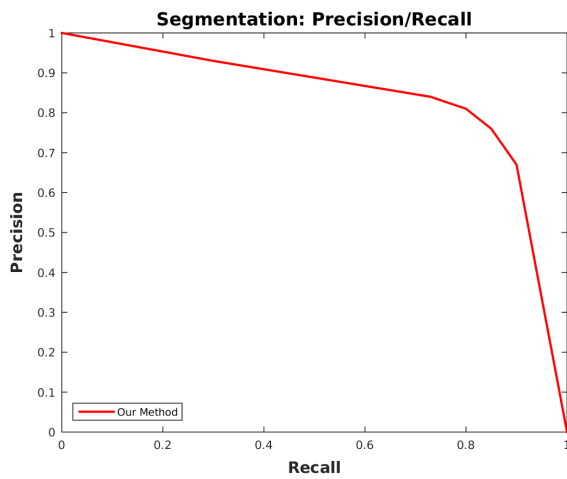


Fig. 13. Segmentation: Precision Recall Curve

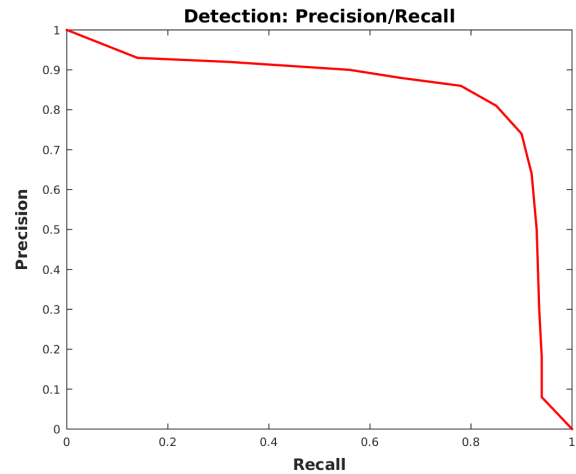


Fig. 15. Detection: Precision Recall Curve

Detection performance is also shown below and seen to be high. Detection performance is higher than segmentation performance because not all apple pixels need to be identified by gain an accurate apple detection.

C. Semantic Apple Labelling

Labelling apples in previous works has focused heavily on color information. In the image below, it can be seen that a majority of the apple edges have been detected and there are predicted locations for unidentified apple edges that can be seen in magenta, which are very close to their true locations. Identifying apple edges near occlusions is a task for the future. Apple edge detection is important because edges delineate the fruit from other objects and give information on the orientation of the apple.

D. Apple Registration

Of course, the eventual goal of yield estimation is to detect fruit on the ground, instead of in images. Here, we evaluate against a dataset that was collected at the Fruit Research and Extension Center in Biglerville, PA in 2012. Six orchard



Fig. 16. Raw Image

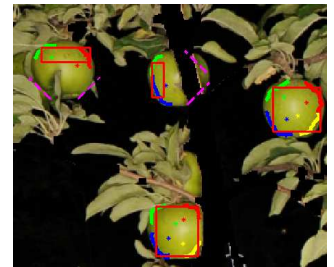


Fig. 17. Apple edge detection is in many cases successful (as seen to the right and bottom of the image). Right now, we are often unable to overcome occlusions that result from branch or leaf occlusions.



Fig. 18. Initial guidewire detections have low recall, but high precision.



Fig. 19. The guidewire detections can be extrapolated across the entire image with a very high degree of accuracy.

sections were sampled by hand and by the algorithm to account for occlusion. This was done by computing an "occlusion ratio" that would translate 2D yield estimates to 3D predictions of fruit on the ground. The overall error is seen to be low, as the algorithm undercounted by just 6 percent.



Fig. 20. Our method can confuse full apple detections with partial apple detections, as seen by the large blue box shown here.



Fig. 21. Our approach can detect apples with hues that are slightly different and also label apple parts for heavily occluded apples (blue box w/ arrow).

IV. CONCLUSION

This paper has provided three contributions to the research community. It has increased the segmentation accuracy of green apples from backgrounds using the concept of combining confidence maps and superpixels. It has created a supervised learning method that only requires a set of annotated images and takes the user involvement out of creating calibration values. And, finally, this work has started the

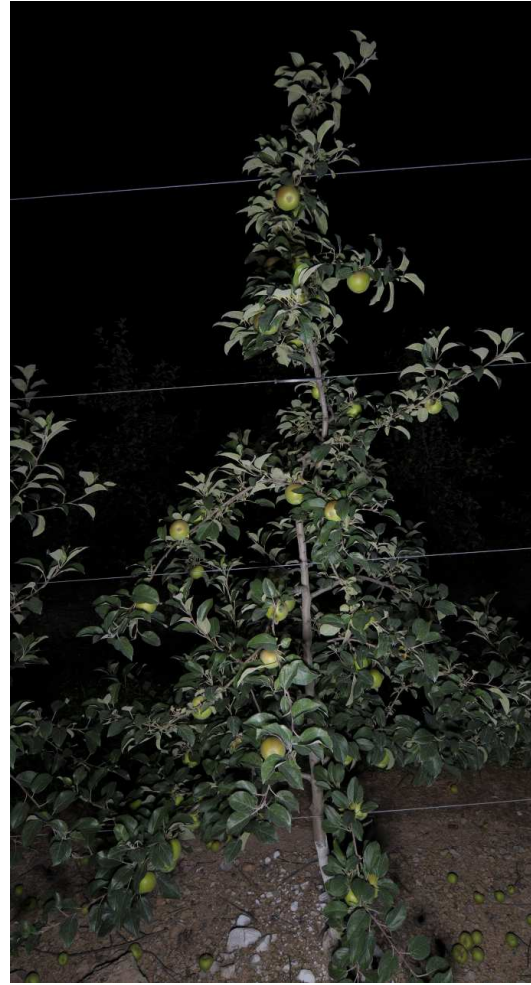


Fig. 22. A new dataset of Honeycrisp apples is used to evaluate yield estimates.

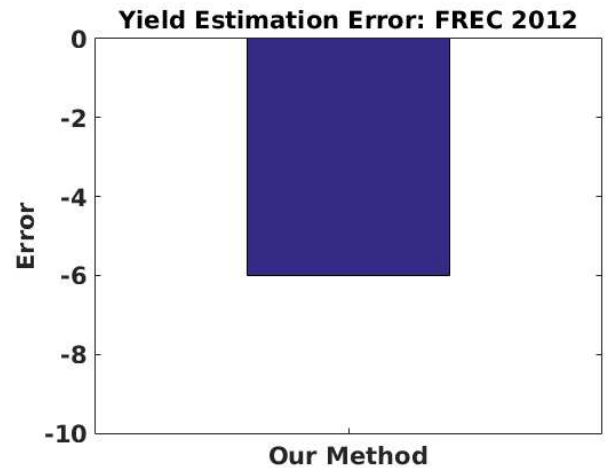


Fig. 23. This graph shows overall error prediction rates for the newly processed Honeycrisp dataset.

work of semantically labelling entire orchards environments, which will help to move towards classifying specialty crops in more advanced ways than just using color to identify fruit. While this method has only been tested on apple datasets, the core infrastructure of the method could be used to identify all specialty crops that have distinguishing color and texture from their environments.

REFERENCES

- [1] Chaivivatrakul, Supawadee, and Matthew N. Dailey. "Texture-based fruit detection." *Precision Agriculture* 15.6 (2014): 662-683.
- [2] Qureshi, Waqar. "Dense Segmentation of Textured Fruits in Video Sequences." *International Conference on Computer Vision Theory and Applications. Proc. of International Conference on Computer Vision Theory and Applications*. N.p.: SCITEPRESS Digital Library, 2014. 441-47. Web.
- [3] Bay, Herbert, Andreas Ess, Tinne Tuytelaars, and Luc Van Gool. "Speeded-Up Robust Features (SURF)." *Computer Vision and Image Understanding* 110.3 (2008): 346-59. Web.
- [4] Nuske, Stephen, et al. "Automated Visual Yield Estimation in Vineyards." *Journal of Field Robotics* 31.5 (2014): 837-860.
- [5] Shi, Jianbo, and Jitendra Malik. "Normalized cuts and image segmentation." *Pattern Analysis and Machine Intelligence, IEEE Transactions on* 22.8 (2000): 888-905.
- [6] Wang, Qi, et al. "Automated crop yield estimation for apple orchards." *Experimental Robotics*. Springer International Publishing, 2013.
- [7] Achanta, Radhakrishna, et al. Slic superpixels. No. EPFL-REPORT-149300. 2010.

Program Committee

The following people have confirmed their participation in the program committee (in alphabetical order):

- Dr. Muhammad Abubakr , LUMS School of Science & Engineering, Pakistan
- Prof. Dr. Marcel Bergerman, IEEE TC on Agricultural Robotics and Automation, and Senior Systems Scientist at the Robotics Institute, Carnegie Mellon University, United States
- Prof. Dr. Karsten Berns, Robotics Research Lab, University of Kaiserslautern
- Prof. Dr. Nils Bjugstad, Department of Mathematical Sciences and Technology, Norwegian University of Life Sciences
- Prof. Dr. Herman Bruyninckx, Dept Mechanical Engineering, University of Leuven, Belgium, and Dept Mechanical Engineering, Eindhoven University of Technology, Netherlands
- Dr. Fernando Auat Cheein, Robotics Research Group, Universidad Técnica Federico Santa María
- Dr Grzegorz Cielniak, University of Lincoln, UK
- Dr. Amir Degani, Civil and Environmental Engineering Technion, Israel Institute of Technology
- Dr. Renaud Detry, Systems and Modeling Group, University of Liège, Belgium and the Computer Vision and Active Perception lab, Royal Institute of Technology (KTH), Stockholm, Sweden
- Prof. Dr. Yael Edan, ABC Robotics Initiative, Ben-Gurion University of the Negev, Israel
- Dr. Robert Fitch, Australian Centre for Field Robotics, The University of Sydney
- Dr. Pål Johan From, Department of Mathematical Sciences and Technology, Norwegian University of Life Sciences
- Prof. Dr. Eldert van Henten, IEEE TC on Agricultural Robotics and Automation, and Full professor at the Farm Technology Group, Wageningen University, The Netherlands
- Siddhartha S. Mehta, Department of Industrial and Systems Engineering, University of Florida
- Prof. Dr. Joachim Hertzberg, Robotics Innovation Center, German Research Center for Artificial Intelligence (DFKI), Osnabrück, Germany
- Dr. Ir. Joris IJsselmuiden, Farm Technology Group, Wageningen University, Netherlands
- Dr. Manoj Karkee, Center for Precision & Automated Agricultural Systems, Washington State University, US
- Dr. Jay Katupitiya, School of Mechanical and Manufacturing Engineering, University of New South Wales, Australia
- Dr. Gert Kootstra, Computer Vision, Post-Harvest Technology, Wageningen University and Research, The Netherlands
- Dr. Saman Abdanan Mehdizadeh, Faculty of Agricultural Engineering, Ramin Agriculture and Natural Resources University, Iran
- Dr. Lazaros Nalpantidis, Robotics, Vision and Machine Intelligence Lab, Aalborg University Copenhagen, Denmark
- Dr. Dejan Pangercic, Deepfield Robotics.
- Dr. Johan Philips, Mechanical Engineering, University of Leuven, Belgium
- Giulio Reina, University of Salento, Italy
- Filipe Neves Dos Santos, INESC TEC, Portugal
- Dr. Slawomir Sander, Robert Bosch Start-up GmbH, Germany
- Ir. Mathijs Vermeulen, Lacquey BV, Netherlands
- Dr. Ir. Niels Wouters, Department of Biosystems, MeBioS, University of Leuven, Belgium
- Rick van de Zedde, Computer Vision, Post-Harvest Technology, Wageningen University and Research, Netherlands